Roman Messner, BSc

Spectroscopy of gold atoms and gold oligomers in helium nanodroplets

MASTER'S THESIS

to achieve the university degree of
Diplom-Ingenieur

Master's degree programme: Technical Physics

submitted to

Graz University of Technology

Supervisor
Univ.-Prof. Mag. Dr.rer.nat Wolfgang E. Ernst
Institute of Experimental Physics

Co-Supervisor
Dipl.-Ing. Dr.techn. Florian Lackner
Institute of Experimental Physics

Graz, February 2018

AFFIDAVIT

I declare that I have authored this thesis independently, that I have not used other than the declared sources/resources, and that I have explicitly indicated all material which has been quoted either literally or by content from the sources used. The text document uploaded to TUGRAZonline is identical to the present master's thesis.

Date

Signature

Abstract

The main focus of this master's thesis was the development of an experimental setup to conduct resonantly enhanced multiphoton ionization spectroscopy of atoms and oligomers inside cold superfluid helium nanodroplets as well as the investigation of gold atoms in helium droplets with this exact setup.
Implementing the setup required the familiarization with multiple devices such as the helium droplet generation apparatus, time of flight mass spectrometer, and laser equipment. All these different parts had to be brought together in a reliable configuration. In particular, the laser setup involved the adjustment of many different variables, in order to obtain a performance-optimized output. Crucial components are the maintenance of the XeCl pump laser, mixing of the laser dyes, adjustment of the dye laser, calibration of the second harmonic generation stage, and the synchronization of the laser with the time of flight mass spectrometer, where ions were detected.
In the further course of the master's thesis, the $6p\,^2P_{1/2} \leftarrow 6s\,^2S_{1/2}$ and
$6p\,^2P_{3/2} \leftarrow 6s\,^2S_{1/2}$ transitions (D lines) of gold atoms embedded in superfluid helium nanodroplets were experimentally investigated using resonant two-photon ionization spectroscopy. Both transitions are strongly blue-shifted and broadened due to the repulsive interaction between the Au valence electron and the surrounding helium. The in-droplet D lines are superimposed by the spectral signature of Au atoms relaxed into the lowest (metastable) ^{2}D states. These features are narrower than the in-droplet D lines and exhibit sharp rising edges that coincide with bare atom transitions. It is concluded that they originate from metastable ^{2}D state $AuHe_n$ exciplexes which have been ejected from the helium droplets during a relaxation process. Interestingly, the mechanism that leads to the formation of these complexes is suppressed for very large helium droplets consisting of about $2\,x\,10^6$ He atoms, corresponding to a mean droplet diameter of approximately 50 nm. The assignment of the observed spectral features is supported by *ab-initio* calculations employing a multiconfigurational self consistent field (MCSCF) method and a multireference configuration interaction (MRCI) calculation.
For the largest employed helium droplets doped with Au oligomers, excitation spectra for mass channels ranging from Au_2 up to Au_9 are presented. The mass spectra reveal even-odd oscillations in the number of Au atoms that constitute the oligomer, which is characteristic for coinage metal clusters. A resonance is observed close by the in-droplet D2 transition, which, surprisingly, exhibits a similar shape in the spectra for all detected oligomer sizes.

Kurzfassung

Der Hauptaugenmerk dieser Masterarbeit lag in der Erstellung eines experimentellen Aufbaus zur Durchführung resonanzverstärkter Mehrphotonenionisationsspektroskopie von Atomen und Oligomeren in kalten suprafluiden Helium Tröpfchen, sowie in der spektroskopischen Untersuchung von Gold Atomen in Helium Tröpfchen.
Die Implementierung des Aufbaus erforderte die Vertrautmachung mit vielen verschiedenen Gerätschaften, wie der Apparatur zur Erzeugung von Helium Tröpfchen, dem Flugzeit Massenspektrometer und dem Laser Setup. Alle Komponenten mussten in einer verlässlichen Konfiguration aneinandergefügt werden. Insbesondere das Laser Setup beinhaltet viele verschiedene Variablen, die für ein leistungoptimiertes Output angepasst werden müssen. Wesentlich hierfür sind die Instandhaltung des XeCl Pumplasers, das Mischen der Laserfarbstoffe, die Einstellung des Farbstofflasers, die Kalibration der frequenzverdoppelnden Stufe sowie die Synchronisierung der Lasers mit dem Time of Flight Massenspektrometer, wo die Ionen schlussendlich detektiert werden.
Im weiteren Verlauf der Masterarbeit wurden der $6p\,^2P_{1/2} \leftarrow 6s\,^2S_{1/2}$ und der $6p\,^2P_{3/2} \leftarrow 6s\,^2S_{1/2}$ Übergang (D Linien) von Gold Atomen eingebettet in suprafluiden Helium Tröpfchen mittels resonanter Zweiphotonenspektroskopie untersucht. Beide Übergänge erscheinen stark verbreitert und blau verschoben, was für die repulsive Wechselwirkung von den Gold Atomen mit der Helium Umgebung typisch ist. Die in-droplet D Linien sind mit der spektralen Signatur von Gold Atomen überlagert, welche in die tiefstliegenden (metastabilen) ^{2}D Zustände relaxiert sind. Diese Linien haben eine schmalere Breite als die in-droplet D Linien und weisen scharf ansteigende Kanten auf, welche mit atomaren Übergängen zusammenfallen. Daraus wurde geschlossen, dass diese Linien von ausgeworfenen $AuHe_n$ Exciplexen im ^{2}D Zustand herrühren. Allerdings scheint der Mechanismus, der zur Produktion dieser freien Exciplexe führt, für große Helium Nanodroplets bestehend aus $2\,x\,10^6$ He Atomen (und 50 nm Durchmesser), unterdrückt zu sein. Die Zuordnung der spektralen Charakteristika wurde durch *ab-initio* Rechnungen unterstützt. Hierzu wurden eine Multi Configuration Self Consistent Field (MCSCF)- und eine Multireference Configuration Interaction (MRCI) Rechnung durchgeführt.
Für die größten verwendeten Helium Tröpfchen, in denen Gold Oligomere in ausreichender Zahl vorhanden sind, konnten Anregungsspektren von Au_2 bis Au_9 aufgenommen werden. Die Ionenausbeute in den Massenspektren weisen für Münzmetall charakteristische even-odd Oszillationen für die Anzahl an Atomen im Oligomer auf. Eine Resonanz wurde bei der in-droplet D2 linie beobachtet, die für alle Oligomere die gleiche Form aufweist.

Contents

Abstract iii

Kurzfassung iv

1 Introduction 1

2 Theoretical background 4
2.1 Historical background of matrix isolation spectroscopy . . . 4
2.2 Helium . . . 5
2.2.1 Physical and chemical properties of helium . . . 6
2.2.2 Helium droplets . . . 7
2.2.3 Adiabatic jet expansion . . . 7
2.2.4 Droplet sizes and velocities . . . 9
2.2.5 Helium droplet doping . . . 10
2.3 Dopants inside helium droplets . . . 11
2.3.1 Transitions inside helium nanodroplets . . . 11
2.3.2 Location of the dopant . . . 12
2.4 REMPI spectroscopy . . . 13
2.5 Electronic structure of gold . . . 13
2.6 Computational methods . . . 14
2.6.1 Diatomic AuHe pair potentials . . . 15
2.6.2 Potentials for Au atoms inside the helium droplet . . . 15
2.6.3 Helium density functional theory calculations . . . 16
2.6.4 Ancilotto parameter λ_A . . . 16
2.6.5 Solvation energies . . . 17
2.6.6 Calculated excitation spectra . . . 17

3 Experimental setup 18
3.1 Description of the helium droplet apparatus . . . 18
3.1.1 Source chamber . . . 18
3.1.2 Pickup chamber . . . 18
3.1.3 Differential pumping stage . . . 19
3.1.4 Main chamber . . . 20
3.2 Laser set-up . . . 20
3.2.1 XeCl pump laser Radiant Dyes RD-EXC-200 . . . 21
3.2.2 Dye laser Lambda Physics FL3002 . . . 21
3.2.3 Laser dyes . . . 22
3.3 Time of flight mass spectrometer . . . 22
3.4 Acquisition of the spectra . . . 24

4 Results **27**
4.1 Theoretical results . . . 27
4.1.1 Diatomic AuHe pair potentials . . . 27
4.1.2 Location of the Au inside the He_N . . . 29
4.1.3 Calculated excitation spectra . . . 31
4.2 Experimental results . . . 31
4.2.1 In-droplet D1 line (37060 - 41000) cm^{-1} . . . 31
4.2.2 On the origin of $AuHe_n$ species . . . 36
4.2.3 Droplet size dependence - D1 line . . . 39
4.2.4 In-droplet D2 line (41000 - 43770) cm^{-1}) . . . 42
4.2.5 Droplet size dependence - D2 transition . . . 47
4.2.6 Gold oligomers . . . 48

5 Summary **52**

6 Appendix **55**
6.1 Settings chosen in the TOF spectrometer software . . . 55
6.2 Synchronized triggering of the devices . . . 56
6.3 XeCl pump laser Radiant Dyes RD-EXC-200 . . . 57
6.4 Setting up the Lambda Physics FL3002 dye laser . . . 58
6.4.1 Pump beam path . . . 61
6.4.2 Oscillator . . . 62
6.4.3 Preamplifier . . . 63
6.4.4 Intermediate telescope . . . 64
6.4.5 Main amplifier . . . 64
6.4.6 Power optimization . . . 65
6.4.7 SHG crystals . . . 66
6.4.8 Calibration of the BBO crystal . . . 67

Bibliography **69**

Danksagung **79**

List of Figures

2.1 Phase diagram of helium . . . 6
2.2 Average droplet sizes and diameters of helium nanodroplets produced by supersonic expansion . . . 8
2.3 Phase diagram of helium with isentropes for adiabatic cooling . . . 9
2.4 Grotrian diagram of atomic Au with 1CR2PI scheme . . . 14

3.1 Schematics of the nanodroplet synthesis apparatus . . . 19
3.2 Laser setup used for 1CR2PI spectroscopy . . . 21
3.3 Working principle of the time of flight mass spectrometer . . . 23
3.4 Details on the acquisition of the excitation spectra . . . 25
3.5 Example figure of the total acquired data . . . 26

4.1 Potential energy curves for AuHe . . . 29
4.2 Solvation energies of ground and excited state Au in a helium nanodroplet 30
4.3 Excitation spectrum of Au in helium nanodroplets containing the in-droplet D1 line (37060 - 41000 cm^{-1}) . . . 32
4.4 Grotrian diagram including excitation paths corresponding to the D1 energy 34
4.5 Ion yield as a function of the evaporation cell temperature for the in-droplet D1 line and the feature at the C1 atomic line . . . 38
4.6 Excitation spectra for different helium nanodroplet sizes containing the in-droplet D1 line (37060 - 41000 cm^{-1}) . . . 40
4.7 Excitation spectrum of Au in helium nanodroplets containing the in-droplet D2 line (41000 - 43770 cm^{-1}) . . . 42
4.8 Grotrian diagram including excitation paths corresponding to the D2 energy 45
4.9 Excitation spectra for different helium nanodroplet sizes containing the in-droplet D2 line (41000 - 43770 cm^{-1}) . . . 48
4.10 Time of flight mass spectrum for the largest Au doped helium nanodroplets 49
4.11 Oligomer excitation spectrum (41000 - 43770 cm^{-1}) . . . 50

6.1 Delays set in the KAESDORF RTF50 . . . 55
6.2 Sketch of the triggering between the different devices . . . 57
6.3 Components of the dye laser with optical path . . . 58
6.4 Tools for the adjustment of the Lambda Physics FL3002 dye laser . . . 60
6.5 Reference pictures for the adjustment of the Lambda Physics FL3002 dye laser . . . 60
6.6 Lambda Physics FL3002 oscillator . . . 62

Chapter 1

Introduction

The helium nanodroplet (He_N) synthesis technique has evolved as a powerful method for the production of small molecules and clusters [40, 58, 101] as well as the formation and deposition of larger nanoparticles [7, 32, 71, 99]. Historically, gold nanoparticles represent one of the most important and most studied classes of nanoparticles due to their biocompatibility, chemical and physical stability as well as the fact that they support surface plasmons [2]. These properties enabled many technological applications in a diversity of fields ranging from biology and medicine [44] to catalysis [1] and analytical chemistry [50]. Considering the great interest in particles containing gold as a constituent, it is not surprising that gold is also among the most frequently employed dopants in the helium nanodroplet assisted synthesis of nanoparticles [7, 62, 82, 106]. A peculiar advantage of the helium droplet approach in this regard is the possibility to study optical properties of dopants from the regime of atomic and molecular transitions [13] up to the regime characterized by localized surface plasmon resonances [22, 70]. Thus, the method may serve as a bottom up approach for the study of the electronic structure of Au nanoparticles and mixtures. This idea is addressed in the present work by studying the optical properties of Au oligomers, starting from individual gold atoms for which excitation spectra in helium nanodroplets are hitherto unknown.
For the coinage metal doped helium droplets $AgHe_N$ [68, 74] and $CuHe_N$ [67] transitions from the ^{2}S ground state into the lowest excited ^{2}P states have been explored. These transition appear strongly broadened and blue-shifted. In particular, for $AgHe_N$ where the spin-orbit splitting is large, separated transitions into a $^2P_{1/2}$ ($^2\Pi_{1/2}$) state and a $^2P_{3/2}$ ($^2\Pi_{3/2}$ and $^2\Sigma^+_{1/2}$) have been reported. Note that the coinage metals mimic the spectroscopic characteristics of alkali atoms [12] due to their closed d shell and the unpaired electron in the s shell. Their lowest optically allowed transitions are thus of $^2P \leftarrow {}^2S$ character to which we refer as D-lines in the following, in analogy to the alkali systems. However, in contrast to the alkalis, Cu and Ag are located inside the helium droplet and, according to recent calculations, also ground state gold atoms are expected to be located in the interior of the droplets [35]. A location of the atom inside the droplet typically gives rise to the observation of strongly blue-shifted valence electron transitions in the excitation spectra as a consequence of the strong repulsive interaction of the electron with the surrounding helium.
$AgHe_N$ [68, 74] and $CrHe_N$ [47, 48, 53] are important benchmark systems concerning the relaxation dynamics following photoexcitation of dopant atoms inside helium nanodrop-

lets. It was found that during such an excitation-relaxation process, the atoms can (i) desorb from the droplet as bare atoms or as dopant-He_n complexes or exciplexes, (ii) migrate to the surface of the droplet or (iii) remain solvated inside the droplet. Depending on the surrounding of the atom, a second excitation would show a characteristic broadening and energy-shift, increasing from (i) to (iii). For multi-photon based spectroscopy methods this can lead to very complex spectra, considering that after each excitation a relaxation to a different state and surrounding may take place. Consequently, the deciphering of the recorded spectra and the identification of dynamic pathways is often challenging because different relaxation channels can overlap or compete with each other, giving rise to a superposition of spectral features of different origin [74].
While gold nanoparticles have been synthesized in helium droplets previously [7, 62, 82, 106], gold atoms, molecules and small oligomers have not been subject to an experimental investigation and, in particular, their optical properties in helium droplets are unknown. However, these dopants have been subject to spectroscopic studies in bulk liquid and solid rare gas matrices, which can be compared to Au embedded in a helium droplet, aiding the interpretation of the recorded spectra (with some reservations due to the stronger interaction of solid matrices with the dopant, due to their anisotropy). For example in solid neon, xenon, krypton and argon matrices [31, 33, 64, 73] absorption spectra have been reported for the spectral region that contains the Au D-lines. For Au atoms in liquid and solid helium spectroscopic data is also available [80], however, not in the energy region of the lowest $^2P \leftarrow {}^2S$ transitions. An important result of the experiments with liquid and solid He matrices doped with isolated Au atoms is the strong relaxation of Au atoms into $^2D_{3/2}$ and $^2D_{5/2}$ states [80, 96].
In order to support the assignment of the recorded excitation spectra, computations for the $AuHe_N$ system have been carried out by Johann Pototschnig. In a first step *ab-initio* calculations have been realized, employing a multiconfigurational self consistend field (MCSCF) approach, followed by a multireference configuration interaction (MRCI) calculation. While AuHe diatomic potential energy curves have been reported previously [14, 15], here the ground state and several excited states were considered with a more balanced ansatz, using a large basis set also for excited states. Subsequently, the potential energy curves were applied to determine the solvation of Au atoms in different electronic states. The combination of optimized He densities and potential energy curves allowed to calculate spectral shifts as well as the broadening of transitions of interest.
As a starting point of this thesis, some fundamentals will be presented, including the basics of helium nanodroplet generation, resonantly enhanced multiphoton ionization (REMPI) spectroscopy, isolation spectroscopy, electronic structure of gold and a short summary of the procedure performed for the *ab-initio* calculations. Then the experimental setup is introduced piece by piece, starting with the helium droplet generation apparatus, followed by the laser setup and the time of flight (TOF) mass spectrometer. In the following chapter the results of the experimentally investigated $AuHe_N$ system (gold inside a heliumdroplet) are presented. In order to interpret the recorded spectra many comparisons to other Metal-He_N systems are made and the most relevant scenarios are expounded as possible explanations to the observed spectra. In this thesis, the focus was laid on the spectral regime that contains the lowest electronic $^2P \leftarrow {}^2S$

transitions of gold atoms embedded in helium nanodroplets, covering the spectral range from 37060 cm^{-1} to 43770 cm^{-1}. The in-droplet D1 and D2 line are discussed in separate sections, both have been recorded for three different droplet sizes. After discussing the spectra of isolated atoms, the excitation spectra of Au oligomers ranging from Au_2 to Au_9 are presented.

Chapter 2

Theoretical background

2.1 Historical background of matrix isolation spectroscopy

Here, a short introduction to the ideas of matrix isolation spectroscopy is given with the links that lead to the great advantages of helium nanodroplet isolation spectroscopy. The content is based on the PhD thesis of Markus Koch [52] and the master's thesis of Günter Krois [56].
The foundation of spectroscopy was layed in 1813 by Fraunhofer who discovered discrete lines in the spectrum of the sun. Since then, spectroscopic methods have been expanded and improved with many scientific applications. The most elementary access to spectral properties can be gained through gas (or atom) beam experiments, which provide insight into the electronic structure of atoms and molecules, the building blocks of matter. A big problem with these techniques is the limited applicability for compounds that cannot be brought into gas phase. Fragile species and molecules may not be stable in the gaseous state, or don't even form under the conditions, which are required to create an atomic or molecular beam. Matrix isolation provides a solution to this problem. This was first proposed by Whittle, Dows and Pimentel in 1954 [109], based on the suggestion of Vegard in 1924 [105] that nitrogen atoms isolated in an inert gas matrix experience only a weak perturbation and behave like free. The intent was to keep a reactive species in an inert environment to prevent reactions. A trapping of the atoms ought to be accomplished by very low temperatures of the surrounding matrix inhibiting diffusion processes. With this thought they were the first who could show that molecules embedded in a cold matrix do not react with each other. This was the starting point for the "matrix isolation" spectroscopy.
Since then, the technique evolved and greatly benefited by the invention of the laser, which made the investigation of many unstable substances and radicals possible. One way to realize modern matrix isolation experiments is by co-depositing the species of interest (guest) with an inert host material onto a cooled substrate (either transparent or high reflective). The cooled substrate acts as the cryostat, immobilizing the mixture of host and guest material, making it available for spectroscopic studies in transmission or reflectance. A big advantage is the possibility of long-term measurements due to the high stability of the systems. A disadvantage is the relatively strong influence of the host matrix on the electronic transitions, which makes sharp lines and high resolution

inaccessible. A matrix with a less perturbative character is helium. Helium has no solid phase at or below ambient pressure, therefore a solid matrix isolation requires a high pressure, making it unavailable for high vacuum experiments. However, helium possesses two liquid phases of which one is superfluid. Experiments in such surroundings are extremely interesting due to the weak interaction with the guest species and the unique insights it provides into the nature of superfluidity itself. The free movement however, would destroy the isolation property of the matrix, because over time guests will be lost, react with each other or stick to the cold vessel walls. This is a surmountable problem, if one considers a continuous flux of guest atoms or molecules where always new guests are produced. Also the control of the drift of charged guests with an electric field promises better stability [77]. In 1990 Goyal, Schutt and Scoles [29, 30] fundamentally solved this problem with another idea, namely that one could dope the guest species in a confined volume of the host matrix. With a single guest confined within one separated unit of the host matrix, there is no possibility of bond formation or reaction, because the only binding partner would be the host itself (which is not possible, due to the intrinsic inertness of the host). Experimentally this can be realized by the implementation of small host clusters or droplets prepared in high or ultra high vacuum. Here the isolation is not achieved by the immobilization of a cold solid matrix, but via the separation into small droplets and the doping with single compounds. This method fits the physical properties of helium perfectly, as cold (0.37 K) superfluid nanodroplets that are created using the adiabatic jet expansion scheme are accessible in many different sizes ($\sim$ nm - μm) as described at a later point [103].

2.2 Helium

Helium is the second most abundant element in the universe, even though the abundance in the lower atmosphere (troposphere) is just about 5 ppm. Nearly all helium resources on earth have their origin in the radioactive decay of uranium or other unstable isotopes, which involves the ejection of α-particles (He-cores). These α-particles capture electrons and are subsequently enriched in the natural gas, which is today's main helium resource. In natural gas up to 16 vol% helium can be found. Helium is used in cryo-experiments, for example for the cooling of superconducting coils in magnetic resonance imaging or particle accelerators. Also photo-detectors (e.g. x-ray or infrared detectors) sometimes need to be cooled to very low temperatures to increase sensitivity in terms of signal-to-noise ratio. Helium itself has also been subject to many experiments, taking into account its very special behaviour as a quantum fluid at low temperatures as well as its superfluidity. Yet other applications can be found in more common fields like in medicine as a breathing gas in a mixture with oxygen, in breathing gases for diving, in inert gas welding, as a lifting gas in balloons, in discharge tubes or as packaging gas in the food industry.

2.2.1 Physical and chemical properties of helium

Helium is the lightest and smallest inert gas in the periodic table. It has a closed 1s shell and is therefore very stable and non-reactive. The energetic difference of the helium ground state $1s^2\,{}^1S$ and the first excited state $1s2s\,{}^3S$ is 159856 cm^{-1} [54]. For the lowest allowed dipole transition from the ground state i.e. the $1s2p\,{}^1P \leftarrow 1s^2\,{}^1S$ transition, a photon with an energy of 171135 cm^{-1} [54] is needed. From this, one can already see, that cold helium is optically transparent in wide energy ranges. This is a required feature for matrix isolation spectroscopy as mentioned above. The phase diagram can be seen in figure 2.1. Helium condensates from the gas phase into a normal liquid phase at 4.15 K [118] under ambient pressure. Another phase transition to a superfluid state occurs at 2.17 K. At this so-called λ-transition the quantum mechanical wavefunction of the helium atom becomes larger than the mean interatomic distance, meaning that one cannot distinguish between single atoms any more. The liquid then exhibits a collective behaviour. Helium cannot be solidified at ambient pressure and it takes a minimum of 25 MPa to reach a solid phase. This is due to the zero-point energy of helium. This is the lowest energy the system can bear, but it is still too high for a phase transition to a solid. Liquid helium within a free helium droplet at 0.37 K has a binding energy of about 5 cm^{-1} [13], a very small value compared to the binding energies of the compounds that are targeted for spectroscopic studies inside these droplets.

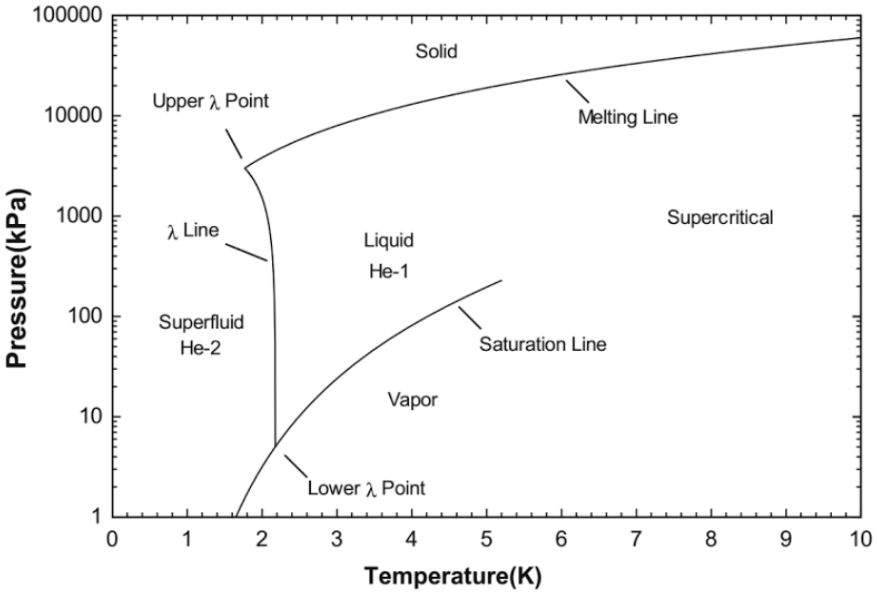

Figure 2.1: Phase diagram of helium taken from ref. [63]. The λ line separates the normal liquid (He-1) from the superfluid (He-2) phase.

2.2.2 Helium droplets

Cold, superfluid helium droplets offer an extraordinary basis for spectroscopic studies as explained above. Helium droplets have been reviewed several times in the past [13, 95, 102, 103, 104]. The method of producing these droplets is well established and shall be presented in the following. There are different methods of creating helium droplets, but for spectroscopic purposes mainly helium droplet beams produced by a free jet expansion are used. These droplets have sizes from a few nm to μm, bridging the gap between atoms and the bulk. Dopants injected into these helium droplets are cooled down by the evaporation of weakly bound helium atoms. A peculiarity of the cold superfluid droplets is the formation of quantized vortices, which have been originally observed for bulk helium [6, 111, 116]. For larger droplets it has been shown that vortices are also formed [27, 28]. Due to a helium density gradient dopants are attracted to the center of these vortices. This is used for the one-dimensional growth of nano-rods and wires [28, 62, 93, 99, 106]. In spectroscopic studies such vortices may create an additional isolation effect, due to the separation of dopants at different vortices, as vortices tend to crystallize in a periodic lattice, where they do not overlap [27]. However, the usage of very big droplets in not very common in spectroscopy.

2.2.3 Adiabatic jet expansion

A beam of helium droplets is created by the adiabatic expansion of pressurized, cold helium gas through a very small nozzle into high vacuum. During the passing of the nozzle, the mean free path of the helium atoms is much smaller than the nozzle diameter, which leads to a lot of collisions. This is crucial for efficient energy exchange and therefore adiabatic cooling. Depending on the starting conditions, the atoms may have supersonic velocities during the gas expansion, which leads to barrel-like shockwaves that constrict the beam. Shortly after the nozzle, when the temperature of the helium gas is sufficiently low, the gas condensates to the liquid phase i.e. droplets. When the collision frequency is lowered due to the lower density the expansion, collision cooling stops and evaporative cooling dominates the further temperature reduction. It was found that the final temperature of the droplets is 0.37 K [13]. The droplets exhibit a very distinct, narrow velocity distribution in forward direction (200 - 400 m/s) [103]. Internal velocities of atoms within a droplet are given by the thermal movement of the cold helium atoms.
Depending on the source conditions (nozzle diameter, stagnation pressure p_0, stagnation temperature T_0) the process of droplet formation can be described by different effects. As the process is adiabatic, the expansion follows isentropes and crosses different lines in the phase diagram. There are mainly three different formation processes involved in the creation of the droplets (cf. figure 2.2, 2.3):

1. Condensation of gas: In a supersonic expansion gaseous helium is adiabatically expanded and condensates to small droplets directly from the gaseous phase into the fluid He I or superfluid He II phase. This expansion is subcritical because the isentropes lie clearly in the gaseous part of the phase diagram. Therefore they

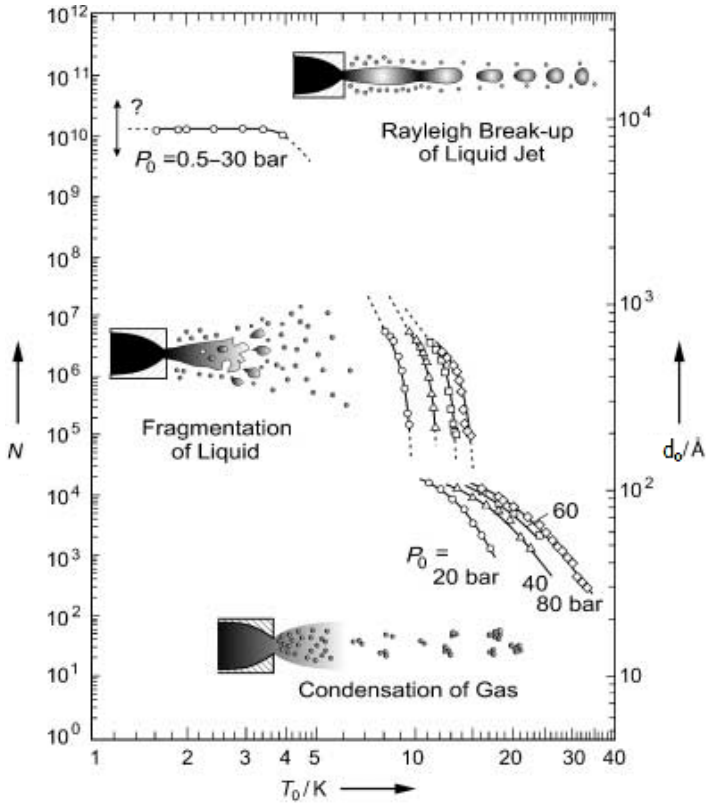

Figure 2.2: The average number of helium atoms per droplet N with the corresponding mean diameters d_0 as a function of the stagnation pressure p_0 and temperature T_0. The temperature range divides into three regions, each related to a different formation process. Taken from ref. [103].

are straight lines, as expected for an ideal gas. Through evaporative cooling the helium droplets are cooled to their final temperature of 0.37 K (figure 2.3, Regime I, $T_0 > 12$ K).

2. Fragmentation of a liquid: In this case a supercritical expansion takes place, where liquid helium (He I) is expanded through the nozzle but due to a crossing of the coexistence region of liquid (He I) and gas the liquid fragments into smaller droplets. The droplets are also cooled to their final temperature via evaporation cooling (figure 2.3, Regime III, 3 K $< T_0 <$ 8 K).

3. Rayleigh break-up of a liquid jet: The liquid helium is so cold, that it is expands as a liquid jet (from He I directly to He II), not fragmenting into droplets. Only due to Rayleigh-oscillations the stream breaks up into large helium droplets, that are cooled further down by evaporation of helium atoms (figure 2.3, Regime III, $T_0 < 3$ K).

The isentropes in regime II in figure 2.3 (8 K $< T_0 <$ 12 K) pass near the critical point, which makes their behaviour unstable and fluctuating.

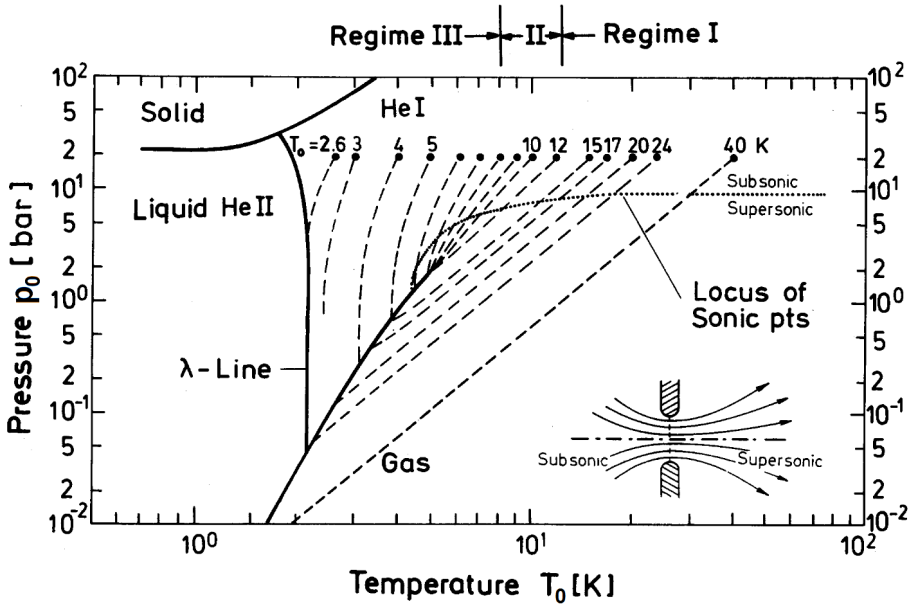

Figure 2.3: Phase diagram of helium taken from [10]. The λ line marks the transition from normal liquid (He I) to superliquid (He II) helium. The adiabatic expansion follows isentropes, drawn as dashed lines. The stagnation temperature is written on the starting point of the dashed isentropes. The stagnation pressure is 20 bar. Regime I corresponds to isentropes at the high temperature side of the critical point; Regime II corresponds to isentropes through or near the critical point; Regime III corresponds to isentropes at the low temperature side of the critical point. For each regime very specific characteristics can be observed. The dotted line marks the sonic points (where the helium atoms have sonic velocity) and therefore specifies the state at the nozzle for adiabatic expansions.

2.2.4 Droplet sizes and velocities

Sizes of helium droplets created by the method described above have been measured by different techniques such as deflection upon atom scattering [34, 66] or deflection of negatively charged droplets in an electric field [51]. The mean diameter d_0, as well as the mean number of atoms N of the helium droplets at different stagnation temperatures T_0 and pressures p_0 are shown in figure 2.2. In this figure it can be seen that with colder stagnation temperatures the droplet size increases. The temperature dependence is characteristic for each expansion mechanism (Condensation of gas; fragmentation of liquid; Rayleigh break-up). Furthermore, it was found that the sizes of the droplets obey a logarithmic normal distribution [34, 66]. Written for the number of He atoms within a droplet $\widetilde{N}$, the probability density function reads

$$p(\widetilde{N}) = \frac{1}{\sqrt{2\pi}\widetilde{N}\sigma}\exp\left(-\frac{(ln(\widetilde{N})-\mu)^2}{2\sigma^2}\right), \tag{2.1}$$

where μ is the mean value of $ln(\widetilde{N})$ and σ is the standard deviation of $ln(\widetilde{N})$. The mean number per helium droplet is then:

$$N = \exp\left(\mu + \frac{\sigma^2}{2}\right). \tag{2.2}$$

As the expansion is an adiabatic process, no energy is lost and all the enthalpy H_0 is converted into kinetic energy (For cooling to 0 K).

$$H_0 = \frac{5}{2} k_B T_0 = \frac{m_{He} v^2}{2} \tag{2.3}$$

Subsequently, the velocity v can be written as

$$v = \sqrt{\frac{5 k_B T_0}{m_{He}}}, \tag{2.4}$$

where k_B is the Boltzmann's constant, T_0 the stagnation temperature and m_{He} the mass of the helium atom. This is of course an estimation for an ideal gas. For low stagnation temperatures, where a crossing of the liquid-gaseous phase takes place, the remaining enthalpy of the lower λ-point has to be considered.

2.2.5 Helium droplet doping

Helium droplets can be doped with many different species, due to an attractive potential that binds the dopant to the helium droplet. In the doping process, the helium droplet beam passes a region with gas phase dopant atoms or molecules. Through collision, single dopants are captured and carried along by the helium droplets. To confine the region of this so-called pickup and avoid the escape of bare dopants, which may interfere with measurements done on the helium droplets, the entrance and exit of the pickup cells are fitted with small apertures, in the size of the helium beam diameter. The pickup itself is a statistic process, hence the mean number of atoms that are picked up is dictated by the cross-section of the droplets (i.e. size) and the vapour pressure of the dopant, which should be picked up.
The only limiting factor for applicability is the ability to bring compounds into gas phase, which can be complicated for high melting materials like tungsten or carbon. Furthermore, for fragile compounds a temperature induced evaporation may lead to fragmentation or decomposition. With the employed pickup cells (tungsten with ceramic alumina coating) temperatures up to 1500 °C can be reached. Other evaporative sources can be realized via electron bombardment heating, inductive heating or laser ablation. When a dopant enters a helium droplet, the energy carried by the dopant is transferred to the helium surrounding. Multiple dopants attract each other via long range Van der Waals forces. When they get close enough, binding can occur. The energy released upon bond formation is dissipated by the helium droplet through evaporative cooling. With this method it is possible to prepare exotic compounds, which may not form under different circumstances. For these compounds the helium droplet approach offers a soft

environment of low-perturbing nature. An important parameter in these cases is the number of atoms that can be picked up by the helium droplet. The cooling of hot metal atoms and the energy released due to binding has to be absorbed. As a consequence, helium atoms are evaporated into the vacuum. For the maximum number of atoms that can be picked up this estimation can be stated:

$$n = \frac{E_{He}}{\frac{3}{2}k_B T + E_{bind}} N, \tag{2.5}$$

where n is the number of metal atoms in the cluster, N is the number of helium atoms per droplet, E_{He} is the energy with which a helium atom is bound to the helium droplet, E_{bind} is the energy released when an atom binds to an existing metal cluster, k_B is the Boltzmann constant and T is the temperature of the evaporated metal atoms.

2.3 Dopants inside helium droplets

Helium nanodroplets offer a wide palette of unique physical and chemical properties. Their inertness, extremely low temperature, and superfluidity make them perfect cryo nano laboratories. For spectroscopic studies, especially the low temperatures are of great importance, because it ensures that the dopant atoms and molecules are in a distinct, very low energetic state i.e. the ground state. Starting from this well defined initial state various experiments like excitations or induced reactions can be investigated.

2.3.1 Transitions inside helium nanodroplets

For free atoms excited by a single photon, dipole selection rules apply, as angular momentum and spin are conserved quantities. These rules are expressed in terms of the quantum numbers L (total orbital angular momentum), l (orbital angular momentum of a single electron), J (total angular momentum) and S (total spin).

$$\Delta L = 0, \pm 1 \quad (\Delta l = \pm 1 \text{ for single electron transitions})$$

$$\Delta J = 0, \pm 1$$

$$\Delta S = 0$$

$$\text{if } \Delta S = \pm 1 \quad \rightarrow \quad \Delta L = 0, \pm 1, \pm 2 \quad \text{(for heavy atoms only)}$$

The ΔL (Δl) and ΔJ selection rules are due to the angular momentum conservation, as the photon has a nonzero spin of $S = 1$. The selection rule $\Delta S = 0$ is valid for light atoms where spin-orbit coupling is weak and the electronic wavefunction can be written as a product of space and spin function. $\Delta S = \pm 1$ is possible for atoms with large spin-orbit coupling due to intercombination between different multiplett systems. However, the transition probability is typically lower than in the case of $\Delta S = 0$.
On account of the interaction of dopants with the helium surrounding, optical dipole

selection rules are known to be softened. This is due to a change of the "good" quantum numbers of the system i.e. quantum numbers that describe the state of the system well. The total orbital angular momentum L appears to be a quantum number that does not correspond to a "good" quantum number any more inside the helium droplet. As only selection rules that refer to "good" quantum numbers have to hold, the $\Delta L = 0, \pm 1$ selection rule ($\Delta l = \pm 1$ for single electron transitions) weakens. This makes it possible to examine transitions that are normally not allowed in the free compound. For example, transitions forbidden in the bare atom, such as ^{2}D $\leftarrow^2$ S have been observed for Au in liquid and solid helium matrices [79, 80]. However, the $\Delta J = 0, \pm 1$ selection rule is still expected to apply, regardless of the type of coupling between the helium and the Au atom (this has been observed for example, for transitions in Cs atoms located on the surface of helium nanodropelts [59]). Another effect of the helium surrounding is the shift and broadening of dopant transitions. The shift originates from a repulsive or attractive interaction of the final state in the helium surrounding. In this context, it is helpful to introduce the so-called atomic bubble theory [25, 49, 97]. In this theory the dopant is accommodated inside a helium-free bubble inside the droplet. If a dopant is excited or relaxes upon the absorption or emission of a photon, the occupation of the the individual orbitals changes. This corresponds to a change in size of the dopant's electron shell, which now needs more or less space inside the helium droplet. As the electronic excitation is a lot faster than the rearrangement of the helium atoms, one can treat the helium bubble as static (v.i. frozen droplet approximation). The interaction of the excited electron shell with the unrelaxed helium surrounding is then related to a distinct energy shift of the transition. The broadening can be explained by so-called bubble oscillations. As the name indicates the helium-free bubble oscillates around the dopant, distorting the state of equilibrium. Depending on the current state and symmetry of the bubble, the shift of the transition is different. A weighted integration over all possible oscillation modes leads to the overall broadening of the transition. As a result of this broadening, it is impossible in most cases to resolve rotational transitions and also vibrational transitions are strongly shifted, making it hard to measure or assign them.
Another interesting feature of the helium surrounding is the strong increase of the relaxation dynamics. In a lot of dopant-He systems enhanced relaxation was observed, such as AgHe [68, 74] and CrHe [47, 48, 53], where a lot of lower lying states were found to be populated upon initial photo excitation. In every excitation or relaxation study this may lead to overlapping features, that originate from these lower states. For example, in works concerning Au in liquid helium matrices [96], it has been found that upon photo excitation, no emission from the initially populated state was measured due to the competing, non-radiative, relaxation pathways.

2.3.2 Location of the dopant

It is known that different dopants may prefer different locations when immersed into helium nanodroplets. This depends on the energetic gains and losses due to electronic interaction, surface and volume energy. Dopants can either be stable inside the helium

droplet, be trapped at the surface, or get straight ejected out of the droplet. It is clear, that the interaction with the helium is a lot weaker at the edge than inside the droplet. Therefore, broadening effects and energy shifts are expected to be smaller at the surface.

2.4 REMPI spectroscopy

Resonant enhanced multiphoton ionization (REMPI) spectroscopy is a powerful method to probe the optical properties of atoms and molecules. (n+m)-REMPI describes a multiphotonic ionization path, where n photons are needed to resonantly excite the intermediate state and m photons to ionize it. The probed state is the intermediate state, because the ion yield increases dramatically when it is resonantly excited. In contrast, a direct ionization without a resonant intermediate state is very unlikely. REMPI can either be realized with just one laser color (1CREMPI), or two different laser colors (2CREMPI) for excitation and ionization. The easiest way to perform REMPI is the (1+1)-REMPI sheme, where just two photons are involved in the overall ionization process (R2PI). In REMPI there are always multiple photons involved in the ionization process, thus the transition probability has a nonlinear dependence on the laser intensity. In general, it is proportional to I^k [5], where I is the laser intensity and k is the nonlinearity of the ionization process. For low intensities, where no saturation effects take place, k can be set to the number of photons participating in the ionization. Hence, for R2PI spectroscopy the yield should be a quadratic function of the laser intensity. In REMPI the produced ions are detected via a quadrupole or TOF mass spectrometer. The detection of the photoelectrons can give additional information, because the electron carries kinetic energy equal to the excess energy involved in the ionization process. The disadvantage is that the origin of the photoelectron cannot be assigned assuredly. In the experiments presented in this work, 1CR2PI spectroscopy in the energy range from 37060 to 43770 cm^{-1} was employed to study the optical properties of Au inside helium nanodroplets.

2.5 Electronic structure of gold

Au has an electron configuration of $[Xe]4f^{14}5d^{10}6s$ and has therefore a similar electronic structure to the alkali atoms with its single 6s electron in the outermost shell. Single s-shell systems are easy to describe and may serve as benchmark systems for other, more complex systems. Atomic gold has an ionization potential of 74409 cm^{-1} [54]. Thus, 1CR2PI spectroscopy is feasible for the atom starting from 37205 cm^{-1} and, consequently, the $6p\,^2P_{1/2} \leftarrow 6s\,^2S_{1/2}$ transition ($\overline{\nu}$ = 37359 cm^{-1}) is the lowest lying state that can be studied employing a 1CR2PI scheme. The Grotrian diagram of atomic gold with the ionization scheme is displayed in figure 2.4. The D1 and D2 transitions (corresponding to the $^2P_{1/2} \leftarrow {}^2S_{1/2}$ and $^2P_{3/2} \leftarrow {}^2S_{1/2}$ transition) are displayed as the main transitions that can be probed with the energy range used in the experiment (grey area). The third transition that falls into the grey probable area is the $^4P_{5/2} \leftarrow {}^2S_{1/2}$

transition. The yield of this line is supposed to be very low, as the $\Delta J = 0, \pm 1$ selection rule is violated. It has been found that the ionization potential is shifted to lower photon energies due to the influence of the surrounding helium for species inside helium nanodroplets. This shift is droplet size dependent and is on the order of a few 100 cm^{-1}. For example, a decrease of about 700 - 800 cm^{-1} has been determined for aniline in helium droplets with diameters ranging from 4 to 12 nm, respectively [72].

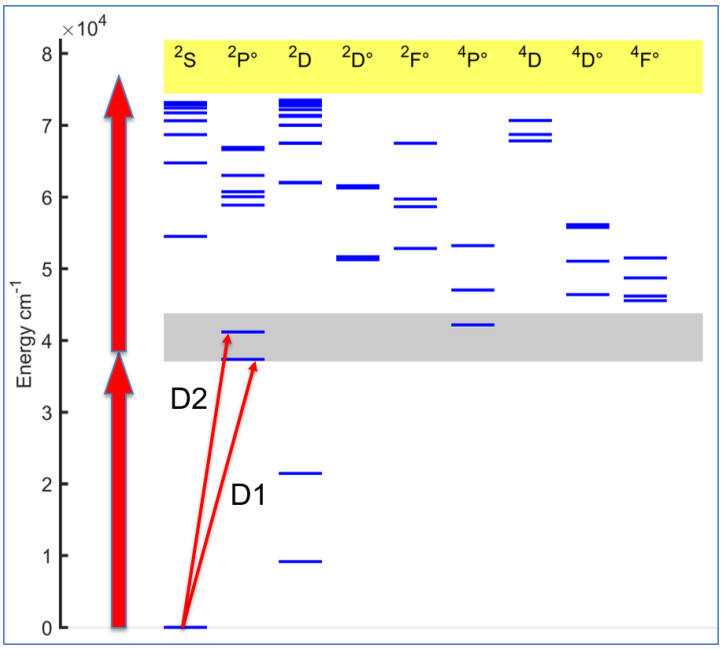

Figure 2.4: Grotrian diagram of Au. The states (blue horizontal lines) are sorted corresponding to their total orbital angular momentum L, their total spin S and their parity (° for odd, no superscript for even) i.e. $^{2S+1}L^{\circ}$. The yellow area marks the ionization regime. The thick red arrows on the left demonstrate the 1CR2PI scheme, with the grey area being the probed energy region in the conducted experiments. D1 and D2 mark transitions from the ground state into the lowest lying doublet P states, namely the $^2P_{1/2} \leftarrow {}^2S_{1/2}$ and $^2P_{3/2} \leftarrow {}^2S_{1/2}$ transitions. The energies of the electronic states are taken from ref. [54].

2.6 Computational methods

Computations in order to model, interpret or predict experimental findings are an important and powerful tool in today's scientific world. In the following, the required instruments for the *ab initio* spectroscopic description of complex dopant-heliumdroplet systems and more specific the $AuHe_N$ system are introduced and explained. This will cover the AuHe diatomic potentials, the angular dependent potentials for Au in a helium surrounding as well as helium density functional theory calculations to get solvation

energies and excitation spectra. All hypotheses, considerations, calculations and evaluations are accredited to Johann Pototschnig. Due to the author's lack of expertise in this kind of field, the following sections of chapter 2 concerning the calculations can be considered to be quotations of Johann Pototschnig.

2.6.1 Diatomic AuHe pair potentials

The most important ingredients for the characterization of any dopant inside the helium nanodroplets is the diatomic pair potential (in the case of dopant atoms). In the following the main focus will lie on the description of the AuHe system as it was the system that was investigated experimentally in this work. Potential energy curves for different states of the AuHe diatom have already been calculated in previous publications [14, 15]. To build up a new, consistent model of the AuHe system new calculations were performed, starting with the potentials by using a different approach than in [14, 15]. The potential energy curves were obtained using a multiconfigurational self consistent field (MCSCF) calculation followed by a multireference configuration interaction (MRCI) calculation. The advantage of using a multireference instead of a singlereference method, as used in the computations mentioned above [14, 15], is that the dissociation and degenerate or quasi-degenerate excited states can be described. A state-averaged MCSCF was applied, which treats the considered states equally. The He atom was described by the aug-cc-pV5Z basis set [113], for Au the aug-cc-pwCV5Z-PP basis set [86] was employed with the recommended effective core potentials [24]. In the previous computations [14, 15] the excited states were treated with a triple-zeta basis set, while the ground state was extrapolated to the basis limit. In the spin-averaged MCSCF computation the electronically excited state corresponding to the ^{2}S, ^{2}D, ^{2}P and ^{4}P asymptotes were considered. Spin-orbit interaction was included for the lower three asymptotes using the Breit-Pauli Hamiltonian and relativistic effective core potentials [24]. All computations were performed using the MOLPRO software package [108]. Note that these energy potentials inhibit a one dimensional character and are therefore not suitable to describe the interation of a single dopant in helium surrounding.

2.6.2 Potentials for Au atoms inside the helium droplet

To calculate three dimensional potentials of Au inside the helium droplet, the approach presented by by Bünermann *et al.* [12] is used. In this method the spin-orbit split one-dimensional AuHe potentials are used with the rotational Wigner D matrix [110] to create angular dependent potentials for each spin-orbit split state. The potentials for

the $^2P_{1/2}$ and $^2P_{3/2}$ asymptotes read as follows:

$$V_{\Pi'_{1/2}}(\Theta) = V_{\Pi_{1/2}} \tag{2.6}$$

$$V_{\Sigma'_{1/2}}(\Theta) = \frac{1}{8}\left(5V_{\Pi_{3/2}} + 3V_{\Sigma^+_{1/2}} + 3(V_{\Pi_{3/2}} - V_{\Sigma^+_{1/2}})\cos(2\Theta)\right) \tag{2.7}$$

$$V_{\Pi'_{3/2}}(\Theta) = \frac{1}{8}\left(3V_{\Pi_{3/2}} + 5V_{\Sigma^+_{1/2}} - 3(V_{\Pi_{3/2}} - V_{\Sigma^+_{1/2}})\cos(2\Theta)\right) \tag{2.8}$$

These expressions were obtained using MATHEMATICA [112]. The potentials without prime are the spin-orbit split diatomic potentials. The primed quantities are the potentials for the dopant and a He atom of the droplet. Additional to the internuclear distance they now have an angular dependence Θ. Note, that the third coordinate is irrelevant, because of the cylindrical symmetry of the system. For the $^2D_{5/2}$ and $^2D_{3/2}$ asymptotes the following equations were employed:

$$\begin{aligned} V_{\Delta'_{5/2}}(\Theta) =& \frac{1}{128}\left(63V_{\Delta_{5/2}} + 35V_{\Pi_{3/2}} + 30V_{\Sigma^+_{1/2}} + 20\left(3V_{\Delta_{5/2}} - V_{\Pi_{3/2}} - 2V_{\Sigma^+_{1/2}}\right)\cos(2\Theta)\right. \\ &\left. +5\left(V_{\Delta_{5/2}} - 3V_{\Pi_{3/2}} + 2V_{\Sigma^+_{1/2}}\right)\cos(4\Theta)\right) \end{aligned} \tag{2.9}$$

$$\begin{aligned} V_{\Pi'_{3/2}}(\Theta) =& \frac{1}{128}\left(35V_{\Delta_{5/2}} + 55V_{\Pi_{3/2}} + 38V_{\Sigma^+_{1/2}} - 4\left(5V_{\Delta_{5/2}} - 7V_{\Pi_{3/2}} + 2V_{\Sigma^+_{1/2}}\right)\cos(2\Theta)\right. \\ &\left. -15\left(V_{\Delta_{5/2}} - 3V_{\Pi_{3/2}} + 2V_{\Sigma^+_{1/2}}\right)\cos(4\Theta)\right) \end{aligned} \tag{2.10}$$

$$\begin{aligned} V_{\Sigma'_{1/2}}(\Theta) =& \frac{1}{64}\left(15V_{\Delta_{5/2}} + 19V_{\Pi_{3/2}} + 30V_{\Sigma^+_{1/2}} - 4\left(5V_{\Delta_{5/2}} + V_{\Pi_{3/2}} - 6V_{\Sigma^+_{1/2}}\right)\cos(2\Theta)\right. \\ &\left. +5\left(V_{\Delta_{5/2}} - 3V_{\Pi_{3/2}} + 2V_{\Sigma^+_{1/2}}\right)\cos(4\Theta)\right) \end{aligned} \tag{2.11}$$

$$V_{\Delta'_{3/2}}(\Theta) = \frac{1}{8}\left(5V_{\Delta_{3/2}} + 3V_{\Pi_{1/2}} + 3\left(V_{\Delta_{3/2}} - V_{\Pi_{1/2}}\right)\cos(2\Theta)\right) \tag{2.12}$$

$$V_{\Pi'_{1/2}}(\Theta) = \frac{1}{8}\left(3V_{\Delta_{3/2}} + 5V_{\Pi_{1/2}} - 3\left(V_{\Delta_{3/2}} - V_{\Pi_{1/2}}\right)\cos(2\Theta)\right) \tag{2.13}$$

2.6.3 Helium density functional theory calculations

The angular dependent potential energy curves were then applied in a density functional calculation for the bosonic helium (Helium-DFT) based on the Orsay-Trento functional [17]. For states with a strong interaction, the modifications developed by Ancilotto *et al.* in [3] were used. This approach allows to calculate He density distribution for a specific Au electronic configuration as well as the total energy of the $AuHe_N$ system. In all the calculations employed for this work droplets with 10^4 He atoms were considered.

2.6.4 Ancilotto parameter λ_A

To assess the preferred location of a dopant interacting with a helium nanodroplet, the easiest prediction can be given with the Ancilotto parameter [4, 91]. This dimension-

less quantity estimates the location, using the ratio of the energy gain due to dopant-matrix interaction (dopant-helium binding) and the energy loss due to the formation of a helium-free bubble inside the helium droplet, where an additional surface is created. The parameter can be calculated from diatomic dopant-He pair potentials. If $\lambda_A > 1.9$, the dopant is supposed to be stable inside the helium droplet. For $\lambda_A < 1.9$ the dopant is likely to be at the surface according to Ancilotto *et al.* [4].

2.6.5 Solvation energies

A more sophisticated approach in order to determine the preferred location of a dopant is through helium-DFT calculations. Solvation energies are calculated by subtracting the energy of an empty helium droplet from the energy of a doped helium droplet as a function of the dopant's position. From the results, one can directly see the energy gain or loss of the system for distinct dopant locations. Negative energies stand for more stable constellations, whereas positive energies describe a repulsive configuration. In a relaxed system, the dopant is situated at the position of the global energy minimum. These minima are strongly correlated to the atomic state of the dopant, therefore excitation or relaxation of an immersed atom can lead to interesting features such as dopant ejection. However, as this is a static calculation, it may not explain all dynamic effects. In this work for example, the ejection of ^{2}D state exciplexes was observed, although the solvation energy calculation suggested an immersion inside the helium droplet.

2.6.6 Calculated excitation spectra

For atoms inside a helium droplet valence electron transitions are broadened and, typically, blue-shifted due to the repulsive interaction between the electron that is subject to excitation and the surrounding helium. The shifts of transition energies inside the helium droplet can be obtained using the frozen droplet approximation, which assumes that the helium droplet density does not rearrange during the excitation process. The assumption that the electronic transition proceeds a lot faster than the relaxation of the helium density seems reasonable due to the large mass difference of the electron compared to the He atoms. The shift is then given by the difference of the ground state potential and the ones defined in equation 2.6 - 2.13 weighted by the He density. In the ground state the Au atom is defined to be located within the droplet and a broadening of the transition is caused by fluctuations of the helium density surrounding the dopant. These bubble oscillations can be taken into account in order to obtain the line broadening as it was done in ref. [91]. In this work the approach of Hernando *et al.* (see ref. [37]) is used and the breathing mode as well as quadrupole oscillations are considered. The bubble wave function was determined using the formulas in ref. [37] and different bubble states were drawn from the probability given by the square of this wave function. The shift for each state was then computed and the spectrum was obtained from the distribution of these shifts.

Chapter 3

Experimental setup

3.1 Description of the helium droplet apparatus

The apparatus which was used to create the helium droplets in displayed is figure 3.1. In principle, the device consists of three vacuum chambers: The source chamber, the pick-up chamber and the main chamber. All chambers are connected via flanges with small skimmers to enable individual semi-decoupled pressure conditions. The approximate chamber pressures are included in figure 3.1.

3.1.1 Source chamber

In the source chamber, grade six Helium (99.9999 % He) is cooled down by a closed cycle refrigerator, Sumitomo RDK-408D2, to a temperature below 20 K. It is then expanded from overpressure into high vacuum through a 5 μm nozzle. An adiabatic (supersonic) expansion takes place, which cools down the He to about 0.37 K [13]. During this process a beam of superfluid droplets with a distinct size distribution is formed as described in section 2. For a fixed stagnation pressure p_0, the size distribution depends only on the nozzle temperature T_0 (mean droplet sizes can be extracted from figure 2.2). The droplets created by this process increase in diameter as well as in number of atoms per droplet, when the stagnation temperature is reduced or the stagnation pressure is increased. It is important to know that the absolute helium flux increases dramatically with decreasing temperatures due to a change in viscosity (gas-liquid-superfluid) and ejection mechanism. After the formation the beam is collimated by a 0.4 mm skimmer and guided to the next chamber. For this work three different settings for the jet expansion were used. They are listed in table 3.1.

3.1.2 Pickup chamber

In this chamber two resistively heated evaporation cells are utilized to evaporate metal atoms. When the helium beam passes through these cells, metal atoms are picked up. This is a statistic process, where the number of dopant atoms inside a single droplet is correlated to the cross-section of the droplet and the adjusted metal vapour pressure. Depending on the pick-up statistics many different mechanisms take place afterwards. If the vapour pressure is very low, only few atoms are picked up. In such systems the

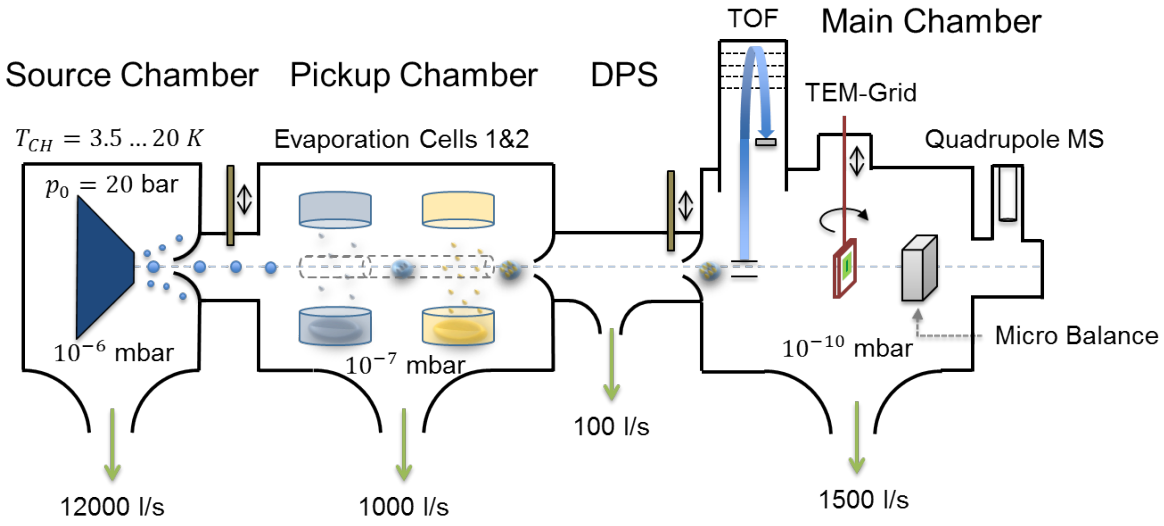

Figure 3.1: Schematics of the nanodroplet synthesis apparatus, consisting of four chambers: Source chamber: Here pressurized, cooled helium gas is expanded into high vacuum through a nozzle with a diameter of 5 μm. Due to a process of supersonic expansion and adiabatic cooling, a beam of superfluid helium droplets with a temperature of about 0.37 K is formed, which is guided through the entire apperatus. Pickup chamber: In the evaporation cells metals are heated and evaporated. The free metal atoms are captured by the passing helium droplets. Differential pumping stage (DPS): This additional pumped chamber is implemented to improve the pressure in the subsequent chamber by flattening the pressure gradient. Main chamber: In this chamber the produced helium droplets doped with metal atoms and clusters are investigated by probing them with different techniques (TOF spectrometer, micro balance, QMS and applications for depositions on different substrates (cf. [98]). This picture was taken from ref. [92].

interaction between the dopant and the helium droplet He_N can be explored. If more atoms are picked up, they agglomerate to bigger clusters and wires. In contrast to previous works [93, 98, 99, 106] from Cluster Lab III that focused on the generation of large nanoparticles, the oven temperature in the present work was optimized for a maximum number of helium droplets that only contain a single Au atom at a nozzle temperature of 15 K.

3.1.3 Differential pumping stage

A differential pumping stage (DPS) is commonly used to separate two pressure regions from each other. The pickup chamber cannot be pumped to ultra high vacuum ($\sim 10^{-10}$ mbar) because of the high temperatures of the pickup cells that goes along with increased pressures, in particular, caused by the evaporated metal atoms effusing out of

Table 3.1: Expansion settings used for the experiments conducted within this work. With the stagnation pressure p_0, the stagnation temperature T_0, the mean helium droplet diameter d_0 and the mean number of helium atoms per droplet N.

p_0 [bar]	T_0 [K]	d_0 [nm] [103]	N [atoms] [103]
60	17	9	9 x 10^3
60	15	10	1.25 x 10^4
60	12	50	2 x 10^6

the cells. To operate different diagnostic tools in a highly inert surrounding, ultra high vacuum is maintained in the main chamber. The DPS is equipped with two skimmers, one at the entrance and one at the exit. An effusive beam of metal atoms is strongly suppressed and also atoms and particles colliding with the walls have a high probability to get evacuated by the pump in the DPS.

3.1.4 Main chamber

In the main chamber, the lowest pressure conditions ($\sim 10^{-10}$ mbar) of the apparatus are achieved. A very inert surrounding with a low surface impact rate is the result. Here, the produced species are examined via a variety of different tools. The *in-situ* instruments include a time of flight mass spectrometer, for the in-flight investigation of the produced species. This is most practicable for smaller clusters, as the yield for a single mass (or cluster size) decreases with increasing cluster sizes [60]. To determine the integrated mass of all the created clusters per second (μg/s), a quartz microbalance is employed. Here only the total mass flux of relatively large clusters can be detected. The last *in-situ* instrument is a quadrupole mass spectrometer (QMS), mounted off-axis of the helium droplet beam, which acts as a residual gas analyser for helium. With this QMS it is possible to monitor the evaporation of helium atoms upon metal atom pickup and bond formation (cf. equation 2.5). The *ex-situ* tools include a transmission electron microscope (TEM) grid-holder and a vacuum transfer device for potential other *ex-situ* examinations, without breaking the vacuum.

3.2 Laser set-up

For the resonant ionization of the gold atoms and oligomers inside helium nanodroplets a laser was utilized. The setup consists of a XeCl excimer laser system that pumps a frequency doubled dye laser. The whole setup is explained in the following. A schematic diagram of the laser setup is showed in figure 3.2. Note that this is the first work that utilizes this laser system in Cluster Lab III.

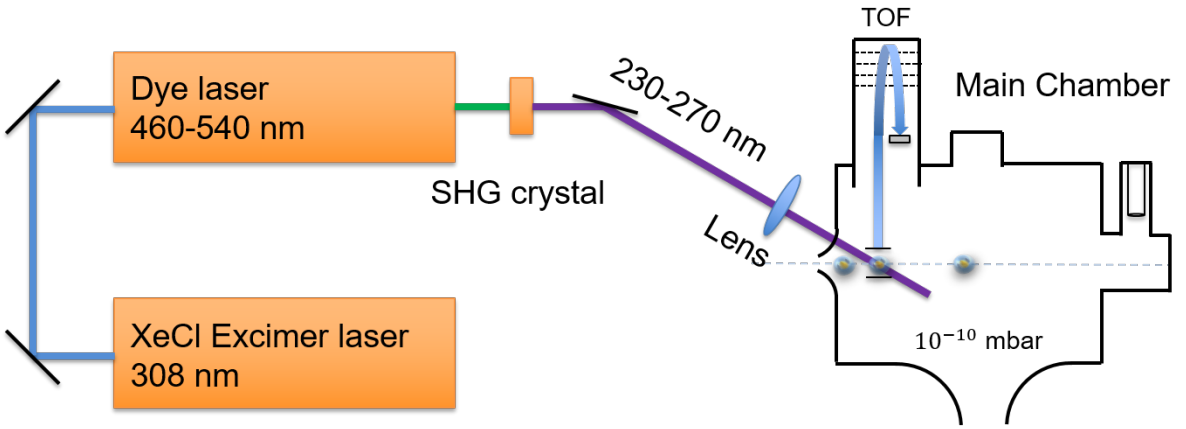

Figure 3.2: A schematic diagram of the laser setup. On the left the used lasers are displayed. On the right the main chamber is shown, with the helium droplet beam crossing the laser beam in the extraction region of the TOF mass spectrometer.

3.2.1 XeCl pump laser Radiant Dyes RD-EXC-200

As a pump laser a Radiant Dyes RD-EXC-200 XeCl excimer laser with a fixed wavelength of 308 nm is used. This laser has a pulse duration of about 25 ns and a maximal repetition rate of 100 Hz. The laser is filled with about 3200 mbar of a gas mixture with 1.97 vol% Xenon, 0.12 vol% Hydrogen Chloride and Neon as a buffer gas. The laser gas is decaying throughout the usage and has to be refilled after six million laser pulses. Within the conducted experiments the output power of this laser varied between 70 to 110 mJ. Three dichroic mirrors (308 nm) are used to guide the rectangular shaped (25 x 50 mm) pump laser pulses to the dye laser.

3.2.2 Dye laser Lambda Physics FL3002

The dye laser is a FL3002 from Lambda Physics. It consists of one oscillator stage and two amplifier stages (preamplifier and main amplifier). Two cuvettes are necessary, where one is used for the oscillator and preamplifier and one for the main amplifier. Via an electrical tiltable grating wavelengths are selected in the oscillator stage, which are then amplified in the preamplifier. The laser light is aligned by a lens system and then amplified by the main amplifier. For the oscillator and the preamplifier around 20 % (10 % + 10 %) of the pump laser power is consumed. The rest is utilized to pump the main amplifier cuvette. The resulting laser light is frequency doubled by a BBO1 (β-Barium Borate) SHG (Second harmonic generation) crystal. The frequency doubled light with a pulse energy of about 30 - 400μJ is separated from the fundamental laser pulse via a prism frequency separator (four Pellin-Broca prisms) and guided into the vacuum apparatus through a fused silica window with three mirrors (two dichroic mirrors: 220 - 400 nm; one UV enhanced Al-coated mirror: 250 - 450 nm). In the ionization region of the TOF mass spectrometer the laser pulses intersect with the doped helium droplet

Table 3.2: Used laser dyes with the related wavelength ranges λ_{range}, the wavelength with the maximal photon yield λ_{peak}, the wavelength ranges of the second harmonic λ_{range}^{SHG} and the concentrations of the oscillator/preamplifier dye c_{osc}. The concentration of the main amplifier dye is 1/3 of the concentration of the oscillator/pre-amplifier dye.

Laser dye	λ_{range} [nm]	λ_{peak} [nm]	λ_{range}^{SHG} [nm]	c_{osc} [g/l]
Coumarin 47	456.7 - 469.8	456	228.4 - 234.9	1.6
Coumarin 2	456.7 - 469.8	451	228.4 - 234.9	1.3
Coumarin 102	465.8 - 489.8	480	232.9 - 244.9	2.0
Coumarin 307	484.6 - 528.7	500	242.3 - 264.4	3.0
Coumarin 153	524.6 - 539.7	544	262.3 - 269.9	3.8

beam. A fused silica lens focuses the laser to a minimum area of about 1 mm^2. The overall absorption of the mirrors and the lens was measured to be about 15 %. The exact excitation wavelength is determined by measuring the fundamental wavelength of the dye laser pulses with a wavemeter (Coherent Wavemaster).

3.2.3 Laser dyes

To cover a wide spectral range (37060 to 43770 cm^{-1}), five different laser dyes were used (Coumarin 307, 153, 102, 2 and 47). The concentration in the oscillator/pre-amplifier and main-amplifier cuvette were chosen equivalently to the recommendations of Radiant Dyes GmbH. All dyes were solvated in Ethanol ($\geq$ 99.8 %, denatured with about 1 % methyl ethyl ketone) and filled into commercial dye pumps. The reservoir of the oscillator/preamplifier pump contained 0.8 l dye solution whereas the reservoir of the main amplifier pump contained 1.2 l dye solution, due to the higher energy input and therefore faster degeneration. The used mixing ratios with the wavelength ranges for each dye are listed in detail in table 3.2.

3.3 Time of flight mass spectrometer

TOF spectrometry is a reliable, accurate method to probe free clusters and molecules. Here, only a short introduction to the fundamentals of this sophisticated technique is given. Further information can be taken from books like e.g. ref. [84].
TOF spectrometry is based on the measurement of the time of flight of accelerated ions. As the measurement of flight times requires a fixed starting time, only one bunch of ions can be analysed at once. This is periodically repeated, leading to a pulsed procedure. TOF spectra are then typically accumulated for a certain number of laser or electron pulses (sweeps). The working principle is shown in figure 3.3. Ion trajectories are indicated by the dashed blue line.
At first, positively charged ions are created in the ion source region either by electron impact ionization or laser ionization. The ions are extracted by an homogeneous electric

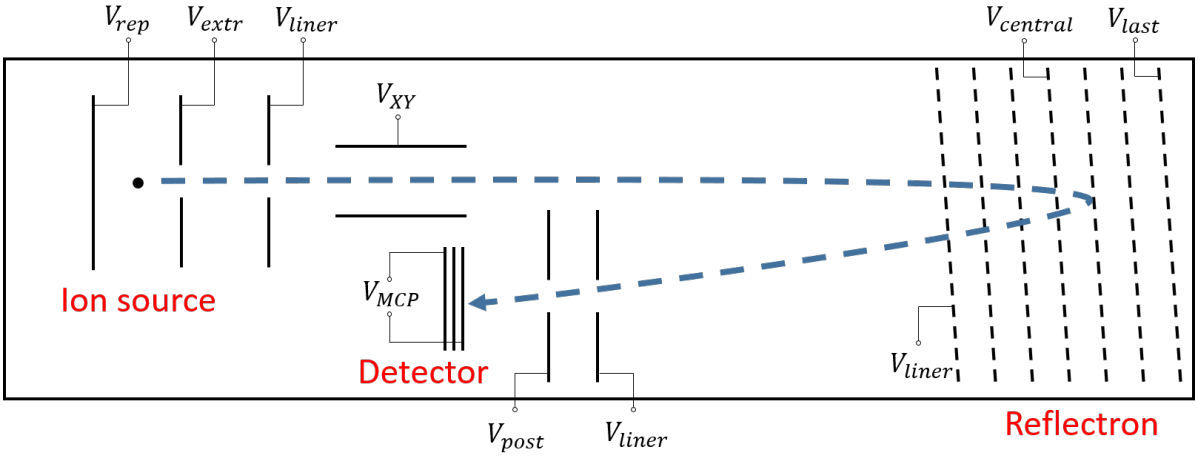

Figure 3.3: Scheme of the time of flight mass spectrometer with indicated voltages:

V_{rep}	Repeller voltage
V_{extr}	Extractor voltage
V_{liner}	Liner voltage
V_{XY}	XY-Deflection voltage
$V_{central}$	Central grid voltage
V_{last}	Last grid voltage
V_{post}	Post acceleration voltage
V_{MCP}	MCP voltage

Note that the MCP voltage is a floating potential.

field which is established between the repeller and extractor plate. Subsequently, the ions are accelerated in another homogeneous electric field between the extractor and the liner. The ion velocities v can be related to the charge q, the mass m and the potential U with which the particles are accelerated:

$$v = \sqrt{2\frac{qU}{m}}. \tag{3.1}$$

An electric field normal to the flight direction of the ions is used to correct the trajectories for optimal detection. In the field free drift region beyond the liner, the ions are separated according to their velocities (charge to mass ratio). Over a distinct drift length D the time of flight t is distributed by:

$$t = D\sqrt{\frac{m}{2qU}}. \tag{3.2}$$

In the reflectron an inhomogeneous electric field is applied to artificially extend the drift length to enhance the mass resolution. To measure the high masses more effectively, the ions are accelerated in a homogeneous field between another liner plate and the post acceleration plate. In the three stage MCP detector, the ions produce electrons that are multiplied many times and finally detected as a current.
As the mass is proportional to the square of the flight times, a model ($\frac{m}{q} = model(t)$) is

Table 3.3: Table with the used voltage settings for the STEFAN KAESDORF RFT50

	U [kV]
Liner	-8.00
Lens	-8.00
Extractor	-3.00
Repeller	3.00
Central grid	-2.10
Last grid	1.38
MCP	3.00

needed to map the times onto masses ($\frac{m}{q}$). In the used TOF spectrometer a quadratic model is used with three constants ($\frac{m}{q} = at^2 + bt + c$). The constants are determined through a calibration with known peaks of the TOF spectrum. Note, that there are also more complicated models that require more constants.
Additional fields are applied, for example in an electric Einzel lens and in the mass filter. The Einzel lens focuses the ions onto the detector. The mass filter is a parallel wire ion gate, consisting of an array of thin metal sheets. When the ions pass through the sheets a weak electric field is turned on between the sheets, deflecting fast ions with small masses.
Note that the ionization process may lead to a fragmentation. If an electric field is present in the extraction region during ionization, one has to consider a lowering of the ionization threshold. For a hydrogen atom with the potential $V(r) = -1/r + Ez$ the energy lowering $\Delta\overline{\nu}$ is given by [57, 75]:

$$\Delta\overline{\nu}[cm^{-1}] = -6.12\sqrt{E[V/cm]}. \tag{3.3}$$

Where E is the electric field inside the extraction zone in [V/cm]. The TOF instrument that was used for the experiments in this work is a STEFAN KAESDORF RFT50. The typical voltages were set according to table 3.3. Other setting that were chosen in the TOF software are listed in the appendix.

3.4 Acquisition of the spectra

A short summary of the experimental setup: Cold, superfluid helium nanodroplets are doped with Au atoms before they are excited, ejected from the droplet, ionized as free atoms and are finally extracted by the TOF spectrometer, where they are counted according to their mass. For each laser shot a huge variety of masses is detected simultaneously, resulting in a full mass spectrum. Measurements at fixed wavelengths are captured to create an excitation spectrum for all the ion masses. The results are data triplets of the form [wavelength, mass, ion yield]. An example of recorded data sets is plotted in figure 3.5. One can see prominent features at the masses of Au (197 amu), AuHe (201 amu), $AuHe_2$ (205 amu) and even $AuHe_3$ (209 amu). The excitation spectra

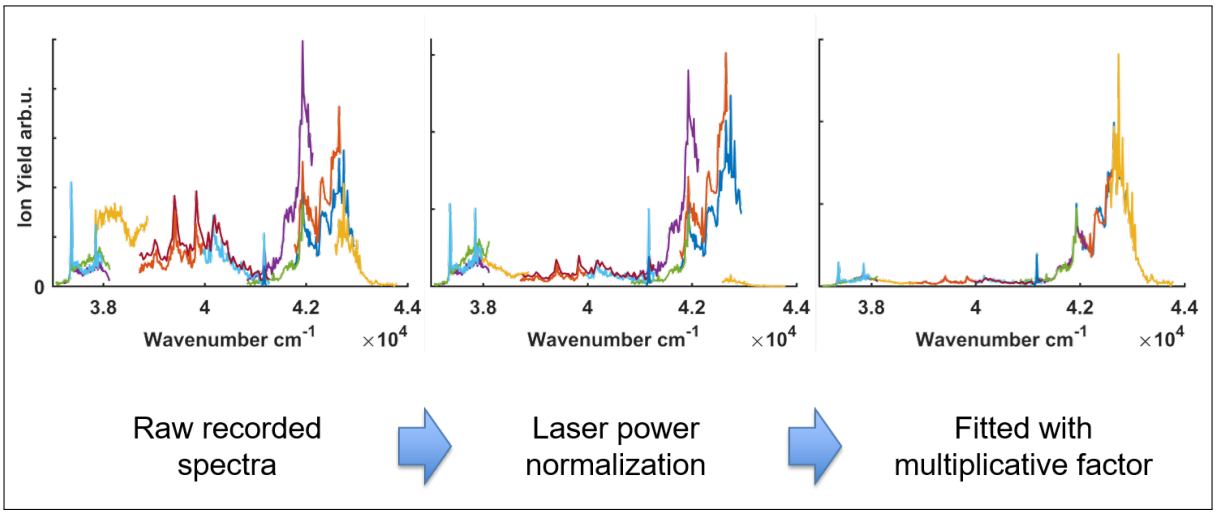

Figure 3.4: The steps of the spectrum acquisition. Left: The raw spectra are displayed. Each colored spectrum corresponds to a measurement with one dye over a particular wavelength range. Middle: Each spectrum (colored line) is normalized with the corresponding power characteristic of the used dye. Right: Each spectrum is multiplied by a constant in a way that the squared differences of overlapping spectra are minimized. This measurement was taken at a nozzle temperature of 15 K for the mass of single Au (197 amu)

of individual masses are presented and discussed at a later point.
The fact that over the entire wavelength range five different laser dyes were used, generates some difficulties. Firstly, the laser efficiency is very different for each laser dye and furthermore, also each dye has its own power characteristic for the corresponding wavelength range. To overlay and compare different excitation spectra from different dyes, the individual spectra were normalized by their individual power curves. In contrast to chapter 2, where it is stated that the transition probability has a quadratic dependence of the laser intensity, the normalization was done with the bare laser intensities, and not with the squared ones. This is justified by the measured linear dependence of the ion yield from the laser power. To further improve the quality of the excitation spectra, multiplicative constants were introduced. Each spectrum (measured with one dye over a destinct wavelength range) is multiplied by a single constant in a way that the squared differences between overlapping spectral parts of different spectra is minimized. For this purpose the fminsearch function of MATLAB [42] was used. The process is depicted in figure 3.4. Due to the fitting, comparability over wide spectral regions is not given, the spectrum is therefore split into two parts.

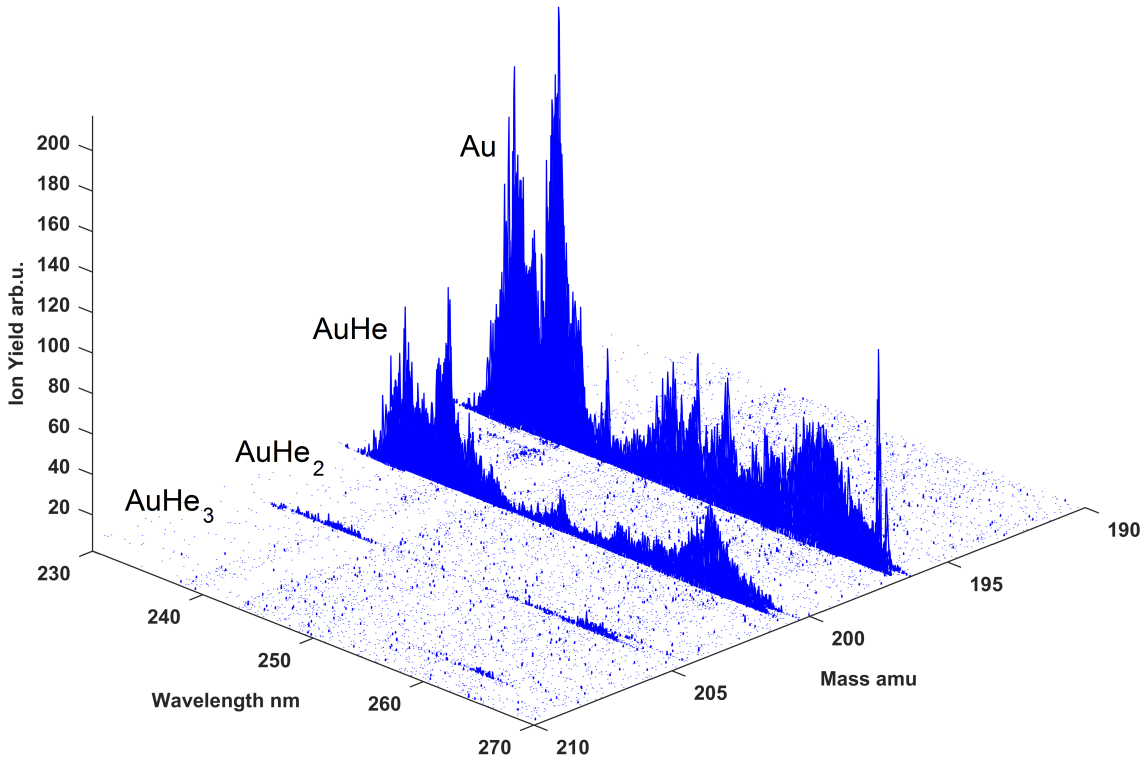

Figure 3.5: Overlayed total acquired data for one droplet size in the mass region around Au (197 amu). The features at the destinct masses 197, 201, 205, 209 correspond to atomic Au, AuHe, $AuHe_2$ and $AuHe_3$. This measurement was taken at a nozzle temperature of 15 K , which corresponds to a mean droplet size of 10 nm.

Chapter 4

Results

This section is based on an unpublished article that is currently in preparation [76]. Large parts of chapter 4 are taken from this manuskript. Before discussing the experimentally recorded excitation spectra the results from the *ab-initio* calculations are presented. The recorded Au $6p\,^2P_{1/2} \leftarrow 6s\,^2S_{1/2}$ and $6p\,^2P_{3/2} \leftarrow 6s\,^2S_{1/2}$ transitions, i.e. the in-droplet D1 and D2 transition, will be presented and discussed separately in the following sections.

4.1 Theoretical results

As mentioned above all the calculations were performed by Johann Pototschnig. This also applies to the evaluation and interpretation of the numerical results.

4.1.1 Diatomic AuHe pair potentials

Table 4.1 lists the parameters extracted from the diatomic AuHe potential energy curves that were calculated as described in chapter 2. In contrast to previous computations [15] of excited states, in which a basis set of triple zeta quality was used, here a quintuple zeta basis set was employed. Furthermore, a state-averaged multiconfigurational method was selected in order to describe all states simultaneously, which results in a more balanced description for the included states. In order to estimate the deviation of the MCSCF approach from the previously used methods [15] a coupled cluster (CC) calculation was performed for the ground state with the same basis set as used in the MCSCF calculation. A dissociation energy of 13.9 cm^{-1} and an equilibrium distance of 4.12 Å were obtained after correcting for the basis set superposition error. This is in good agreement with the values from ref. [15] (cf. table 4.1). The largest deviation from the previous results is observed for the $2^2\Pi$ state, indicating that there is still a large uncertainty for this state.
The computations were performed for larger internuclear separations, which made it even possible to determine the equilibrium distance and dissociation energy of the $3^2\Sigma^+$ state. Spin-orbit coupling was included using spin-dependent effective core potentials [24]. The corresponding computed potential energy curves are shown in figure 4.1 and the corresponding parameters obtained by fitting these potentials are listed in table 4.2.

Table 4.1: List of the results obtained for the dissociation energy D_e, equilibrium distance r_e and Ancilotto parameter λ_A of the spin-averaged potential energy curves. The values reported in previous works [14, 15] are shown for comparison. The $2^2\Pi$ potential has a vibrational constant $\omega_e = 117.4$ and an asymmetry parameter $\omega_e x = 10.7$.

	CI [15]		CCSD [14, 15]		this work		
State	D_e [cm^{-1}]	r_e [Å]	D_e [cm^{-1}]	r_e [Å]	D_e [cm^{-1}]	r_e [Å]	λ_A
$X^2\Sigma^+$			15.3	4.09	11.9	4.20	5.5
$2^2\Sigma^+$	11.6	4.32			12.9	4.30	6.1
$1^2\Pi$	11.3	4.33	13.1	4.33	13.4	4.29	6.3
$1^2\Delta$	11.8	4.30	13.5	4.19	16.6	4.20	7.6
$3^2\Sigma^+$					0.6	7.44	0.5
$2^2\Pi$	136.6	2.38			320.9	2.61	91.8
$1^4\Sigma^+$					1.5	5.97	1.0
$1^4\Pi$					2.0	5.61	1.2

Table 4.2: Results obtained for the potential energy curves including spin-orbit interaction. The dissociation energy D_e, equilibrium distance r_e and the Ancilotto parameter λ_A are tabulated. The $2^2\Pi_{3/2}$ potential has a vibrational constant $\omega_e = 115.2$ and an asymmetry parameter $\omega_e x = 10.6$.

State	D_e [cm^{-1}]	r_e [Å]	λ_A
$X^2\Sigma^+_{1/2}$	11.9	4.20	5.5
$2^2\Sigma^+_{1/2}$	14.2	4.27	6.6
$1^2\Pi_{3/2}$	14.1	4.28	6.6
$1^2\Delta_{5/2}$	15.0	4.23	7.0
$1^2\Pi_{1/2}$	14.3	4.27	6.7
$1^2\Delta_{3/2}$	15.3	4.22	7.1
$2^2\Pi_{1/2}$	0.9	6.52	0.6
$3^2\Sigma^+_{1/2}$	0.6	7.26	0.5
$2^2\Pi_{3/2}$	312.8	2.63	90.2

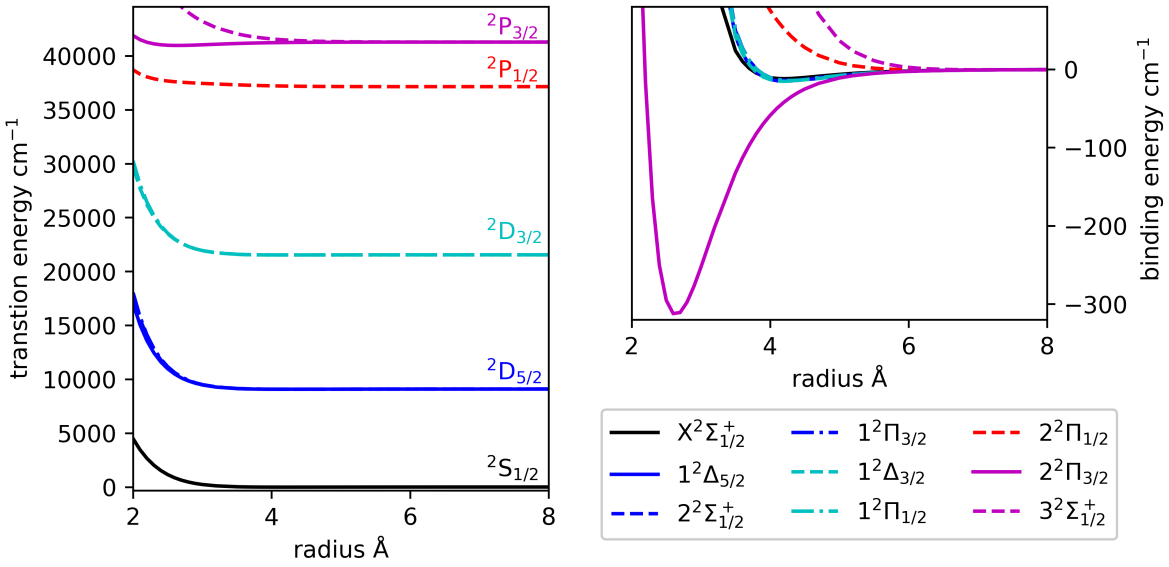

Figure 4.1: Calculated potential energy curves for different electronically excited states of the diatomic AuHe molecule (left). In the right figure the asymptotes have been set to zero allowing for a better comparison of the different states. Note that the differences between the $1^2\Delta_{5/2}$, $1^2\Pi_{3/2}$ and $2^2\Sigma^+_{1/2}$ states are negligible and their potentials overlap in the figure. Similarly, the states $1^2\Delta_{3/2}$ and $1^2\Pi_{1/2}$ are not separable.

4.1.2 Location of the Au inside the He$_N$

A priori, it is not known if a ground state or excited state Au atom prefers a location at the surface or inside the droplet. The Ancilotto parameter λ_A [4, 91] can serve as a first estimation for the location of a dopant. The calculation of this dimensionless parameter is based on the ratio of the energy gain due to dopant-matrix interaction (dopant-He potential depth) and the energy cost for the formation of a bubble inside the droplet in which the atom is accommodated. The parameter can be calculated from the AuHe diatomic pair potentials and is thus listed in table 4.1 and 4.2 together with the spectroscopic constants. The Ancilotto parameter predicts a solvation of the dopant for $\lambda_A > 1.9$ and a surface location for $\lambda_A < 1.9$ [4]. Consequently, among the calculated states the $2^2\Pi_{1/2}$ and $3^2\Sigma^+_{1/2}$ arising from the 6p ^{2}P$_{1/2}$ and 6p ^{2}P$_{3/2}$ asymptotes are expected to prefer a location at the surface of the droplet, while all other states are expected to be solvated inside droplet.
However, a more elaborate answer to the question about the location of the Au atom beyond the Ancilotto parameter approach can be given based on a calculation of the solvation energy of the atom as a function of its position with respect to the droplet center. As described above, the potential energy curves were mapped onto angular dependent potentials (according to equations 2.6 - 2.13). In the helium DFT calculation the helium density (10^4 He atoms) was optimized for each of the resulting potentials of

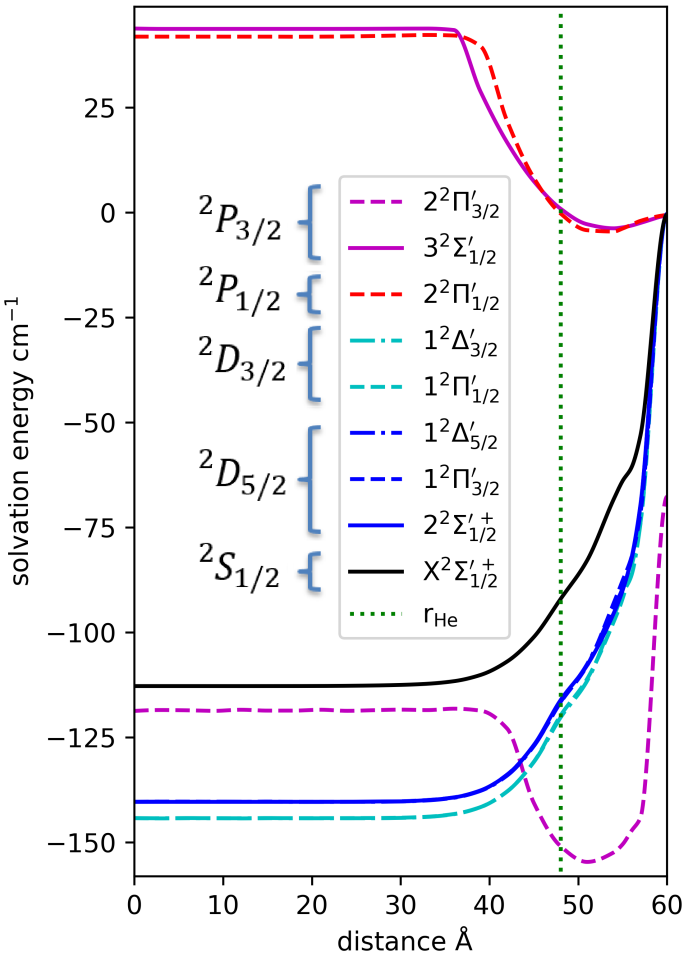

Figure 4.2: Solvation energy of a gold atom inside a helium droplet for the different calculated states, including spin-orbit interaction, as a function of the distance between the droplet center and the atom. The corresponding asymptotes are listed for easier allocation. The dotted green line marks the radius of the helium droplet used for the calculation. The optimized He densities were determined using the Orsay-Trento functional [17]. Similar to figure 4.1, the solvation energies related to the states arising from the $^2D_{3/2}$ and $^2D_{5/2}$ asymptotes overlap and cannot be seen individually.

the individual states. Subtracting the energy of the helium density with the Au atom inside the droplet from the energy of the helium density of the plain droplet gives the solvation energy, calculated as a function of the distance of the dopant from the droplet center. For the ground state, the result can be compared to a previous calculation by our group that reported a solvation energy of 175.5 cm^{-1} [35], which is a higher value than the one obtained in the present work owing to the different employed AuHe pair potentials: While ref. [35] used the ground state pair potential from ref. [14], in the present work the potentials were calculated from scratch with slightly different results,

see table 4.1.
The calculated solvation energies for the ground and different excited states are presented in figure 4.2. It can be seen that the states corresponding to the $^2S_{1/2}$ and $^2D_{3/2,5/2}$ asymptotes have a solvation energy minimum inside the superfluid helium, indicating that the gold atom is located inside the droplet in these cases. For the states corresponding to the $^2P_{1/2,3/2}$ asymptotes a global minimum at the surface is observed for all states, however, inside the droplet two different behaviors are observed: The $2^2\Pi'_{1/2}$ ($^2P_{1/2}$) and $3^2\Sigma'^+_{1/2}$ ($^2P_{3/2}$) state show a repulsive potential and will be ejected with only a small probability to be captured at the surface. The $2^2\Pi'_{3/2}$ ($^2P_{3/2}$) state prefers a solvation inside the droplet with a higher probability to be found close to the surface.

4.1.3 Calculated excitation spectra

In the experiment, the gold atom can be assumed to be in its ground state, located inside the droplet. It is surrounded by helium, the interaction between helium and the Au dopant atom depends on the electronic state. This alters the transition energy and, in the following, we present a calculation of the in-droplet D1 and D2 transitions for droplets consisting of $N = 10^4$ He atoms. Oscillations of the helium density around the dopant influence the resulting energy shift and, in particular, cause an additional line broadening. In our theoretical treatment the breathing mode and the quadrupole mode of the bubble around the dopant have been considered. The resulting spectra are shown together with the experimental spectra. Note that in this treatment the transitions from the ground state to the $2^2\Pi'_{3/2}$ and $3^2\Sigma'^+_{1/2}$ states arising from the $^2P_{3/2}$ asymptote exhibit splitting, because the spherical symmetry is not conserved due to the inclusion of the quadrupole mode. This can be compared to the in-droplet D2 line in Ag [68] or the Ba^+ ion [115].

4.2 Experimental results

In this section the results of probing the electronic structure of Au atoms inside helium nanodroplets obtained with the experimental setup shown in figure 3.2 are presented and interpreted. As explained before, the excitation spectrum reaching from 37060 cm^{-1} to 43770 cm^{-1} is split into two parts which are discussed separately. One containing the in-droplet D1 line (37060 - 41000) cm^{-1} and one containing the in-droplet D2 line (41000 - 43770) cm^{-1}.

4.2.1 In-droplet D1 line (37060 - 41000) cm^{-1}

4.2.1.1 $AuHe_N$ excitation spectrum: D1 transition

The recorded excitation spectrum from 37060 to 41000 cm^{-1} is shown in figure 4.3 for helium droplets He_N, consisting on average of $N = 1.25$ x 10^4 He atoms. This part of

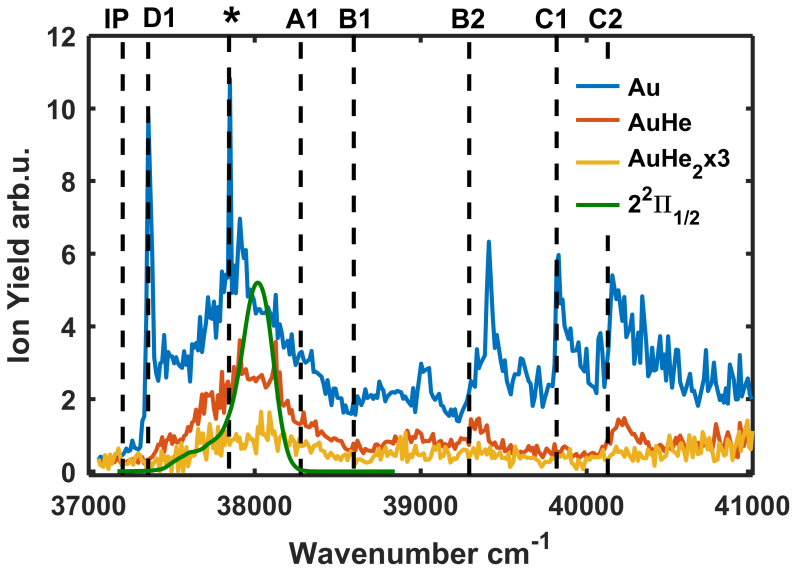

Figure 4.3: Excitation spectrum of gold atoms inside helium nanodroplets He_N (N = 1.25 x 10^4) in the region from 37060 to 41000 cm^{-1}. The ion yields for Au (blue), AuHe (red) and $AuHe_2$ (yellow) are shown as a function of the excitation laser wavelength. Vertical dashed lines mark the position of bare atom transitions as listed in table 4.3. A variety of features can be identified to the blue of the atomic $6p\,^2P_{1/2} \leftarrow 6s\,^2S_{1/2}$ transition, marked as D1 line. The broad adjacent structure peaking at 37970 cm^{-1} is assigned to the broadened and blue-shifted in-droplet D1 transition of Au atoms. The asterisk marks the $5d^9_{5/2}6s_{1/2}6p_{3/2}\,^2P_{3/2} \leftarrow 5d^96s^2\,^2D_{5/2}$ transition. The features exhibiting a rising edge at the bare atom transitions B2, C1 and C2 originate from Au atoms relaxed into the $5d^96s^2\,^2D_{3/2}$ state. The field-free threshold for two-photon ionization corresponds to the vertical dashed line at 37206 cm^{-1} marked with IP. The green line represents the calculated spectrum.

the recorded spectrum contains the $AuHe_N$ $6p\,^2P_{1/2} \leftarrow 6s\,^2S_{1/2}$ transition (in-droplet D1 line). The figure shows the ion yield obtained for mass windows corresponding to Au (blue), AuHe (red) and $AuHe_2$ (yellow) as a function of the excitation laser wavelength. In the graphic, possible bare atomic Au transitions are marked with vertical dashed black lines. The involved states can be read out of table 4.3 and figure 4.4 according to the abbreviations on top of figure 4.3. The free atom D1 line at 37359 cm^{-1} is indicated by the vertical dashed line marked by D1 on top. A broad Gaussian-like structure peaking at (37970 $\pm$ 15) cm^{-1} with a full width at half maximum (FWHM) of (645 $\pm$ 30) cm^{-1}, as obtained from a Gauss function fitted to the AuHe trace (2σ significance level), is located adjacent to the free atom D1 line. On top of the broad structure a sharp line can be located coinciding with the transition marked with an asterisk. Beyond that, beginning at about 39500 cm^{-1} at least three features with a sharp rising edge and a

wing extending to the blue can be identified. The calculated in-droplet D1 transition from the $X^2\Sigma'^+_{1/2}$ ground state into the $2^2\Pi'_{1/2}$ state is plotted as a solid green line in figure 4.3 (scaled to the Au signal).

4.2.1.2 In-droplet D1 line

Based on the comparison of the experimentally acquired spectrum with the calculated spectrum we assign the broad structure between 37300 and 38500 cm^{-1} to the broadened and blue-shifted D1 transition of Au atoms inside helium nanodroplets. The calculation underestimates the width of the transition, indicating that maybe bubble oscillation modes of higher order, which were not included in the calculation, contribute to the broadening of the line. The shift, however, is well reproduced by the calculation. The observed strong blue-shift and broadening is very typical for valence electron transitions in atoms located inside of helium droplets, supporting the result from the theory section that predicts a location inside the droplet for ground state Au atoms. Close inspection of the in-droplet D1 line reveals the presence of a very weak additional shoulder-like structure beginning at the atomic transition marked with A1.

4.2.1.3 Atomic lines: D1 and *

There are two lines in the spectrum exhibiting atomic characteristics, namely the lines marked with D1 (37359 cm^{-1}) and the other marked with an asterisk (37846 cm^{-1}). Both features can be readily assigned to the bare atom transitions ($6p\,^2P_{1/2} \leftarrow 6s\,^2S_{1/2}$ and $5d^9_{5/2}6s_{1/2}6p_{3/2}\,^2P_{3/2} \leftarrow 5d^96s^2\,^2D_{5/2}$) based on comparison to the NIST data base [54]. Due to the pickup geometry it could be possible that bare atoms effuse from the pickup cell to the ionization zone of the TOF spectrometer. But both bare atom lines decreased significantly in intensity when the helium beam was blocked, indicating that atoms transported by the helium droplets are the source of their origin and not bare atoms effusing from the pickup cell. The atomic D1 line as well as the asterisk line can thus be pinned to transitions of atoms that were ejected from the helium droplet through a relaxation/ejection mechanism. For a successful detection in the TOF spectrometer it would therefore take at least three photons (in-droplet excitation - relaxation/ejection - bare excitation - bare ionization). Note that this would be the easiest scenario, and as the main channel for the ejection cannot be found with the used experimental setup, the real excitation and relaxation paths could be much more complex.

4.2.1.4 B2, C1, C2 transitions

Further distinct peaks are found beyond the in-droplet D1 transition in the regime from 38500 to 40500 cm^{-1}. In this region no possible transitions are located that can be reached from the ground state. It can be seen that all features in this region do not exhibit a characteristic sharp atomic line, but instead comprise of a sharp rising edge,

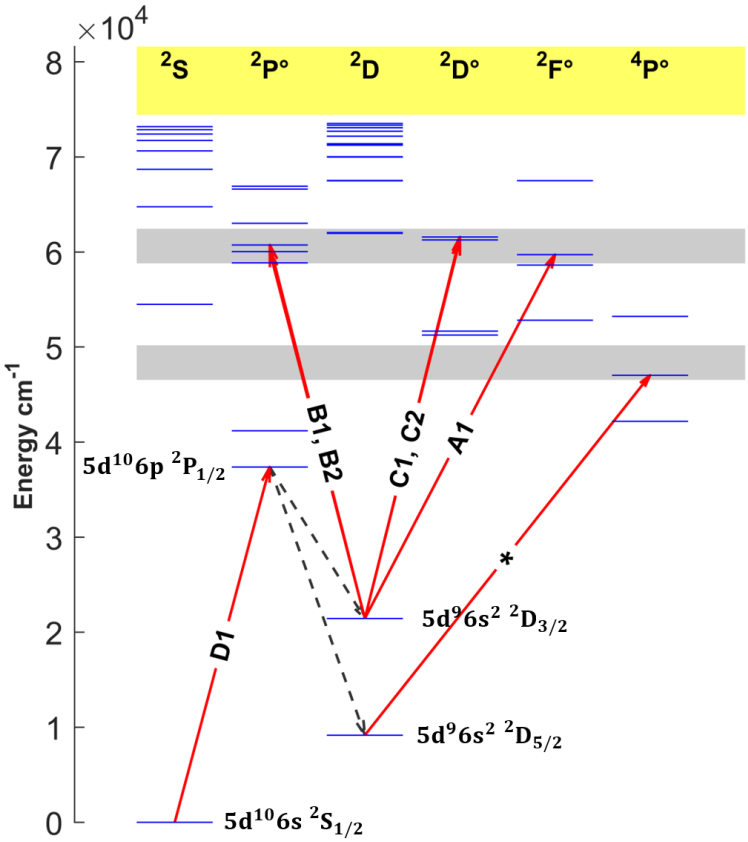

Figure 4.4: Grotrian diagram of Au. The states (blue horizontal lines) are sorted corresponding to their total orbital angular momentum L, their total spin S and their parity (° for odd, no superscript for even) i.e. ${}^{2S+1}L^{\circ}$. Transitions identified in the spectrum following the D1 excitation are drawn as arrows (red - excitation, black - possible relaxation pathway). The gray shaded areas mark the spectral interval from 37060 to 41000 cm^{-1} (cf. figure 4.3) from the view point of the $5d^96s^2\,{}^2D_{3/2}$ and $5d^96s^2\,{}^2D_{5/2}$ states.

followed by a broad wing extending towards the blue. The coincidence of the rising edge of the structures with the marked position of bare atom transitions is striking and we conclude that the observed features are caused by these exact transitions. All intermediate states correlate to atoms in the ${}^2D_{3/2}$ state, as it can be seen in table 4.3.
As the Au atoms are supposed to be in their ground state due to the interaction with the cold helium environment, some excitation/relaxation dynamics can be hold responsible for their presence. Note that the C1 and C2 transitions exhibit a similar spectral form, which may be expected as the intermediate states correlate to the two spin orbit components of the $5d^9_{3/2}6s_{1/2}6p_{3/2}\,{}^2D_{3/2,5/2}$ states, involving an excitation of one of the $6s^2$ electrons. However, the transitions labeled B1 and B2 appear very different in the

spectrum: While B1 is strongly broadened and barely visible, B2 is very similar to the C1 and C2 transition. Note that these two transitions differ only in the alignment of the spin of the valence electron occupying the 7p orbital, i.e. the total angular momentum. However, as our calculation for the lowest ^{2}P state suggests, the interaction between the helium atoms and the Au atom can differ dramatically for different spin-orbit substates. Furthermore, the weak feature in the Au ion yield trace located at 39000 cm^{-1} (cf. figure 4.3) does not coincide with any known transition in the Au atom and eludes from an assignment.

The corresponding transitions are shown in the Grotrian diagram in figure 4.4. The grey shaded areas mark the energy interval that can be reached by a one-photon excitation originating from the lowest two $5d^96s^2\,^2D_J$ states within the range from 37060 to 41000 cm^{-1}. Starting from the $5d^96s^2\,^2D_{3/2}$ and $5d^96s^2\,^2D_{5/2}$ states, arrows indicate possible transitions [87], which are listed in table 4.3. Black arrows in figure 4.4 indicate possible relaxation pathways, however, as will be discussed further down, we note that the ^2D_J states are not necessarily populated upon direct relaxation from in-droplet D1 transition.

The peak form and shift of the B2, C1 and C2 transitions imply that the interaction of the corresponding excited states with the surrounding helium is weaker than in the case of the in-droplet D1 transition. This might be expected for transition involving core-level electrons (5d electrons) shielded by the outer s electrons [21], however, all transitions listed in table 4.3 correspond to an excitation of one of the $6s^2$ valence electrons. The B2 transition, in particular, corresponds to an excitation into a state with $5d^{10}7p\ ^2P_{3/2}$ configuration. A migration of the atom to the surface of the helium droplet would explain the observation of narrower lines with sharp rising edges, due to the weaker helium interaction. However, according to the calculations presented above in figure 4.2, the $5d^96s^2\,^2D_{3/2}$ state is strongly bound inside the droplet and is thus not expected to migrate to a surface position. Similar peak forms have, for example, been observed for $CrHe_N$, where the corresponding transitions have been attributed to transitions from weakly bound states into weakly repulsive states in ejected $CrHe_n$ ($n > 0$) complexes [53]. The corresponding spectra were mainly detected for the Cr mass window and, for some transitions, also for the CrHe mass channel. Larger $CrHe_n$ ($n > 1$) complexes were absent due to the excess energy provided by the ionizing photon to the system. Considering the similarities between the $CrHe_N$ spectra and the features observed for $AuHe_N$, such a scenario seems favourable as an explanation for the observed superimposing spectral features. The AuHe potential energy curves that arise from the metastable ^{2}D state asymptotes are indeed very weakly bound, however, calculations for the intermediate AuHe states are not available but may exhibit a weakly repulsive character in the respective Franck-Condon window.

Table 4.3: List of transitions that can be pinned to features in the excitation spectrum plotted in figure 4.3. The transitions are drawn as vertical dashed lines in figure 4.3, annotated with the abbreviations as listed below. Transition energies $\Delta\overline{\nu}$ are taken from ref. [54] and rounded to the last digit.

Initial state		Intermediate state		Abbreviation	$\Delta\overline{\nu}$ [cm^{-1}]
$5d^{10}6s$	$^2S_{1/2}$	$5d^{10}6p$	$^2P_{1/2}$	D1	37359
$5d^96s^2$	$^2D_{5/2}$	$5d^9_{5/2}6s_{1/2}6p_{3/2}$	$^4P_{3/2}$	*	37846
$5d^96s^2$	$^2D_{3/2}$	$5d^9_{3/2}6s_{1/2}6p_{3/2}$	$^2F_{5/2}$	A1	38278
$5d^96s^2$	$^2D_{3/2}$	$5d^{10}7p$	$^2P_{1/2}$	B1	38598
$5d^96s^2$	$^2D_{3/2}$	$5d^{10}7p$	$^2P_{3/2}$	B2	39293
$5d^96s^2$	$^2D_{3/2}$	$5d^9_{3/2}6s_{1/2}6p_{3/2}$	$^2D_{5/2}$	C1	39820
$5d^96s^2$	$^2D_{3/2}$	$5d^9_{3/2}6s_{1/2}6p_{3/2}$	$^2D_{3/2}$	C2	40128

4.2.2 On the origin of AuHe$_n$ species

An important question to be addressed is about the origin of exciplexes constituting of ^{2}D state Au atoms with attached He atoms in the spectral region beyond the in-droplet D1 transition. It is interesting that these features are observed at all in this regime because, as noted above, there are no excited states in between the D1 and D2 line that can be reached from the ground state. In order to discuss their possible origin, some possibilities need to be excluded before proposing a scenario that is capable of explaining the observed spectral features:

1. Firstly, one has to reflect if there is already a significant amount of excited $^2D_{3/2}$ and $^2D_{5/2}$ state Au atoms present in the helium droplets before reaching the ionization zone. This seems feasible due to the high temperatures of the pickup cell. For example in atom beam experiments Au atoms in the $^2D_{5/2}$ state have been observed at comparable oven temperatures [117]. Considering the lifetime on the order of a few ms [80], a helium droplet aided transport from the pickup chamber to the extraction zone in the TOF instrument does not seem impossible (and has been shown for laser ablated metastable Al attached to He$_N$ [45]). But if such a scenario would be true, the difference in the population of the two $^2D_{3/2}$ and $^2D_{5/2}$ states would be dramatic due to the underlying thermal distribution and, as a consequence, the transition marked by the asterisk should be much stronger in the spectrum. A more striking argument is the fact that the calculations above suggest that the ^{2}D states prefer a location inside the droplet and not at the surface, which would make transported atoms in the ^{2}D states irrelevant as the transitions recorded clearly suggest a weak interaction with the helium surrounding, and therefore a excitation/relaxation/ejection has to take place to even measure exciplex features. Corresponding transitions originating from atoms inside the helium droplet would be expected to be broader and exhibit a larger blue-shift and are not visible in the spectra. The broad feature following the B1 atomic line could

make an exception, but as explained above this feature arount 39000 cm^{-1} cannot be pinned to a definite source for certain. Considering these arguments, it seems unlikely that thermally excited atoms doped to the droplets in the pickup zone contribute significantly to the recorded spectra.

2. Following ref. [48], the dissociation of dimers or larger oligomers and the subsequent surface migration of an atom may also explain the observed transitions. In the case of $AuHe_N$, a similar scenario based on a dissociation and subsequent ejection of ^{2}D state atoms with one or more attached He atoms would provide a hypothesis in agreement with the theoretical and experimental results. As a considerable amount of dimers and a small amount of trimers is also present in a fraction of the droplets, such species may indeed contribute to the spectra. Unfortunately, gas phase data for gold dimers and larger oligomers are not available for the respective spectral regime [41, 81]. However, possible transitions of Au dimers and trimers have been studied, for example, in argon matrices [23], where absorption bands were found near the D2 line. To investigate if a dissociative process could be the source for the detected Au and AuHe ions in the corresponding energy region, additional experiments have been performed in which the excitation wavelength was fixed at 39825 cm^{-1} (C1 peak) while the gold oven temperature was increased. Note that the temperature is estimated based on the temperature dependent resistance of the heated oven. This method ensures good reproducibility, but absolute temperature values calculated from the individual resistances may contain significant systematic errors. According to the Poissonian pickup-statistics the increased oven temperature leads to an increase in the doping level from single atoms to dimers and trimers. The result is shown in the top panel of figure 4.5. Note that only the Au and Au_2 traces are shown and that these traces have been normalized. The total yield of Au_2 is about 20 times lower than the Au yield. The Au_3 trace is not shown but behaves similar to the Au_2 yield, though exhibiting an even lower total ion yield. The recorded data points have been fitted with a Gaussian function to guide the eye. The Au oven temperature dependence at the in-droplet D1 line (38020 cm^{-1}) has been recorded as a reference, (cf. bottom panel of figure 4.5). Both transitions show the same Au oven temperature dependence, in particular, there is a clear distinction between the Au and Au_2 yield with the monomer trace starting to rise at lower temperatures than the dimer trace for both transitions. From this study, two important conclusions can be drawn: (i) there is a dimer and trimer background that increases with pickup temperature, which, in the respective spectral region, is likely due to non-resonant two-photon ionization. (ii) However, for both selected photon energies there are clearly distinct monomer signals present and both exhibit a similar temperature dependence. Finding (ii) indicates that monomer doped helium droplets are the source for the in-droplet D1 line as well as for the features that are observed beyond it. Consequently, it is concluded that the dissociation of dimers or larger oligomers into ^{2}D state $AuHe_n$ fragments is not supported by our results.

A hint for a possible explanation of the origin of metastable ^{2}D atoms is given by matrix

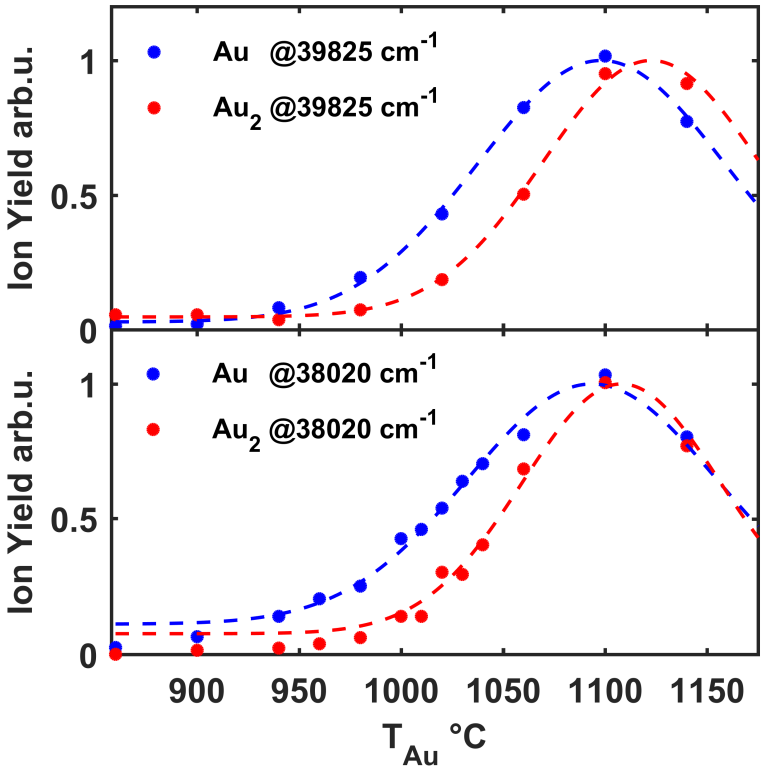

Figure 4.5: Ion yields obtained for Au and Au_2 as a function of the approximate Au oven temperature at two selected photon energies (top panel: C1 transition - 39825 cm^{-1}; bottom panel: in-droplet D1 line - 38020 cm^{-1}). The mean number of helium atoms of the employed helium droplets He_N corresponds to N = 1.25 x 10^4. The ion yields have been normalized with respect to the maximum of the corresponding Gaussian fit functions. For both transitions it can be seen that the monomer yield starts to rise at a lower temperature than the dimer yield.

isolation experiments in liquid and solid helium [78, 79, 80]. In these works, excited Au atoms have been prepared by a laser which is not resonant with a Au transition in the matrix, similar to the situation here. Two possible mechanisms have been proposed in order to explain the origin of the excited state atoms:

1. It was argued that these states are populated either by near-resonant transitions, where a photon is absorbed whose energy is only slightly detuned from a transition that is strongly broadened by the surrounding matrix. A near resonant excitation and subsequent relaxation into the ^{2}D state may indeed be possible, considering the relatively high photon intensity and the fact that the features are located in between the two strongly broadened in-droplet D lines of the Au atom. The near linear background in between 38500 and 41000 cm^{-1} supports this scenario.

2. Another possible scenario is the population of the ^{2}D state through a multiphoton ionization (in our case two-photon ionization) and subsequent electron-ion recombination. But upon ionization, ions tend to agglomerate He atoms around them, known as snowball formation [100], and a recombination of the ion core and electron may be hindered by this effect. On the other hand, for alkali atoms in high Rydberg states on the surface of helium droplets, which represent a similar system, recombination/relaxation of the valence electron with the ion core is thought to be the main decay mechanism that limits the life time of these states [69, 88]. Furthermore, such a recombination process of electrons and ions has been exploited in matrix isolation works, in order to prepare excited atoms from which fluorescence light can be detected [96]. As the employed photon energies are only slightly above the ionization threshold, the free electron can only have a small amount of excess energy. Considering that the electron has to pass through a barrier [19, 85] on its way from ionization inside the droplet through the surface into vacuum, it seems possible that both species find each other and recombine. The resulting energy release maybe sufficient for the resulting neutral atom to leave the droplet as bare atom or exciplex. As two photon ionization is a non-linear effect, the yield should have a quadratic laser power dependence. In the current spectra this behaviour could neither be proved nor excluded. Here, photoelectron spectroscopy [68, 74] could reveal insight into the energetic situation. Even though the electron has to pass through a layer of helium upon ionization, it has to be considered that energy is released in this ionization process, due to the stronger interaction between the surrounding helium and the ion, which manifests in a lowering of the ionization potential.

In both cases a combination of radiative and non-radiative processes will lead to a population of the lowest ^{2}D state manifold. However, based on our current data, we cannot distinguish between the two scenarios, which may both compete for the formation of ^{2}D state atoms. In any case, the fact that the ion yield in both the Au and AuHe trace do not reach a zero-background level beyond the in-droplet D1 transition (in particular, beyond about 38500 cm^{-1}) indicates that a fraction of the atoms in the helium droplet is non-resonantly ionized, supporting both of the above scenarios. In conclusion, we attribute the observed transitions (B2 - C2) to ^{2}D state atoms that are produced in a non-resonant process, either by direct near-resonant excitation or non-resonant ionization followed by recombination. Subsequently, radiative or fast non-radiative relaxation dynamics lead to the population of the metastable ^{2}D state manifold. In the course of the relaxation process, the excited atom is ejected as an AuHe$_n$ exciplex consisting of a ^{2}D state Au atom with several attached He atom.

4.2.3 Droplet size dependence - D1 line

Further support for the assignment of spectral features and insight into the photoinduced dynamics is obtained from the droplet size dependence of the recorded excitation spectra. Figure 4.6 shows the excitation spectra for three different nozzle temperatures

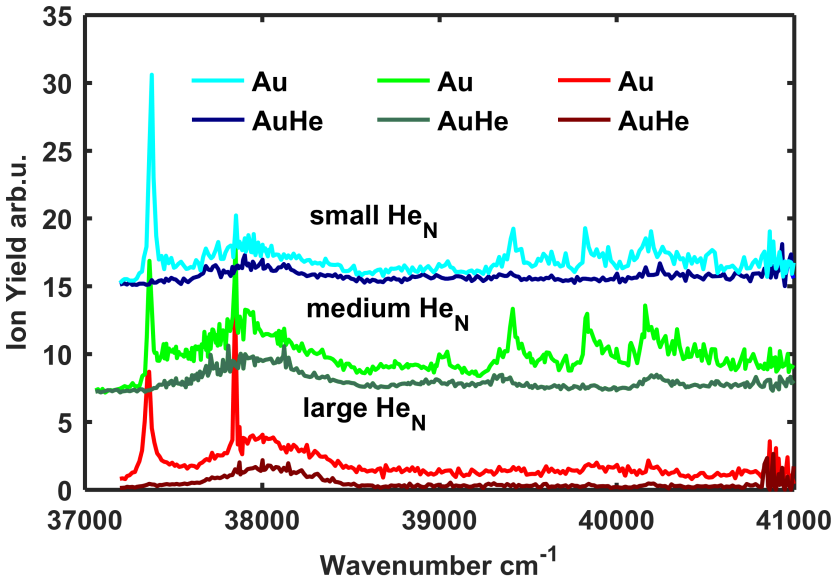

Figure 4.6: Excitation spectrum of gold atoms embedded in helium nanodroplets He_N in the regime from 37060 cm^{-1} to 41000 cm^{-1} for large N = 2 x 10^6 (red), medium N = 1.25 x 10^4 (green) and small N = 9 x 10^3 (blue) droplets. The ion yield for Au (bright) and AuHe (dark) are displayed in each case.

(12, 15 and 17 K), corresponding to mean droplet sizes He_N with N = 2 x 10^6 (red), N = 1.25 x 10^4 (green) and N = 9 x 10^3 (blue). Shown are both the ion yields for the Au (bright spectra) and AuHe (dark spectra) mass windows as a function of the excitation laser wavelength. The spectra for the small and the middle sized droplets look very similar. Due to the optimization of the pickup condition to the middle sized droplets, spectra recorded for these droplets exhibit more total yield.
Whereas for very large helium droplets (red spectra), the spectra indeed look different. The peaks beyond 38500 cm^{-1} disappear , compared to the background. The spectra of these large droplets seem to resemble the results reported for experiments on Au atoms in bulk matrices [31, 33, 64, 73], where no transitions in between the in-droplet D1 and D2 line have been found. The droplets appear to possess a more bulk-like characteristic, which makes the B2, C1 and C2 transitions to exclusive features of the helium droplet isolation spectroscopy method.
The disappearing of the transitions in the spectrum for large droplets indicates that (i) the excited Au atoms either stay inside the droplet or (ii) the required intermediate system does not form. As discussed above, the source of these transitions has been attributed to monomer doped helium droplets. And as the monomer in-droplet D1 line is still observed in the large droplets the origin of the features beyond 38500 cm^{-1}, namely single isolated Au atoms, should still be present and intermediate states are expected to form.
This also indicates that both contributions (in-droplet D1 vs. B2, C1, C2) behave differently for different droplet size regimes, calling for further discussions. The second

scenario, namely a suppressed ejection could be explained by the big size of the droplets. In the calculations it turned out that the ^2D_J state atoms prefer a location inside the helium droplet. Therefore, upon relaxation to the $^2D_{3/2}$ state, if the helium density relaxes and all excess energy is dissipated by the helium surrounding, the excited Au atom is likely to stay inside the droplet and may not get ejected. Another possibility is offered by the enhanced relaxation dynamics inside the liquid helium droplet. In bigger clusters where the excited atom takes more time to be ejected from the droplet, the atom may relax before it exits the droplet. Examination and potential verification of such scenarios need to be set as objectives for successive studies. If the ionization step takes place inside the helium droplet, the Au ions are expected to stay solvated inside the droplet due to the strong binding character of the potential for an ion inside a helium droplet [65].

Assuming the ion-electron recombination scenario described above, the possibility of electrons bound within or at the surface of a helium droplet has to be considered as well. In experimental studies it was found that only droplets larger than $N = 7.5 \text{ x } 10^4$ can carry an excess electron in a stable manner [20, 36]. For neutral droplets, such as in our experiment, with a solvated ion + electron, the system is expected to be more stable and thus even smaller droplets should support surface bound electron states. This assumption is encouraged by the calculations of Golov *et. al* [26]. Therein, for overall neutral helium droplets, stable Rydberg states have been predicted, where the excited electron is bound outside the helium droplet due to the attractive Coulomb interaction with the positively charged droplet. These states are predicted to be supported by droplets beyond a size of $N = 7 \text{ x } 10^2$. Consequently, the recombination process might be quenched at large droplets due to the formation of spatially separated electrons and cations, which would explain the observed disappearance of the features.

It can be seen that the transition marked by an asterisk behaves differently than the other superimposed features. The line represents a fingerprint of bare atoms in the $^2D_{5/2}$ state, and it is concluded that these atoms are ejected directly upon resonant excitation of the in-droplet D1 transition. Furthermore, this observation indicates that the nature of the mechanism underlying the formation of the ^2D state is different from the resonant excitation process that leads to the observation of the asterisk transition.

Another alternative but, at this point, rather speculative point that may be raised in this context is that for the largest employed cluster sizes, quantized vortices may already be present [28]. For droplet sizes down to a few 100 nm diameter vortices have been observed experimentally [28]. Potentially, the presence of vortices will affect the ejection and formation dynamics of $AuHe_n$ exciplexes, which may also contribute to the quenching of the observed transitions.

In any case, we conclude that since for large droplets the formation of ^2D state exciplexes is suppressed, the corresponding spectrum represents the actual $AuHe_N$ excitation spectrum.

4.2.4 In-droplet D2 line (41000 - 43770) cm^{-1})

4.2.4.1 $AuHe_N$ excitation spectrum - D2 transition

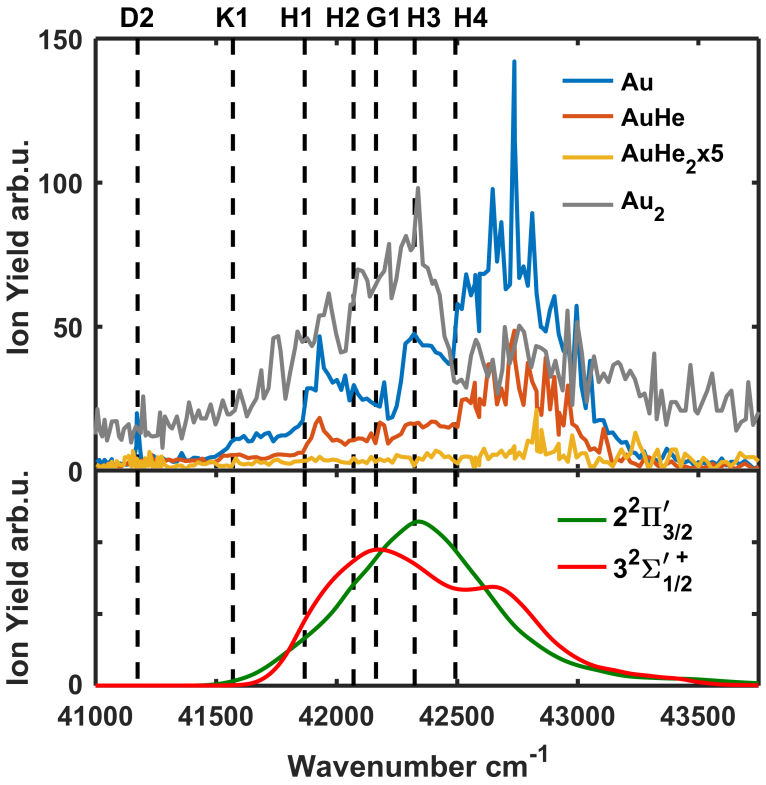

Figure 4.7: Upper picture: Excitation spectrum of gold atoms inside helium nanodroplets He_N with N = 1.25 x 10^4 from 41000 to 43770 cm^{-1}. The ion yields for Au (blue), AuHe (red) and $AuHe_2$ (yellow) are shown as a function of the excitation laser wavenumber. The bare atom $6p\,^2P_{3/2} \leftarrow 6s\,^2S_{1/2}$ transition (D2 line) is located at 41175 cm^{-1}. The broad structure extending from 41500 to 43300 cm^{-1} is attributed to the broadened and blue-shifted in-droplet D2 transition of gold atoms inside helium droplets. The spectrum is superimposed by features that coincide with bare atom transitions, marked by dashed vertical lines and listed in table 4.4. These transitions originate from atoms relaxed into the lowest ^2D states. The dimer spectrum recorded for large helium droplets (N = 2 x 10^6) is shown in gray in the background. Lower picture: The green and red lines correspond to the calculated spectra for the transitions from the $X^2\Sigma'^+_{1/2}$ ground state into the $3^2\Sigma'^+_{1/2}$ and $2^2\Pi'_{3/2}$ states that arise from the $^2P_{3/2}$ asymptote.

Figure 4.7 shows the Au (blue), AuHe (red) and $AuHe_2$ (yellow) ion yield recorded for the spectral region from 41000 cm^{-1} up to 43770 cm^{-1} for helium droplets He_N consisting on average of N = 1.25 x 10^4 He atoms. The calculated spectra are plotted below

as a red and a green line, for the $3^2\Sigma'^+_{1/2} \leftarrow X^2\Sigma'^+_{1/2}$ and $2^2\Pi'_{3/2} \leftarrow X^2\Sigma'^+_{1/2}$ transition. The bare atom Au $6p\,^2P_{3/2} \leftarrow 6s\,^2S_{1/2}$ D2 transition is located at 41175 cm^{-1}. A broad structure spanning almost over the entire recorded spectral range can be observed in the center of the figure (41500 - 43300 cm^{-1}). As in the D1 spectrum (cf. figure 4.3), atomic transitions are marked as vertical, black, dashed lines in figure 4.7 tagged with abbreviations that can be compared to the transitions listed in table 4.4. The structure exhibits a variety of features, in particular, various rising edges coinciding with vertical lines that mark the position of electronic transitions in bare Au atoms. Note that compared to the in-droplet D1 transition, the obtained ion yield is much stronger (approximately x 3) for the in-droplet D2 transition.

4.2.4.2 In-droplet D2 line

Considering the AuHe pair potentials, the $6p\,^2P_{1/2}$ state gives rise to a single $2^2\Pi'_{1/2}$ state, whereas for the $6p\,^2P_{3/2}$ asymptote, two different states emerge, i.e. the $2^2\Pi'_{3/2}$ and the $3^2\Sigma'^+_{1/2}$ state. This follows from the different possibilities for the orientation of the P orbital with respect to the internuclear axis. When introduced into the center of a helium droplet (or bulk helium), in principle, the $2^2\Pi'_{3/2}$ and $3^2\Sigma'^+_{1/2}$ states are degenerate because the system bears spherical symmetry. However, this is just true in a first approximation, because the bubble in which the atom is accommodated is oscillating and the atom can move inside the droplet. In the present calculation, the spherical symmetric breathing mode and the quadrupole mode has been considered in order to introduce a line-broadening. In the scenario proposed by Yabuzaki *et al.* [49] it is suggested that higher orders (such as the quadrupole mode) lead to a dynamic Jahn-Teller effect. This results in a breaking of the symmetry of the system, which lifts the degeneracy of the two states. Such a line splitting has been observed experimentally for systems comparable to Au such as Cs and Rb atoms [49], Ag atoms [68] and Ba^+ ions [115] in helium nanodroplets. In our calculation the energetic splitting is marginal, while the shapes differ a lot from each other, as can be seen in figure 4.7.
Similar to the in-droplet D1 line, we assign the underlying broad structure extending from 41500 to 43300 cm^{-1} to the broadened and blue shifted in-droplet D2 transition. This is in good agreement with the calculations, where the in-droplet transitions show about the same width. Already based on a comparison to $CuHe_N$ [67] and $AgHe_N$ [68] it can be expected that this transition is broader than the in-droplet D1 transition because it comprises of transitions from the $X^2\Sigma'^+_{1/2}$ ground state into both the $2^2\Pi'_{3/2}$ and the $3^2\Sigma'^+_{1/2}$ states [15]. A comparison to the calculated spectrum suggests also that the transition is buried below all the superimposed features that dominate the spectrum.

4.2.4.3 Atomic D2 line and unidentified sharp features

The bare atom D2 transition can be seen in the spectrum at 41175 cm^{-1}. The observation of bare Au atoms in the ionization region is attributed to atoms excited to the in-droplet D2 line with subsequent relaxation and ejection. These bare atoms are then two photon ionized outside of the droplet. This is in analogy to the atomic D1 line in

figure 4.3. When comparing the atomic D1 and D2 lines to their in-droplet counterparts, one sees that the atomic D1 line has a much stronger relative yield than the atomic D2 line. This can be attributed to the fact, that the D1 line is positioned at an energy, where the in-droplet D1 line already possesses a significant yield (cf. figure 4.3), unlike the atomic D2 line, which is located at an energy, where the in-droplet D2 line has a very low yield. This observation supports the assignment of both the atomic D1 and D2 line to relaxed and ejected groundstate atoms, following an excitation through the in-droplet D1 and D2 line.

Close inspection of the spectrum reveals the presence of multiple sharp lines in the region between 42570 and 43130 cm^{-1}. The position of these lines is reproducible for different droplet sizes and for different laser dyes and photon intensities. A scan with higher resolution revealed that these lines are indeed very sharp (< 5 cm^{-1}), suggesting that they are of atomic or molecular origin of species not solvated inside the helium droplet environment. However, they do not coincide with any known atomic transition [54]. Molecular candidates would be $AuHe_n$ or Au_2He_n. As the lines are also visible in the AuHe ion yield at least one He atom has to be attached to the species. Unfortunately, spectra for such molecules, in particular in the respective spectral regime, are unknown. Certainly, bare atom transitions correspond to asymptotes of molecular states, however, the number of possible intermediate molecular states becomes very large considering the selection of possible asymptotes in table 4.4. Consequently, the origin of these lines remains obscure and eludes from a conclusive interpretation without further support from theory or gas phase experiments.

A possible explanation may involve transitions into excited states of the Au^+He_n ion, where upon excitation the chances of Au^+He_n ions to leave the droplet are increased. A similar scenario was observed in the spectroscopy of the Ba^+He_N system, where ground state Ba^+ was found to be immersed inside the droplet, but upon population of excited states of the ion (in particular, the D1 and D2 transition), Ba^+ and Ba^+He complexes were found to be ejected from the droplet. However, the situation in the singly ionized Au system (Au II) is complex with many possible transitions in this region, with some of them matching the observed sharp lines. Beside the very speculative character of this scenario, such an origing would contradict the atomic, sharp form of the observed features.

In this context it is interesting to discuss a peculiarity of the Au atom related to the $5d^9 6s_{1/2} 6p_{1/2}\, {}^4P_{5/2} \leftarrow 5d^{10}6s\, {}^2S_{1/2}$ transition, which may contribute to the unassigned features between 42570 and 43130 cm^{-1}. This transition lies only about 1000 cm^{-1} above the bare atom D2 line, marked as G1 transition in figure 4.7. Our calculation, not including spin-orbit interaction, suggests a blue-shift of about 350 cm^{-1}. Considering that the state is very close to the ${}^2P_{3/2}$ state, the corresponding wave functions are expected to mix and transitions from the ground state into states arising from the ${}^4P_{5/2}$ asymptote may gain transition probability. However, according to our calculations this increase should be low in the respective Franck-Condon window and we do not assume a significant contribution of this transition to the observed signal, in agreement with matrix isolation experiments [23, 31, 33, 64] where transitions from the ground state into states corresponding to the ${}^4P_{5/2}$ asymptote have not been identified.

4.2.4.4 K1, H1, H3, H4 transitions

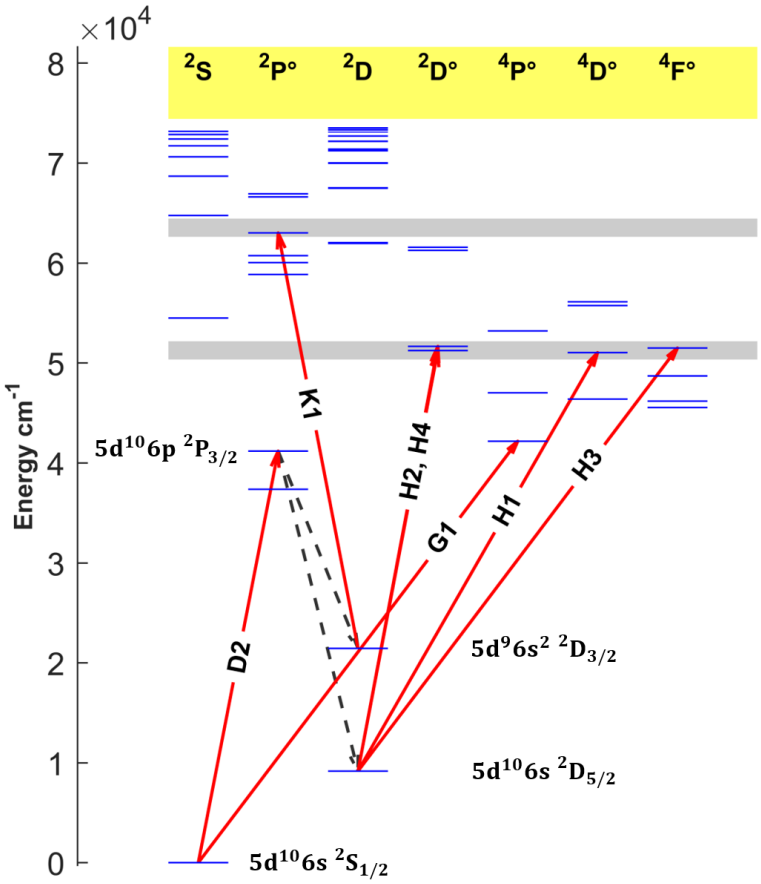

Figure 4.8: Grotrian diagram of Au. The states (blue horizontal lines) are sorted corresponding to their total orbital angular momentum L, their total spin S and their parity (° for odd, no superscript for even) i.e. $^{2S+1}L^{\circ}$. Transitions identified in the spectrum following the D2 excitation are drawn as arrows (red - excitation, black - possible relaxation pathway). The gray shaded areas mark the spectral interval from 41000 to 43300 cm^{-1} (cf. figure 4.7) from the view point of the $5d^96s^2\,{}^2D_{3/2}$ and $5d^96s^2\,{}^2D_{5/2}$ states.

As far as known to the author, the shape of the observed structure superimposing the in-droplet D2 line does not resemble any previously reported spectra. However, from the discussion of the in-droplet D1 line above, it can be expected that transitions originating from atoms in the lowest ^2D_J states contribute to the observed spectrum. In fact, some of the rising edges of the steps visible in the spectrum coincide exactly with the bare atom transitions originating from the lowest ^2D_J manifold, indicating that these states

are indeed responsible for the features that dominate this part of the spectrum.
Such a scenario is indicated in the Grotrian diagram in figure 4.8 by red (excitation) and dashed black (relaxation) arrows. The gray shaded areas mark the energy region from 41000 cm^{-1} to 43300 cm^{-1} (cf. figure 4.7) with respect to the lowest two $5d^9 6s^2\, ^2D_J$ states. The transitions originating from the ^2D_J states are indicated by vertical dashed black lines in figure 4.7, the annotations are explained in table 4.4. The bare atom K1, H1 and H4 transitions coincide exactly with rising edges in the Au spectrum which are, consequently, attributed to atoms relaxed into both the $^2D_{3/2}$ (K1) or $^2D_{5/2}$ (H1, H3, H4) state. The transition marked with H3 is attributed to the rising edge slightly below the vertical bare atomic transition line in the spectrum. From these states the atoms are two-photon ionized via the respective resonant intermediate state, as listed in table 4.4. As discussed above, a surface location of ^2D_J state Au atoms is not expected based on the calculation of solvation energies. Both scenarios introduced above, i.e. (i) an excitation and subsequent relaxation (as indicated in figure 4.7) as well as a (ii) two photon ionization, subsequent recombination and relaxation serve still as possible explanations for the observation of ^2D_J state atoms. The presence of a resonant intermediate step may favour the scenario (i) in which the in-droplet D2 line is resonantly excited and the atoms subsequently relax directly from this state into the ^2D_J states. The widths of the features H1 and H3 are very similar to the peak widths of the features located at the bare atom B2, C1 and C2 transitions at the D1 line (figure 4.3). This suggest that also in this spectral regime ejected $AuHe_n$ exciples are the source for spectral features that superimpose the in-droplet D2 line spectrum. However, the interaction of the helium environment with an atom in the $^2P_{3/2}$ state is different than for the $^2P_{1/2}$ state, in particular, considering that the $2^2\Pi_{3/2}$ state is strongly bound to the droplet with an increased probability to be found at the surface (cf. figure 4.2). If a $2^2\Pi_{3/2}$ state Au atom is ionized on the surface of the droplet, it would not lead to signal in the TOF spectrometer, because ions are known to sink into the helium droplet. Atoms in this state are not ejected and therefore may contribute to the population of ^2D_J state atoms due to very efficient relaxation pathways.

Table 4.4: List of transitions relevant for the D2 line excitation spectrum. The transitions are shown as vertical lines in figure 4.7 using the abbreviations listed below. Transition energies $\Delta\overline{\nu}$ are taken form ref. [54] and rounded to the last digit.

Initial state		Intermediate state		Abbreviation	$\Delta\overline{\nu}$ [cm^{-1}]
$5d^{10}6s$	$^2S_{1/2}$	$5d^{10}6p$	$^2P_{3/2}$	D2	41175
$5d^{10}6s$	$^2S_{1/2}$	$5d^9_{5/2}6s_{1/2}6p_{1/2}$	$^4P_{5/2}$	G1	42164
$5d^96s^2$	$^2D_{3/2}$	$5d^9_{3/2}6s_{1/2}6p_{3/2}$	$^2P_{5/2}$	K1	41570
$5d^96s^2$	$^2D_{5/2}$	$5d^9_{5/2}6s_{1/2}6p_{3/2}$	$^4D_{7/2}$	H1	41868
$5d^96s^2$	$^2D_{5/2}$	$5d^9_{5/2}6s_{1/2}6p_{1/2}$	$^2D_{3/2}$	H2	42070
$5d^96s^2$	$^2D_{5/2}$	$5d^9_{5/2}6s_{1/2}6p_{3/2}$	$^4F_{3/2}$	H3	42324
$5d^96s^2$	$^2D_{5/2}$	$5d^9_{5/2}6s_{1/2}6p_{3/2}$	$^2D_{5/2}$	H4	42493

4.2.5 Droplet size dependence - D2 transition

Figure 4.9 shows the spectra obtained for the Au (bright) and AuHe (dark) ion yields for three different He_N sizes with $N = 2$ x 10^6 (red), $N = 1.25$ x 10^4 (green) and $N = 9$ x 10^3 (blue). The same trend as above for the in-droplet D1 transition is observed: With increasing droplet size, the relative intensity of superimposed features decreases. The red Au and AuHe spectra thus resemble a situation in bulk helium and transitions originating from the ^{2}D state exciplexes are quenched. Furthermore, it can be seen that the feature between 42570 to 43130 cm^{-1} differs in its droplet size dependent behaviour from the step-like features in the spectrum that have been pinned to transitions originating from ^2D_J state $AuHe_n$ exciplexes, indicating that the species responsible for the sharp lines in this region have a different origin. Thus, the entire structure ranging from 41500 to 43300 cm^{-1} is assigned to both the $2^2\Pi'_{3/2}$ and the $3^2\Sigma'^+_{1/2}$ component. We note, however, that the form may be affected by additional features between 42570 cm^{-1} to 43130 cm^{-1}.

In the case of the in-droplet D2 transition the possible influence of dimers and larger oligomers, which, as will be shown below, exhibit an absorption band close by the free atom D2 line, has to be considered. For sake of comparison, the dimer spectrum from figure 4.11 has been plotted in gray in figure 4.7. It can be seen that, while the dimer spectrum exhibits a maximum around the feature assigned to the in-droplet D2 line, it does not feature the structure in the 42570 to 43130 cm^{-1} regime. The possible implications of this observation will be discussed in the next section. Most importantly, the dimer spectrum does not feature the superimposed structures with various rising edges and consequently, we exclude the possibility that dissociated dimers or trimers are a source of ^{2}D state exciplexes.

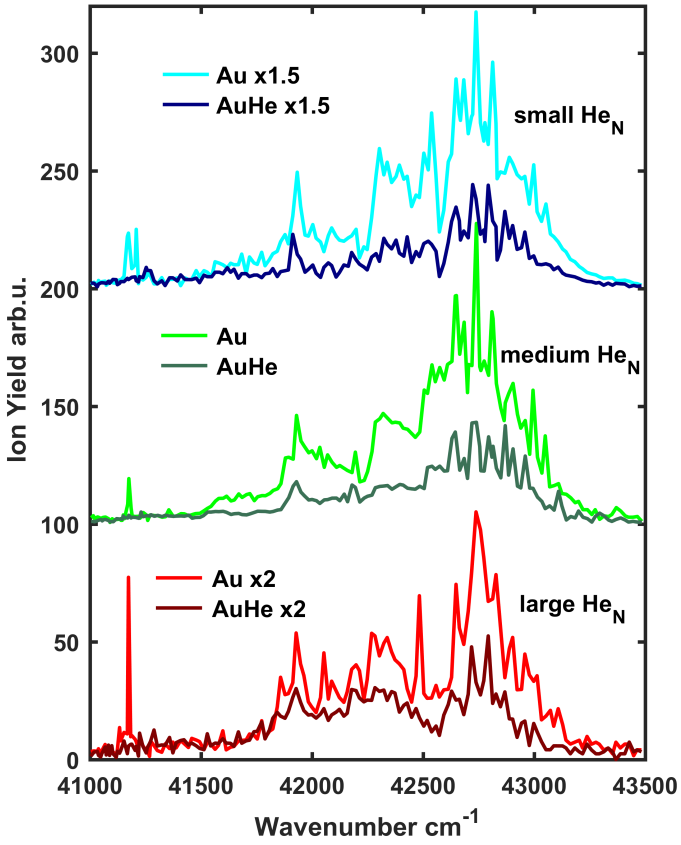

Figure 4.9: Excitation spectrum of gold atoms in helium nanodroplets in the spectral region containing the $6p\,^2P_{3/2} \leftarrow 6s\,^2S_{1/2}$ transition (D2 line) for helium droplet sizes of He_N with $N = 2$ x 10^6 (red), $N = 1.25$ x 10^4 (green) and $N = 9$ x 10^3 (blue). The ion yields for both Au (bright) and AuHe (dark) are shown.

4.2.6 Gold oligomers

In addition to the mass regime correlating to single Au atoms, the ion yield for larger Au_n oligomers was simultaneously recorded as a function of the excitation laser wavenumber. For small droplets the doping conditions have been optimized for maximum single atom pickup and therefore spectra for Au dimers or trimers could not be recorded due to their low abundance. In the largest employed helium droplets generated at the lowest nozzle temperature of 12 K, however, also Au oligomers are formed in a significant amount. In figure 4.10 we present a typical mass spectrum recorded for helium droplets He_N with mean sizes of $N = 2$ x 10^6. A pronounced even-odd oscillation is observed with the exception of the Au_2 dimer. Such a behavior is very typical for alkali and coinage metal clusters and reflects the stability of spin-paired valence electrons and closed shell cluster ions [18]. Magic numbers in systems consisting of atoms with a single valence

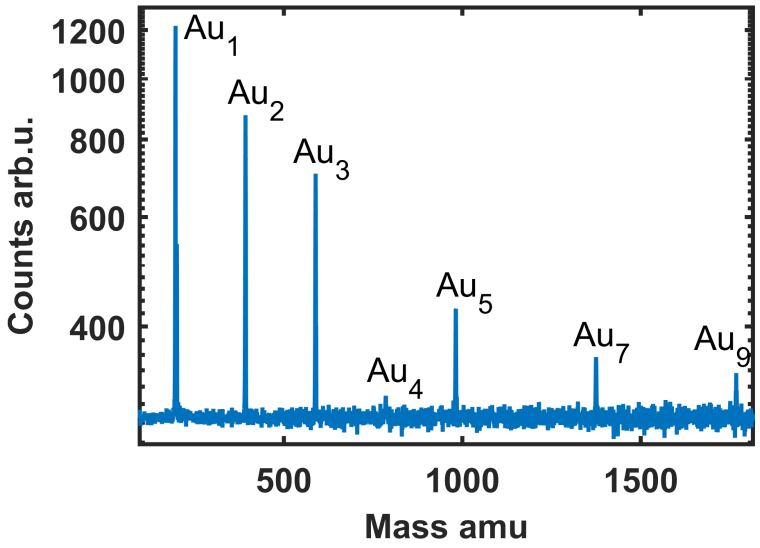

Figure 4.10: Integrated TOF mass spectrum over all recorded spectra for large helium droplets He_N consisting on average of $N = 2$ x 10^6 He atoms.

electron typically occur when the number of delocalized electrons in the cluster corresponds to $n_e = 2, 8, 18, 20, ...$, a rule which has also been found to apply for gold clusters [8, 46], and in particular, also for Au clusters embedded in helium droplets upon electron impact ionization [98]. Interestingly, this is also observed in this work with laser ionization, where the excess energy is a lot smaller than with electron impact ionization ($E_{electron} = 90\ eV$). Similar results have also been reported for alkali oligomers in helium nanodropets [101]. In this context, it is important to remember that the TOF mass spectrum reflects the stability of the ionized species, convoluted by the pickup distribution (assuming similar ionization cross-sections) and not the actual abundance of clusters formed inside the helium droplet. Furthermore, fragmentation of larger clusters may also affect the observed cluster size distribution. Ionized gold clusters with an odd number of Au atoms correlate to an even number of valence electrons. The largest observed cluster in figure 4.10 is the Au_9 cluster, which corresponds to the magic number of eight electrons. The yield for clusters beyond Au_9 is too low to be detected in the TOF mass spectrometer at the chosen conditions.
Already in the early days of helium nanodroplet isolation spectroscopy it was realized that high-spin dimers and trimers can be formed and studied with helium droplets because the survival of weakly bound species is favored upon the formation of the molecular bond [39, 83]. Even though even-odd oscillations and the shell closure at $n_e = 8$ are observed, which would be characteristic for low-spin oligomers, from the discussion above it follows that it cannot be excluded that neutral high-spin Au oligomers or other more complex structures [89] are formed upon pickup before ionization takes place. More likely, both high- and low-spin species are formed in the helium droplet similar to what has been observed for Ag_2He_N [90].

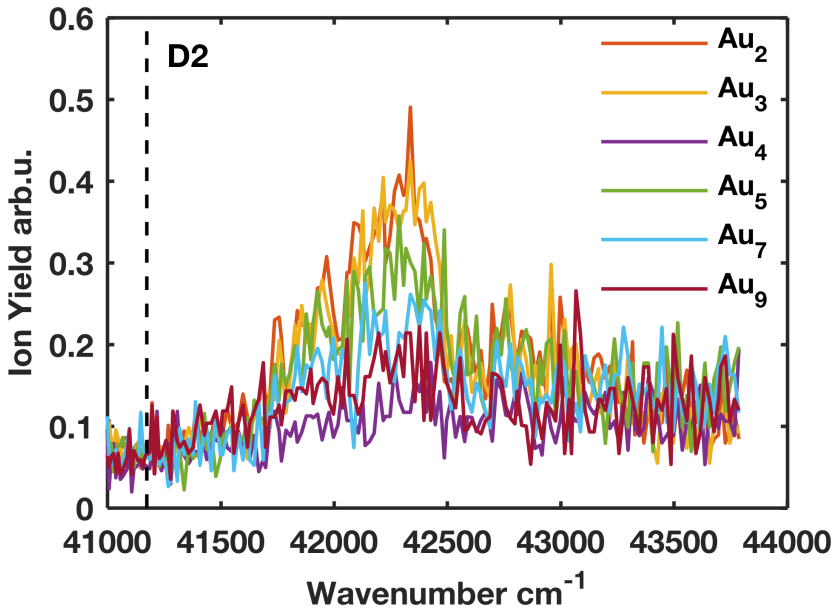

Figure 4.11: Excitation spectrum of gold oligomers in helium nanodroplets recorded for droplets He_N consisting on average of $N = 2$ x 10^6 He atoms. The atomic D2 line is represented by the vertical dashed line.

The observation of stable Au oligomers demonstrates that a spectroscopic investigation of these species is possible in large helium droplets. But even though the ionization process is very soft, the ionizing photon provides a few 100 to 1000 cm^{-1} of excess energy to the system, which may also lead to fragmentation of the oligomer as one possible dissipation mechanism besides a release of energy in form of kinetic energy of a photoelectron or in form of vibrational energy stored in the ionized oligomer.
Figure 4.11 shows the ion yield recorded for different Au oligomers as a function of the excitation laser wavenumber. Note that we only show the ion yield from 41000 to 43500 cm^{-1}, i.e. the regime that contains the D2 line. The ion yield below the D2 line was too low in order to warrant conclusions about possible features. This is similar to the finding noted above for the in-droplet D1 line, which showed an approximately 3 times lower ion yield than the in-droplet D2 line. Similar to bare atoms, Au oligomers can be two-photon ionized from the ground state in the respective photon energy regime. Among the oligomers, the low-spin (singlet state) Au_2 dimer has the highest ionization potential reported with 9.50 eV (76600 cm^{-1}) [43, 107].
Figure 4.11 reveals the presence of a resonant transition, peaking at about 42330 cm^{-1}, which, surprisingly, is observed at the same position for all oligomers. Interestingly, these features match the peak position attributed to the in-droplet D2 line quite well. Comparing these spectra to the results obtained from the spectroscopy of Au clusters in a neon matrix [64], suggests that some larger clusters exhibit transitions in the respective photon energy regime. For Au_2 and Au_3, spectroscopic results have been reported in argon [23] and krypton [33] matrices . Both report on Au_3 resonances in the investigated region at 231/258 nm (42290/38760 cm^{-1}) (Ar) and 233/255 nm (42918/39216 cm^{-1})

(Kr). Note that matrix effects are typically strong and influence the electronic properties of such small clusters, in particular, these effects depend strongly on the matrix element, among which He typically is the least perturbing matrix.
Even though some of the previous matrix isolation works reported transitions close to the resonance observed in figure 4.11, none of them reported a behavior in which the spectra for different mass channels resemble each other. Fragmentation of a cluster larger than Au_9 could account for this observation, however, atom-like transitions at oligomer mass channels seems to be a peculiarity of helium nanodroplet isolation spectroscopy and we favour a different explanation: Previous works, in particular, on magnesium doped helium droplets [89] but also on aluminum doped droplets [55] have proposed a scenario in which atoms separated by layers of helium form a metastable structure inside the helium droplet. This structure is thought to collapse upon laser excitation and ionization, giving rise to the detection of atom-like transitions in oligomer mass windows. Note that similar features have been observed for $SrHe_N$ [11]. The spectrum shown in figure 4.11 demonstrates that the size selective R2PI spectroscopy on gold oligomers in helium nanodroplets leads to similar results, calling for further experiments dedicated to the investigation of wider photon energy regimes, in particular, at lower energies where a multitude of absorption bands can be expected [64]. Note that this scenario could also explain the strong Au monomer in-droplet D1 and D2 line observed for large helium droplets while all other features are suppressed. As the pickup was optimized for monomers at small droplets and kept constant at large droplet sizes, the maximum of the pickup probability is far above the monomer pickup maximum and, statistically, monomers should not be present in a significant amount. However, if the atoms are separated inside the droplet, a detection of the corresponding monomer transitions would be expected.
Clearly, the observed spectral features raise new questions about fundamental aspects in the formation process of metal clusters in helium droplets. The results further suggest that the observation of monomer-like transitions in oligomer mass windows are a more general feature in helium droplet isolation spectroscopy. Taking this a step further, we note that it could be possible that at the largest employed droplet sizes vortices are already present in the droplets. For droplets bigger than 300 nm vortices were found, which was proven by doping with Ag and subsequent investigation of the elongated structures [28, 99]. Also in-beam, with Xe doped He droplets, diffraction pictures showed the presence of high density vortex droplets for helium droplets bigger than 300 nm [27]. As known to the author there is no literature that states a sharp border between droplet sizes with and without vortices. A conclusion in which size regime vortices start to appear is yet to attain, and experimentally hard to grasp due to the rather indirect measurement through dopant pickup. However, ref. [16] suggests that individual atoms can be captured by vortices and the expected effects on the spectrum are moderate [38]. Thus, the observed features may represent the spectroscopic signature of atoms trapped at vortices inside helium nanodroplets, a conclusion, however, that demands further experimental and theoretical support.

Chapter 5

Summary

Within this thesis an experimental setup was established to conduct REMPI spectroscopy on atoms and oligomers inside helium nanodroplets. Theoretically the setup is capable of investigating transitions of arbitrary species inside helium nanodroplets. Possible limitations can be the solubility of the atom in the helium droplet, a vanishing ion yield for weak transitions or the inability to bring the desired species to gas phase. The most restrictive component is the laser setup itself. With the low repetition rate of 100 Hz, measurements last very long, which can be undesirable, considering possible instabilities of the doped helium droplet beam, due to the consumption of the doping material in the evaporation cells or variations in the stagnation temperature or pressure. Even temperature changes of the vacuum chamber, room, lasers, TOF spectrometer etc. should not be neglected. The dye laser itself offers a narrow bandwidth and a short pulse duration, nevertheless it may not be the best choice for such experiments. The degeneration of the dyes over time introduces an additional instability, besides the wavelength dependent efficiency of the dye, making a constant power output impossible to achieve. In the course of finding a balance between a preferably short measurement duration and a high signal-to-noise ratio, high photon intensities were unavoidable. Secondary effects resulting from the high powers, like e.g. the saturation of transitions, have not been observed, but may be present when probing atoms other than Au.
The calibration of the dye laser and the SHG stage as well as the TOF settings are explained in the appendix. The setup was optimized for the measurement of single Au atoms inside the droplets to conduct an experimental study of the D lines, i.e. the $6p\,^2P_{1/2} \leftarrow 6s\,^2S_{1/2}$ and $6p\,^2P_{3/2} \leftarrow 6s\,^2S_{1/2}$ transitions of Au atoms embedded in helium nanodroplets. Excitation spectra of both transitions have been investigated using the 1CR2PI scheme. Strongly blue-shifted and broadened transitions were observed due to the repulsive interaction between the Au valence electron and the surrounding helium. The experiment was accompanied by calculations performed by Johann Pototschnig, including a multiconfigurational self consistent field (MCSCF) approach and a multireference configuration interaction (MRCI) calculation. The shift and the broadening of the recorded transitions were well reproduced by theory. Both theory and experiment supported the conclusion that Au atoms are located inside the helium droplet. Interestingly, the experiments revealed that a considerable amount of metastable ^2D state atoms were present during the excitation process. The observation of transitions originating from these states in between the in-droplet D1 and D2 line indicated that a non-resonant

process was responsible for the population of these states. As the linewidths of these transitions were relatively narrow for in-droplet valence electron transitions and the corresponding peak shapes exhibited sharp rising edges, not shifted with respect to their bare atom counterparts, it was concluded that these transitions originated from $AuHe_n$ exciplexes, that have been ejected from the droplet. Two possible mechanisms for the generation of these exciplexes were discussed: (i) a near-resonant excitation and subsequent relaxation mechanism as well as a (ii) near-resonant two-photon ionization scenario with subsequent ion-electron recombination. The D2 line spectrum, in particular, was found to be dominated by transitions originating from the lower ^{2}D state. In this case the two proposed scenarios still apply, however, the transitions are resonantly enhanced, giving rise to an increased efficiency of the underlying formation mechanism. Intriguingly, for very large helium droplets (He_N with $N = 2\,x\,10^6$), the mechanism that led to the observation of the metastable ^{2}D state exciplexes was suppressed, providing a clean view onto the D line transitions without additional features on top.

Large helium droplets could be doped with multiple Au atoms, which enabled the simultaneous recording of excitation spectra for Au oligomers from Au_2 to Au_9. The mass spectrum revealed characteristic even-odd oscillations, well known for alkali and coinage metal clusters. A resonance was observed beyond the atomic D2 line. Surprisingly, the corresponding spectral peak exhibited a similar shape for all oligomer sizes. However, the fact that the recorded transitions resembled each other in the spectra of different cluster sizes indicates that the distribution of the neutral Au clusters did not correspond to the finally detected ionic distribution. Similar to the scenario proposed for metastable magnesium structures [89], it was presumed that at least a fraction of the Au atoms were separated from each other inside the droplet giving rise to atom-like transitions at oligomer mass channels.

We want to stress this finding, which puts fundamental aspects in our understanding of the cluster formation process in helium nanodroplets into a new light. If the atoms are indeed separated before the excitation, we anticipate that for large droplets vortices have to be considered in order to explain the experiments. A picture in which atoms are separated and threaded along vortices would expand the current prevailing picture that proposes single and multi center cluster aggregation and subsequent attachment to vortices [35, 106]. Given the increasing interest into the synthesis of metal clusters with helium nanodroplets, it is very important to find out if this is a general phenomenon or if it is only present at certain droplet size regions or doping levels. The results are thus calling for more detailed studies of this aspect in the formation of nanoparticles inside helium nanodroplets, which is of great interest considering that the method is currently transitioning from very fundamental research to first applications, for example, for the fabrication of catalytic active nanoparticles [114] for which helium nanodroplets provide a versatile inert and solvent free synthesis environment. The present work demonstrates that mass selective spectroscopy of gold oligomers in helium droplets is possible up to Au_9. As one of the great advantages of the helium nanodroplet approach is the formation of bimetallic species, starting from heteronuclear molecules [58, 83] and ranging up to core-shell clusters and nanowires [99]. It would be very interesting to employ this approach to study the optical properties of larger bimetallic species. Considering that the

field of plasmonics is currently reaching size limits where quantum effect are becoming increasingly important [94], this endeavor may be particularly valuable as it provides a bottom up view onto the optical properties of these species and their evolution with cluster size.

Chapter 6

Appendix

6.1 Settings chosen in the TOF spectrometer software

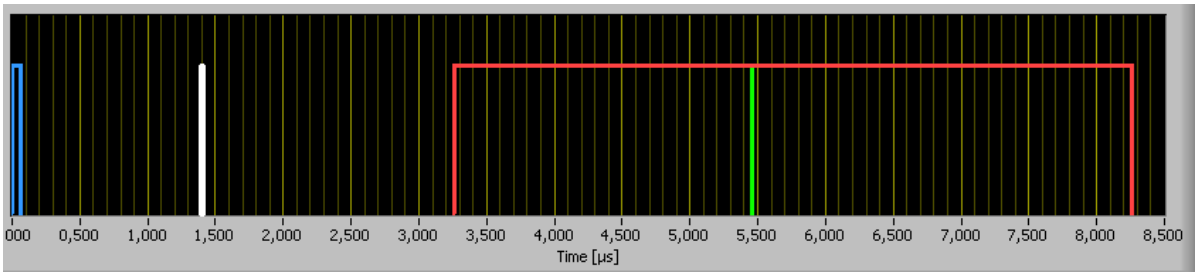

Figure 6.1: This figure shows the time delays between the different pulses in the TOF mass spectrometer. Blue: electron ionization window; white: laser ionization pulse; red: extraction window; green: mass filter window.

In the software of the TOF spectrometer many different adjustments can be altered to optimize the measurement. Crucial operating conditions are the time delays and pulse durations of the signals produced by the pulse generator, as well as the digitalizing options. The purpose of the pulse generator is to set a repetition frequency (if not externally triggered) and initiate the set delays. In our case, where the TOF spectrometer is triggered with an external trigger originating from the the pump laser, the pulse

Table 6.1: Table with the used fast multiscalar settings of the STEFAN KAESDORF RFT50.

Setting	value
present sweeps	3000
range	80000
bin width	4
time resolution [ps]	250
Fast DAC1	1
Fast DAC2	2
StartDisc.+/-1V	0.300
StopDisc.+/-1V	-0.150

generator just starts the electron ionization, the extraction and the mass filter at set times following the trigger signal. A picture of the set delays can be seen in figure 6.1. Blue marks the pulse for the electron ionization, red marks the ion extraction and green marks the mass filter. The delay between the trigger signal originating from the pump laser and the actual dye laser pulse was measured by a photodiode and is marked in the figure as a white line. The settings used are displayed in table 6.1 and 6.2. In the experiments the filament was not heated up, which makes the pulse duration of the electron gun obsolete. The mass filter options chosen in table 6.2 are just displayed for the sake of completeness, as the mass filter voltage was set to 0 V.
Nearly all TOF measurements were conducted with the "boxcar" mode of the mass spectrometer. Here, a series of consecutive mass spectra can be recorded. The time that is spend on a single spectrum can be set by different thresholds. The options are: "preset sweeps", where the number of ionization/extraction cycles can be set; "preset time", where the measurement time can be set; "preset counts" in the "region-of-interest", where one can define a region in the TOF spectrum as well as a threshold for the counts within this exact region. When the chosen quantity reaches the set value, the measurement is saved and a new one is started. For all spectra recorded, the "preset sweeps" option was chosen to make the specta comparable in terms of the ion yield.

Table 6.2: Table with the used pulse generator settings of the STEFAN KAESDORF RFT50.

Setting	value [μs]
Pulse duration electron gun	0.06
Delay ion extraction pulse - ionization pulse	3.2
Pulse duration ion extraction	5
Delay mass filter	0
Pulse duration mass filter	2.2
Delay external trigger - electron gun	0

6.2 Synchronized triggering of the devices

To operate all devices used for the experiment collectively, they need to be synchronized via different triggers. Most importantly, the TOF mass spectrometer needs to know at what time the ionizing laser pulse interacts with the helium droplet beam, in order to extract the produced ions and detect them. Another crucial component is the switching of the dye laser wavelength. As the individual mass spectra are captured in the "boxcar" mode, the switching of the dye laser wavelength has to be synchronized with the start of a new measurement. The trigger dependencies are depicted in figure 6.2. The first trigger is given by the pump laser with each pulse it emits. This optical signal can be obtained from the "Trig OUT" port. To convert the optical pulse into a digital TTL signal, that can be processed by a computer, it is guided into the "ADC" (the name was

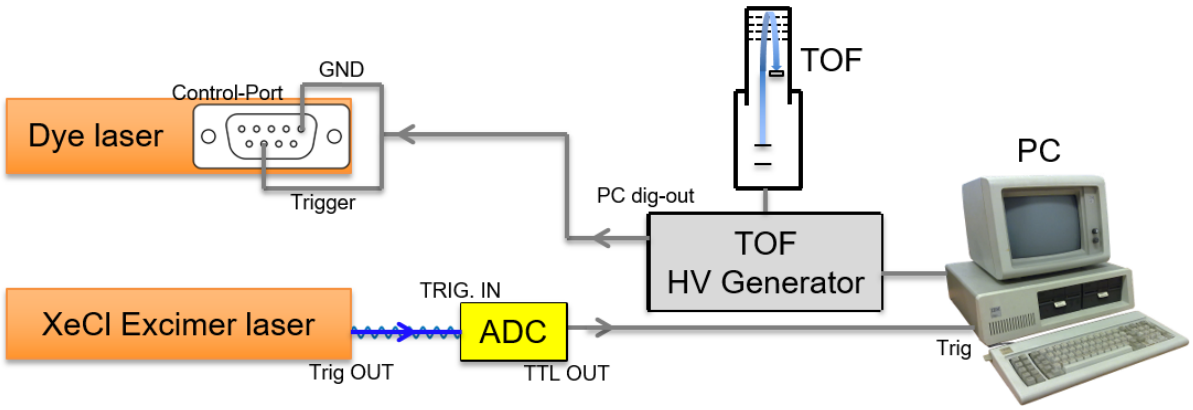

Figure 6.2: Sketch of the triggering between the different the pump laser, the dye laser, the HV control unit of the TOF mass spectrometer and the PC. The gray lines stand for coaxial cables with BNC connectors (except for the dye laser, where the coaxial cable is mounted to a DE-9 connector). The blue line with the oscillation stands for an optical fibre. All input and outputs are named according to the designation on the respective device. The despiction of the PC was taken from Wikipedia [1].

chosen in analogy to an analog/digital converter). The resulting TTL signal is directed to the "TRIG" port of the control board, which is installed in the PC via a coaxial cable and two BNC connectors. There the HV pulse generator of the TOF mass spectrometer is triggered (extraction of the produced ions). After a certain amount of laser shots (sweeps in the TOF), the measurement spectrum is saved and a new one is started. At the start of each new spectrum, a TTL pulse is provided by the BNC socket "PC dig-out". This signal is guided to the "Control Port" of the dye laser via a coaxial cable. As the "Control Port" is a DE-9 socket, the coaxial cable is mounted on a DE-9 connector. The TTL signal triggers the dye laser in order to switch the laser wavelength. The dye laser is therefore operated in the external trigger mode. By pressing the "EXT" soft key on the control panel the dye laser will skip the duration settings in the next wavelengths scans, featuring only the range and stepsize options.

6.3 XeCl pump laser Radiant Dyes RD-EXC-200

The XeCl excimer laser is shortly discribed in section 3, where the most important specifications are listed. The laser is operated through a PC interface, where settings like the repetition frequency, the high voltage for the discharge, and the pulse energy can be altered. With this interface, it is also possible to control the magnetic valves inside the pump laser, that are necessary for gas exchange and refill. The operation of the laser as well as a stepwise instruction for the pump gas exchange is given in detail in the appendix of [56], and is therefore not repeated here.

[1] PC [Online image]. Accessed: 2017-12-19. `https://de.wikipedia.org/wiki/Personal_Computer`

6.4 Setting up the Lambda Physics FL3002 dye laser

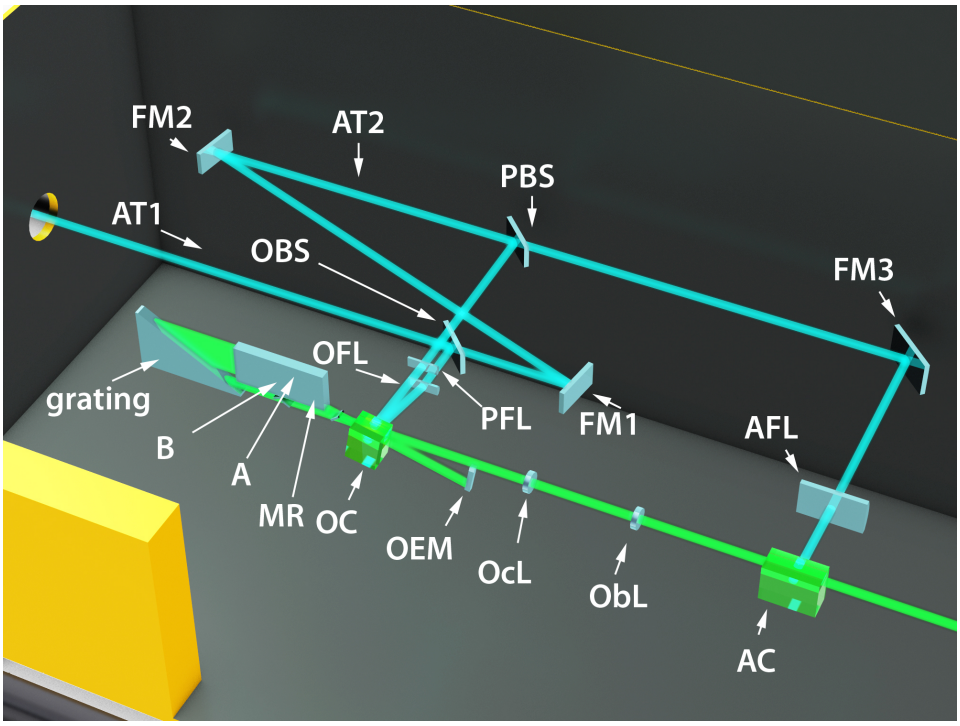

Figure 6.3: Schematics of the FL3002 dye laser. Light blue marks the optical path of the pumping laser beam and green marks the path of the dye laser beam. The picture is taken from [56]. The abbreviations mark following optical components:

AT1-2	... attenuators 1-2
FM1-3	... folding mirrors 1-3
OBS	... oscillator beam splitter
PBS	... preamplifier beam splitter
OFL	... oscillator focusing lens
PFL	... preamplifier focusing lens
AFL	... main amplifier focusing lens
grating	... tiltable grating
A	... prism beam expander; tilt control
B	... prism beam expander; exit prism control
MR	... monitor reflex
OC	... oscillator cuvette
OEM	... oscillator end mirror
OcL	... ocular lens
ObL	... objective lens
AC	... main amplifier cuvette

This section gives a summary of the most important steps when setting up the FL3002 from scratch. The content is based on the master's thesis of Günther Krois [56] and

the manual of the dye laser [61], to which it is referenced for further reading. In ref. [56] short operating and setup instructions are provided, but according to the writer of this thesis a few adjustments need to be made, concerning the section about the main amplifier and the power optimization.
When working with high intensity lasers, it is always crucial to wear laser goggles. Especially, UV laser sources which are not visible for the human eye, such as the XeCl pump laser or the second harmonic of the dye laser may constitute a great danger to the eyesight if not handled properly. The laser should always be blocked out, in particular, after passing the experimenting zone to avoid an uncontrolled reflection across the room. Therefore, no shutter should be opened before the exact location is known where the laser hits an obstacle. To minimize the general risk it is advised to work at the lowest possible output power when setting up the laser. This includes a low repetition frequency and swung in attenuators.
The most important components of the dye laser are designated in figure 6.3. In the following the working principle of the FL3002 is explained shortly (cf. figure 6.3): The pump laser pulses (light blue) enter the dye laser from the left. Two attenuators AT1 and AT2 can be swung in, to lower the pump laser power. They are mainly used for the setup of the dye laser. The pump laser is reflected by the folding mirrors FM1, FM2 and FM3. About 10% of the pump laser power is reflected by the beam splitters OBS and PBS. The dye laser pulse is created in the cavity of the oscillator (cf. figure 6.6). The oscillator consists of a wavelength-selective grating, a prism expander, the laser active medium (Oscillator cuvette OC) and a mirror (OEM). The pump laser intensity that is reflected by the OBS is focused by the oscillator focusing lens (OFL) and pumps the dye that is contained in the OC. The blazed grating in Littrow configuration only reflects one particular wavelength, depending on the tilt angle. Therefore, it also acts as the second mirror of the cavity. The wavelength selected laser light is guided back though the OC passing above the OEM. The pump laser light that is reflected by the beamsplitter PBS is focused with the PFL into the OC, pumping the dye in a second region, exactly where the dye laser beam leaves the oscillator. Consequently, the laser beam is amplified. With the ocular lens OcL and objective lens ObL the path of this preamplified laser beam is modified to reach the main amplifier stage. The main amplifier cuvette AC is pumped by the pump laser light ($\sim$ 80 % of the total pulse energy), reflected by the folding mirror FM3 and focused by the main amplifier focusing lens AFL. When the preamplified laser beam passes through the AC, it is amplified to its final intensity through induced emission.

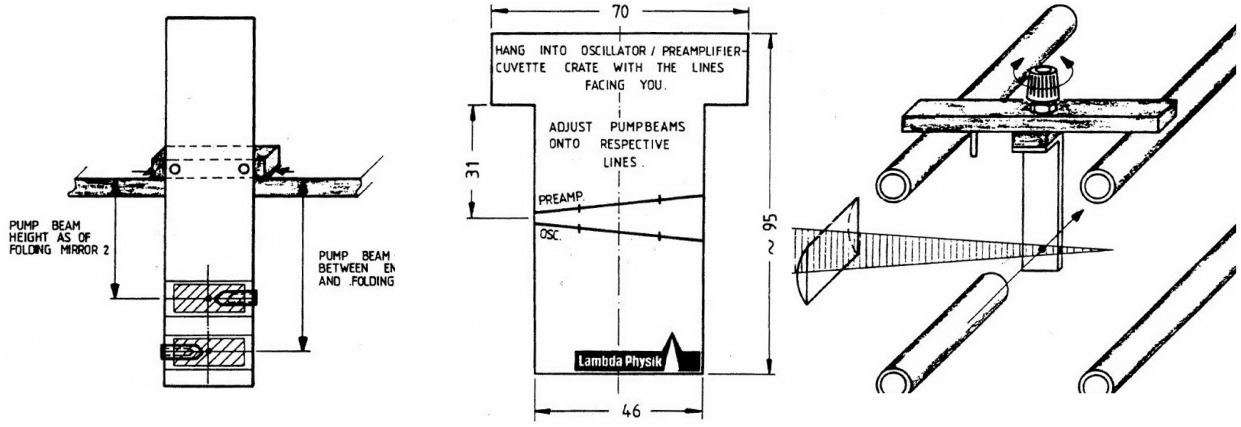

(a) Pump beam tool (b) Cuvette focusing tool (c) Dye beam tool

Figure 6.4: The different tools which are needed for the setup of the dye laser. The pump beam tool (a) is for adjusting the height of the pumping laser beam, such the folding mirrors are optimally illuminated. The cuvette focusing tool (b) is for the adjustment of the oscillator focusing lens (OFL) and preamplifier focusing lens (PFL). The dye beam tool (c) is for monitoring and alignment of the dye laser beam. Taken from [56].

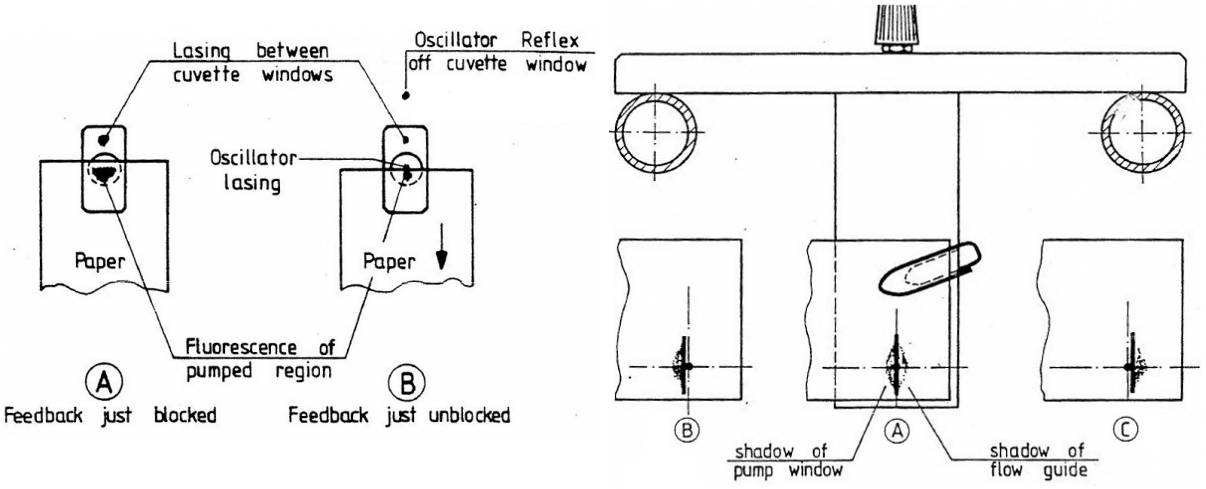

(a) Oscillator separation (b) Dye beam shape

Figure 6.5: Viasual references to compare to, when optimizing the oscillator beam. (a) Ⓐ/Ⓑ shows the separation of the oscillator beam from the amplified spontaneous emission (ASE). (b) Ⓐ/Ⓑ/Ⓒ shows the shape of the oscillator beam. The goal is to minimize the interaction with the OC window and the flow guide. Taken from ref. [56].

6.4.1 Pump beam path

The first thing to do, is to guide the pump laser beam into the dye laser. In the end, the optical path should follow the one displayed in figure 6.3. The following steps have to be performed according to the manual [61]:

1. The pump laser should be aligned as parallel as possible to the dye laser (horizontally and vertically). The beam should not be obstructed by the rectangular entry port.

2. Block the pump beam. Remove the OC and AC. Remove FM1, FM2 and FM3.

3. Put the pump beam tool (figure 6.4a) in the position, where FM1 should be. Unblock the pump beam and bring it onto the lower rectangular area of the pump beam tool either by tilting the pump beam (if everything is parallel, only slight changes need to be applied) or by tilting the dye laser itself with the adjustable feet.

4. Block the pump beam. Put back FM1 and place the pump beam tool where FM2 should be. Unblock the pump beam and bring the pump beam onto the upper rectangular area of the pump beam tool. This is done by adjusting the orientation of the FM1 with the horizontal an vertical alignment knobs.

5. Block the pump beam. Put back FM2 and place the pump beam tool where FM3 should be. Unblock the pump beam and bring the pump beam onto the upper rectangular area of the pump beam tool, using the knobs on FM2. Block the pump beam and put back FM3.

6. The main pump beam path is now set up properly. Now the beamsplitters have to be adjusted. Swing in attenuators AT1 and AT2. The pump beam should now be blocked by the holder of the cuvettes. In the next step, the OBS, PBS and FM3 need to be tuned, in a way such that the corresponding cylindrical lenses OFL, PFL and the AFL are fully illuminated. The easiest way to do this is with a piece of paper, which can be slid in between the beamsplitter/mirror and the corresponding lens. When doing this, it is very important to wear laser goggles. Also try to avoid skin exposure to the pump laser light.

7. Put in the cuvette focusing tool (figure 6.4b) where the OC should be. Tune the horizontal and rotation knobs to bring the two lines together. The point of focus can be altered by changing the distance between the lens and the cuvette (maybe the position of the lens on the lens holder has to be modified, if the focus cannot be altered sufficiently). Bring the oscillator beam (lower line) another 5 mm below the marked line. Now change the focus by shifting the lenses OFL and PFL back and forth. The position of the oscillator and preamplifier beam must not change. If this is not the case, adjust the OBS and PBS until it does not move any more.

8. The procedure for the AFL is quite similar. Put in the dye beam tool (figure 6.4c) where the AC should be. Overlap the main amplifier beam with the pinhole on the dye beam tool. Adjust FM3 until the focus-defocus procedure does not move the main amplifier beam any more.

6.4.2 Oscillator

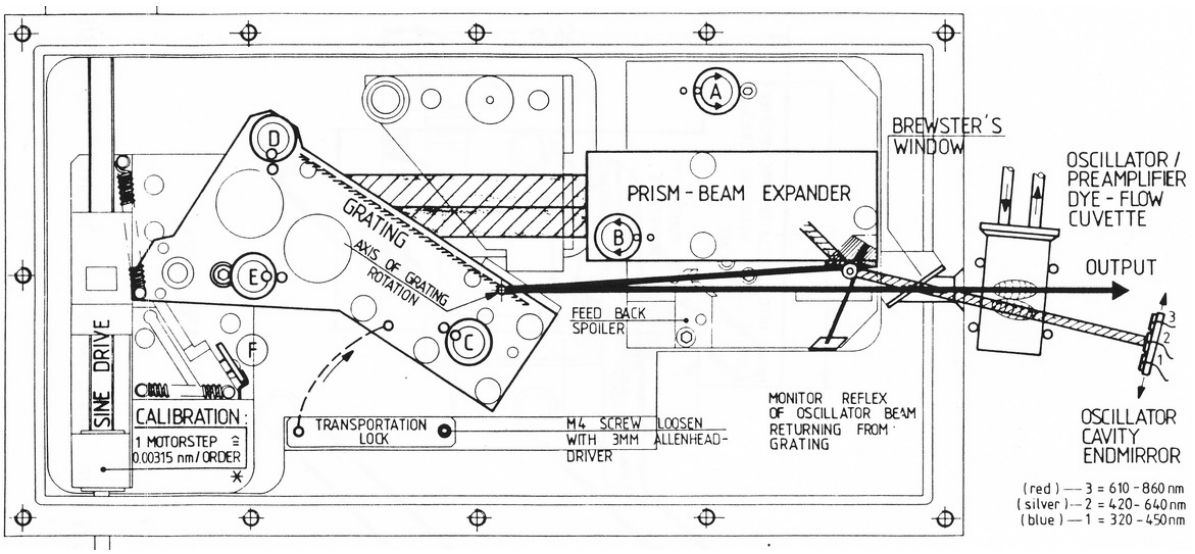

Figure 6.6: Schematics of the FL3002 dye laser oscillator taken from ref. [56].

.

The Oscillator is depicted in figure 6.6. The wavelength selection is performed with a tiltable blazed grating in Littrow configuration. The selected wavelength is reflected back in the exact same direction as the incoming light. To set up the oscillator, the following steps have to be performed according to the manual [61].

1. Block the pump laser beam. Block the preamplifier beam by hanging the pump beam tool with the shorter side in the opening between OFL/PFL and OC. Block the main amplifier beam between PBS and FM3 with another pump beam tool or any other highly absorbing obstacle. Block the dye laser beam by closing the exit of the dye laser. Swing in both attenuators AT1 and AT2.

2. Insert the OC. Turn the grating to the lasing maximum of the used dye by using the softkeys on the dye laser.

3. Unblock the pump beam. Swing out AT1. Adjust the height of the oscillator beam until a rectangular shaped spot (MR) is visible on the bottom of the oscillator block and a bright line appears on the grating. Note, that the dye laser output can hardly be seen before the setup is optimized.

4. If the oscillator is adjusted poorly and no lasing is visible, try to check the tilt of the OC (it should be parallel in the beginning) and the rotation of the oscillator beam. Also see if the right OEM is selected (610 - 860 nm → red, 420 - 640 nm → silver, 320 - 450 nm → blue). Check if the grating is set to the correct wavelength, if the dye is pumped correctly (no bubbles in the cuvette) and if the pump laser has enough power.

5. Swing in AT1. Slide in a stiff piece of paper between the OC and the OEM from below until the MR just disappears. The oscillator path is now interrupted. On the piece of paper the spontaneous fluorescence of the pumped region is visible as a diffuse unspeckled light patch. Another intense spot can be observed slightly above, which results from lasing between the OC windows. Holding the paper in place where the oscillator path is just interrupted, adjust the rotation of the OFL in a way such that the fluorescence center is just below the edge of the paper (figure 6.5a Ⓐ). This separates the amplified spontaneous emission (ASE) from the actual oscillator laser beam. As a result, both the fluorescence and the lasing between the OC windows should have decreased (cf. figure 6.5a Ⓑ).

6. Leave the AT1 in, if possible. Hang the dye beam tool (figure 6.4c) onto the upper two rods of the 4-rod optical bench between the ObL and the AC. The laser should now be visible with a shape similar to ones that are displayed in figure 6.5b. Adjust knob A until a form comparable to figure 6.5b Ⓐ is reached. If done correctly, the oscillator beam passes the OC optimally.

7. After tilting the prism beam expander, the oscillator path has to be optimized again. This is best accomplished at threshold conditions (blue end). If one has a steady hand, the grating can be lifted manually with one finger, while trying to optimize the output by adjusting knob B. The grid should therefore be kept in a position where the oscillator laser spot on the dye beam tool almost vanishes. Change the grating from maximum to threshold position. If the dye laser point jumps sideways, adjust B slightly until it is steady.

8. If the shape of the oscillator beam does not resemble the form in figure 6.5b Ⓐ iterate over steps 6 - 8.

9. With a 4 mm Allen head driver swivel the OC, until there is just a single line visible on the grating. If the primary line has satellites, try to merge them. This concludes the adjustment of the oscillator.

6.4.3 Preamplifier

The OC also works as a dye cuvette for the preamplifier. The goal is to overlap the second (preamplifier) pumped zone in the OC with the oscillator output.

1. Swing in attenuators AT1 and AT2. Place the dye beam tool between ObL and the AC on the 4-rod optical bench if not already there. Remove the pump beam tool

that blocks the preamplifier pump beam. A spot of higher intensity (preamplifier spot) should now appear on the dye beam tool.

2. While alternately blocking and unblocking the pump beam of the preamplifier with the pump beam tool (to see deviations of the oscillator and the bright preamplifier spot), bring the height of the preamplifier pump beam to a level where the oscillator spot coincides horizontally with the preamplifier spot by using the horizontal control of PFL.

3. If two spots do not coincide vertically repeat steps 5 - 8 of the oscillator setup to ensure that the oscillator beam passes the cuvette centrally (it should then resemble the shape of the spot in figure 6.5b Ⓐ)

4. Focus and defocus the PFL by losing up the PFL and moving it back and forth. The spot should not move, it should just defocus. If is does move, correct the PBS so that the pump beam hits the PFL cantrally.

6.4.4 Intermediate telescope

The telescope corrects the beam path such that the preamplified dye beam travels centrally to the AC.

1. Remove the AC. Swing in attenuators AT1 and AT2 (if the laser is poorly visible, try swinging out AT1 or AT2 individually).

2. Hang in the dye beam tool right behind the ObL. With the knobs of the OcL, bring the dye laser beam onto the pinhole of the dye beam tool.

3. Remove the dye beam tool and place it behind the AC as far away from the ObL as possible. With the knobs of the ObL, bring the dye laser point onto the pinhole again. Repeat steps 2 - 3 until no further modification are necessary.

6.4.5 Main amplifier

The goal is to overlap the pumped zone in the AC with the preamplified dye laser beam.

1. Block the pump beam. Block the pump beam path between PBS and FM3 either with the pump beam tool or any other high absorbing obstacle. Swing in AT1 and AT2. Put in the dye beam tool behind the AC. Place the AC back into its crate.

2. Unblock the pump beam. The preamplified dye laser beam is slightly shifted up because the AC is acting as a tilted parallel plate. The AC crate has two screws. One for swiveling and one for a parallel vertical shift. Move the AC crate with the screw for the shift to a position, such that the preamplified dye laser beam passes through the AC near the cuvette window.

3. Repeatedly unblock and block the main amplifier pump beam by moving the pump beam tool up and down. A bright spot should appear on the dye beam tool. Merge the preamplified dye leaser beam with the spot from the AFL by tuning the horizontal knob of the AFL.

4. Swivel the AC until all satellite reflexes merge with the primary spot.

5. Adjust the screw for the parallel shift for optimal brightness and beam shape.

Now all the dye laser beam paths are set up near optimum. The laser intensity may still be far off from its maximum.

6.4.6 Power optimization

For the power optimization a device capable of measuring the pulse energy with a fast response rate is needed. Ideally, a photo diode or joulemeter in combination with a dispersion lens and an attenuator can be utilized. The measurement can be visualized by an oscilloscope. Each part of the dye laser can and should be optimized individually in the following order: Oscillator - Preamplifier - Main amplifier. Other orders do not work because these parts build up on each other. The oscillator should not be optimized based on the bare output power, but instead one should also focus on a good beam shape and low ASE. This is already accomplished in the setting up of the oscillator described above.

1. Block the pump beam. Block the main amplifier pump beam. Put the joulemeter in front of the AC. Use attenuators (AT1, AT2 or external) if necessary. Unblock the pump beam.

2. Adjust the focus of the OFL for optimal output

3. Adjust the focus, beam height, and rotation of the PFL for optimal output (only pairs of heights and rotation may work).

4. Iteratively change knobs A and B to find the optimal path of the laser through the OC. For every A, B needs to be optimized to obtain a MR with maximal brightness and contrast.

5. Swivel the OC for maximal output. The ribbon on the grating may exhibit light satellites.

6. Reset the intermediate telescope, to a central position of the dye laser beam.

7. Place the joulemeter behind the AC. Use attenuators, otherwise the detector will get burnt.

8. Unblock the main amplifier pump beam. Adjust the height and the rotation of the main amplifier pump beam for maximum output, by tuning the knobs on the AFL. The measurement of the dye laser power is challenging, due to the fluorescence that can occur. The author experienced, that the best and easiest way to optimize the main amplifier is by measuring and optimizing the output of the second harmonic that is generated by a SHG crystal.

9. Adjust the focus of the AFL for maximum output and readjust the height of the AFL.

10. Move the AC with the screw for parallel shift for optimal output.

11. Swivel the AC to optimize output. Repeat steps 10-11.

The dye laser is now set to the optimal operation conditions. Note that the laser dyes degenerates faster with high pump laser powers and high repetition rates, therefore the energy as well as the repetition frequency should be chosen as low as possible for any non-measurement purpose such as adjustment operations or the guidance of the laser output to the experiment.

6.4.7 SHG crystals

To reach the desired energy region, a SHG crystal (BBO) was used to double the frequency of the fundamental dye laser pulses. Here the working principle of such crystals shall be explained shortly following ref. [9]. The phenomenon of frequency doubling is based on nonlinear effects in terms of light intensity inside a material. In classical linear optics, the polarization P (strength of the induced dipole moment per unit volume $\sim$ measure of the deviation of the averaged electron position from the averaged nucleus position) of a material is direct proportional to the electric field E.

$$P^{(1)} = \epsilon_0 \chi^{(1)} E \tag{6.1}$$

With ϵ_0 being the vacuum permittivity and $\chi^{(1)}$ being the linear term of the susceptibility (in general χ is a tensor). In the general case, also higher order terms contribute to the polarization. When Taylor expanding the polarization, equation 6.1 changes into a more complex form.

$$P^{(1)} + P^{(2)} + P^{(3)} + ... = \epsilon_0[\chi^{(1)} E + \chi^{(2)} E^2 + \chi^{(3)} E^3 + ...] \tag{6.2}$$

For simplicity reasons P and E are treated as scalar quantities. $\chi^{(2)}$ and $\chi^{(3)}$ are known as second and third order nonlinear optical susceptibility. In the case where the field E and polarization P are treated as vectors, the susceptibilities $\chi^{(1)}$, $\chi^{(2)}$, $\chi^{(3)}$, etc. are tensors of rank two, three, four, etc.. One can show that effects that are caused by the second order nonlinear polarization $P^{(2)} = \epsilon_0 \chi^{(2)} E^2$ can be clearly separated from effects caused by the third order polarization $P^{(3)} = \epsilon_0 \chi^{(3)} E^3$, leading to a hierarchy of intensity dependent physical processes. Second order effects include frequency doubling

or summation and optical rectification. Third order effects are e.g. the optical Kerr effect and frequency tripling or summation. The interaction of a monochromatic electromagnetic (EM) wave, as it is produced e.g. by a laser, with a nonlinear medium shall be discussed hereafter. A scalar EM wave has the form:

$$E(t) = E_0 \mathrm{e}^{-i\omega t} + c.c.\,. \tag{6.3}$$

E_0 is the maximal field of the EM wave, ω is the angular frequency, t the time and *c.c.* stands for the conjugate complex of the first term. The polarization in second order $P^{(2)} = \epsilon_0 \chi^{(2)} E^2$ will look like:

$$P^{(2)}(t) = 2\epsilon_0 \chi^{(2)} E E^* + (\epsilon_0 \chi^{(2)} E^2 e^{-i2\omega t} + c.c.). \tag{6.4}$$

The second order polarization consists of a term that does not oscillate (zero frequency) and a term that oscillates with the doubled frequency (2ω) of the incoming EM wave. The zero frequency term leads to the optical rectification, resulting in a static electric field across the nonlinear medium. The second term oscillating with 2ω can result in the emission of EM waves, as accelerated charges radiate. This wave is the second harmonic of the incident EM wave.
In general χ is a frequency dependent tensor, therefore the so-called phase matching is essential for the efficient generation of higher harmonics. When phase matching is achieved, the fundamental wave and the second harmonic have the same velocity inside the medium, assuring a fixed phase relation between them. Second harmonic waves emitted by the medium interfere constructively with the waves that were emitted earlier in the same direction. The result is a coherent, frequency doubled beam traveling in the same direction as the fundamental beam.
To ensure equal velocities of the SHG and the fundamental wave, the birefringence of crystals is used. The crystal is tilted until the ordinary (o) and extraordinary beam (eo) have the same index of refraction. For example for normal dispersion ($\frac{dn}{d\omega} > 0$) in negative uniaxial crystals:

$$n_{eo}(\omega,\theta) = n_o(2\omega,\theta). \tag{6.5}$$

Due to the use of birefringence, the SHG is always polarized normal to the polarization of the fundamental wave.

6.4.8 Calibration of the BBO crystal

A BBO (β-Bariumborat) crystal was used in all experiments to frequency double the pulses of the dye laser in order to get to the desired energy region. As explained above phase matching is accomplished by tilting the crystal. To operate the crystal at phase matching conditions for a wavelength range, a calibration has to be performed where angles are pinned to wavelengths. Within the dye laser, this is implemented via a stage where the crystal is mounted onto an electrical rotating arm. Another crystal beyond the BBO crystal is used to compensate the beam shift of the BBO crystal, which acts as a tilted parallel plate. When performing a calibration over a desired range by pressing

the "CAL" soft key, the laser divides the range into five equidistant points, where the operator manually optimizes the laser output signal. The laser then interpolates between the optimized points.
Note, that the fundamental dye laser beam that hits the BBO crystal should be vertically polarized. In this way the SHG wave is horizontally polarized, assuring that the frequency separator is operated near the Brewster angle for optimal performance. This can be accomplished by inserting a polarization filter in front of the AC. Optimally the filter which is included in the scope of supply of the dye laser is used. It can be placed in a holder, located at the support of the ObL in front of the lens.

Bibliography

[1] J. R. Adleman, D. A. Boyd, D. G. Goodwin, and D. Psaltis. Heterogenous catalysis mediated by plasmon heating. *Nano Lett.*, 9(12):4417–4423, 2009.

[2] V. Amendola, R. Pilot, M. Frasconi, O. M. Maragò, and M. A. Iatì. Surface plasmon resonance in gold nanoparticles: A review. *J. Phys: Condens. Mat.*, 29(20):203002, 2017.

[3] F. Ancilotto, M. Barranco, F. Caupin, R. Mayol, and M. Pi. Freezing of ^{4}He and its liquid-solid interface from density functional theory. *Phys. Rev. B*, 72(21):214522, 2005.

[4] F. Ancilotto, P. B. Lerner, and M. W. Cole. Physics of solvation. *J. Low Temp. Phys.*, 101(5):1123–1146, 1995.

[5] J. Bakos, A. Kiss, L. Szabó, and M. Tendler. Light intensity dependence of the multiphoton ionization probability in the resonance case. *Phys. Lett. A*, 41(2):163–164, 1972.

[6] G. P. Bewley, D. P. Lathrop, and K. R. Sreenivasan. SUPERFLUID HELIUM: Visualization of quantized vortices. *Nature*, 441(7093):441588a, 2006.

[7] A. Boatwright, C. Feng, D. Spence, E. Latimer, C. Binns, A. M. Ellis, and S. Yang. Helium droplets: A new route to nanoparticles. *Faraday Discuss.*, 162(0):113–124, 2013.

[8] W. Bouwen, F. Vanhoutte, F. Despa, S. Bouckaert, S. Neukermans, L. T. Kuhn, H. Weidele, P. Lievens, and R. E. Silverans. Stability effects of Au_n X_m^+ (X = Cu, Al, Y, In) clusters. *Chem. Phys. Lett.*, 314(3):227–233, 1999.

[9] R. Boyd. *Nonlinear optics*. Academic Press, 3^{rd} edition, 2008.

[10] H. Buchenau, E. L. Knuth, J. Northby, J. P. Toennies, and C. Winkler. Mass spectra and time-of-flight distributions of helium cluster beams. *J. Chem. Phys.*, 92(11):6875–6889, 1990.

[11] O. Bünermann. *Spektroskopie von Alkali- und Erdalkaliatomen, -molekülen, Alkaliclustern und Komplexen organischer Moleküle auf Heliumnanotröpfchen*. PhD thesis, Fakultät für Physik, Universität Bielefeld, 2006.

[12] O. Bünermann, G. Droppelmann, A. Hernando, R. Mayol, and F. Stienkemeier. Unraveling the absorption spectra of alkali metal atoms attached to helium nanodroplets. *J. Phys. Chem. A*, 111(49):12684–12694, 2007.

[13] C. Callegari and W. E. Ernst. Helium droplets as nanocryostats for molecular spectroscopy - from the vacuum ultraviolet to the microwave regime. In *Handbook of High-resolution Spectroscopy*. Eds. M. Quack and F. Merkt, John Wiley & Sons, Ltd, 2011. DOI: 10.1002/9780470749593.hrs064.

[14] F. Cargnoni, T. Kus, M. Mella, and R. J. Bartlett. Ground state potential energy surfaces and bound states of M-He dimers (M = Cu, Ag, Au): A theoretical investigation. *J. Chem. Phys.*, 129(20):204307, 2008.

[15] F. Cargnoni, A. Ponti, and M. Mella. Coinage metal exciplexes with helium atoms: A theoretical study of $M^*(^2L)He_n$(M = Cu, Ag, Au; L = P,D). *Phys. Chem. Chem. Phys.*, 15(42):18410–18423, 2013.

[16] F. Coppens, F. Ancilotto, M. Barranco, N. Halberstadt, and M. Pi. Capture of Xe and Ar atoms by quantized vortices in ^{4}He nanodroplets. *Phys. Chem. Chem. Phys.*, 2017.

[17] F. Dalfovo, A. Lastri, L. Pricaupenko, S. Stringari, and J. Treiner. Structural and dynamical properties of superfluid helium: A density-functional approach. *Phys. Rev. B*, 52(2):1193–1209, 1995.

[18] W. A. de Heer. The physics of simple metal clusters: experimental aspects and simple models. *Rev. Mod. Phys.*, 65(3):611–676, 1993.

[19] M. Fárník, U. Henne, B. Samelin, and J. P. Toennies. Differences in the detachment of electron bubbles from superfluid ^{4}He droplets versus nonsuperfluid ^{3}He droplets. *Phys. Rev. Lett.*, 81:3892–3895, 1998.

[20] M. Fárník, B. Samelin, and J. P. Toennies. Measurements of the lifetimes of electron bubbles in large size selected $^4He_n^-$ droplets. *J. Chem. Phys.*, 110(18):9195–9201, 1999.

[21] F. Federmann, A. Bartelt, J. Close, K. Hoffmann, N. Quaas, and J. Toennies. The UV-absorption of europium atoms embedded in helium nanodroplets. *Z. Phys. D At. Mol. Cl.*, 39(1):1–2, 1997.

[22] F. Federmann, K. Hoffmann, N. Quaas, and J. P. Toennies. Spectroscopy of extremely cold silver clusters in helium droplets. *Eur. Phys. J. D*, 9(1):11–14, 1999.

[23] S. Fedrigo, W. Harbich, and J. Buttet. Optical response of Ag_2, Ag_3, Au_2, and Au_3 in argon matrices. *J. Chem. Phys.*, 99(8):5712–5717, 1993.

[24] D. Figgen, G. Rauhut, M. Dolg, and H. Stoll. Energy-consistent pseudopotentials for group 11 and 12 atoms: adjustment to multi-configuration dirac-hartree-fock data. *Chem. Phys.*, 311(1-2):227–244, 2005.

[25] A. Fujisaki, K. Sano, T. Kinoshita, Y. Takahashi, and T. Yabuzaki. Implantation of neutral atoms into liquid helium by laser sputtering. *Phys. Rev. Lett.*, 71(7):1039–1042, 1993.

[26] A. Golov and S. Sekatskii. A new type of excimer atom: electron + ionized helium cluster. *Z. Phys. D At. Mol. Cl.*, 27(4):349–355, 1993.

[27] L. F. Gomez, K. R. Ferguson, J. P. Cryan, C. Bacellar, R. M. P. Tanyag, C. Jones, S. Schorb, D. Anielski, A. Belkacem, C. Bernando, R. Boll, J. Bozek, S. Carron, G. Chen, T. Delmas, L. Englert, S. W. Epp, B. Erk, L. Foucar, R. Hartmann, A. Hexemer, M. Huth, J. Kwok, S. R. Leone, J. H. S. Ma, F. R. N. C. Maia, E. Malmerberg, S. Marchesini, D. M. Neumark, B. Poon, J. Prell, D. Rolles, B. Rudek, A. Rudenko, M. Seifrid, K. R. Siefermann, F. P. Sturm, M. Swiggers, J. Ullrich, F. Weise, P. Zwart, C. Bostedt, O. Gessner, and A. F. Vilesov. Shapes and vorticities of superfluid helium nanodroplets. *Science*, 345(6199):906–909, 2014.

[28] L. F. Gomez, E. Loginov, and A. F. Vilesov. Traces of vortices in superfluid helium droplets. *Phys. Rev. Lett.*, 108(15):155302, 2012.

[29] S. Goyal, D. Schutt, and G. Scoles. Infrared-spectroscopy in highly quantum matrices - vibrational-spectrum of $(SF_6)_{n=1,2}$ attached to helium clusters (errata of vol 97, p 2236, 1993). *J. Phys. Chem.*, 99(17):6755, 1995.

[30] S. Goyal, D. L. Schutt, and G. Scoles. Vibrational spectroscopy of sulfur hexafluoride attached to helium clusters. *Phys. Rev. Lett.*, 69(6):933–936, 1992.

[31] D. M. Gruen, S. L. Gaudioso, R. L. McBeth, and J. L. Lerner. Application of matrix isolation spectroscopy to quantitative sputtering studies. I. Energies and oscillator strengths of the resonance transitions of gold atoms isolated in noble gas matrices. *J. Chem. Phys.*, 60(1):89–99, 1974.

[32] G. Haberfehlner, P. Thaler, D. Knez, A. Volk, F. Hofer, W. E. Ernst, and G. Kothleitner. Formation of bimetallic clusters in superfluid helium nanodroplets analysed by atomic resolution electron tomography. *Nature Comm.*, 6:8779, 2015.

[33] W. Harbich, S. Fedrigo, J. Buttet, and D. M. Lindsay. Deposition of mass selected gold clusters in solid krypton. *J. Chem. Phys.*, 96(11):8104–8108, 1992.

[34] J. Harms, J. P. Toennies, and F. Dalfovo. Density of superfluid helium droplets. *Phys.Rev. B*, 58(6):3341–3350, 1998.

[35] A. W. Hauser, A. Volk, P. Thaler, and W. E. Ernst. Atomic collisions in suprafluid helium-nanodroplets: timescales for metal-cluster formation derived from He-density functional theory. *Phys. Chem. Chem. Phys.*, 17(16):10805–10812, 2015.

[36] U. Henne and J. P. Toennies. Electron capture by large helium droplets. *J. Chem. Phys.*, 108(22):9327–9338, 1998.

[37] A. Hernando, M. Barranco, R. Mayol, M. Pi, and F. Ancilotto. Density functional theory of the structure of magnesium-doped helium nanodroplets. *Phys. Rev. B*, 78(18):184515, 2008.

[38] A. Hernando, M. Barranco, R. Mayol, M. Pi, and M. Krośnicki. Absorption spectrum of Ca atoms attached to ^{4}He nanodroplets. *Phys.Rev. B*, 77(2):024513, 2008.

[39] J. Higgins, C. Callegari, J. Reho, F. Stienkemeier, W. E. Ernst, K. K. Lehmann, M. Gutowski, and G. Scoles. Photoinduced chemical dynamics of high-spin alkali trimers. *Science*, 273(5275):629–631, 1996.

[40] J. Higgins, W. Ernst, C. Callegari, J. Reho, K. Lehmann, G. Scoles, and M. Gutowski. Spin polarized alkali clusters: Observation of quartet states of the sodium trimer. *Phys. Rev. Lett.*, 77(22):4532, 1996.

[41] W. S. Hopkins, S. M. Hamilton, P. D. McNaughter, and S. R. Mackenzie. VUV photodissociation dynamics of diatomic gold, Au_2: A velocity map imaging study at 157 nm. *Chem. Phys. Lett.*, 483(1):10–15, 2009.

[42] T. M. Inc. Matlab, 2017. version 9.2.0.556344 (R2017a).

[43] C. Jackschath, I. Rabin, and W. Schulze. Electronic structures and related properties. Electron impact ionization potentials of gold and silver clusters Me_n, n $\leq$ 22. *Berich. Bunsen. Gesell.*, 96(9):1200–1204, 1992.

[44] P. K. Jain, I. H. El-Sayed, and M. A. El-Sayed. Au nanoparticles target cancer. *Nano Lett.*, 2(1):18–29, 2007.

[45] J. Jeffs, N. A. Besley, A. J. Stace, G. Sarma, E. M. Cunningham, A. Boatwright, S. Yang, and A. M. Ellis. Metastable aluminum atoms floating on the surface of helium nanodroplets. *Phys. Rev. Lett.*, 114:233401, 2015.

[46] I. Katakuse, T. Ichihara, Y. Fujita, T. Matsuo, T. Sakurai, and H. Matsuda. Mass distributions of copper, silver and gold clusters and electronic shell structure. *Int. J. Mass Spectrom.*, 67(2):229–236, 1985.

[47] A. Kautsch, M. Hasewend, M. Koch, and W. E. Ernst. Fano resonances in chromium photoionization spectra after photoinduced ejection from a superfluid helium nanodroplet. *Phys. Rev. A*, 86(3):033428, 2012.

[48] A. Kautsch, M. Koch, and W. E. Ernst. Photoinduced molecular dissociation and photoinduced recombination mediated by superfluid helium nanodroplets. *Phys. Chem. Chem. Phys.*, 17(18):12310–12316, 2015.

[49] T. Kinoshita, K. Fukuda, and T. Yabuzaki. Doubly shaped D_2 excitation spectra of Cs and Rb atoms in superfluid helium due to a quadrupole bubble surface oscillation. *Phys. Rev. B*, 54(9):6600–6607, 1996.

[50] K. Kneipp. Surface-enhanced raman scattering. *Phys. Today*, 2007.

[51] E. L. Knuth and U. Henne. Average size and size distribution of large droplets produced in a free-jet expansion of a liquid. *J. Chem. Phys.*, 110(5):2664–2668, 1999.

[52] M. Koch. *Magnetic Resonance Spectroscopy of Single Alkali-Metal Atoms Isolated in Superfluid Helium Nanodroplets.* Phd thesis, Graz University of Technology, 2009.

[53] M. Koch, A. Kautsch, F. Lackner, and W. E. Ernst. One- and two-color resonant photoionization spectroscopy of chromium-doped helium nanodroplets. *J. Phys. Chem. A*, 118(37):8373–8379, 2014.

[54] A. Kramida, Y. Ralchenko, J. Reader, and N. A. Team. Nist atomic spectra database (version 5.4). *National Institute of Standards and Technology, Gaithersburg, MD*, 2016. Available: http://physics.nist.gov/asd [May 17 2017].

[55] S. A. Krasnokutski and F. Huisken. Low-temperature chemistry in helium droplets: Reactions of aluminum atoms with O_2 and H_2O. *J. Phys. Chem. A*, 115(25):7120–7126, 2011.

[56] G. Krois. Heavy alkali and alkaline earth metals on cold helium droplets: First comparison of excitation spectra. Master's thesis, Graz Univerity of Technology, 2011.

[57] F. Lackner. Laserspektroskopie und Flugzeitmassenspektrometrie an Rubidium-dotierten Heliumnanotröpfchen. Master's thesis, Graz University of Technology, 2009.

[58] F. Lackner, G. Krois, T. Buchsteiner, J. V. Pototschnig, and W. E. Ernst. Helium-droplet-assisted preparation of cold RbSr molecules. *Phys. Rev. Lett.*, 113:153001, 2014.

[59] F. Lackner, G. Krois, M. Theisen, M. Koch, and W. E. Ernst. Spectroscopy of nS, nP, and nD Rydberg series of Cs atoms on helium nanodroplets. *Phys. Chem. Chem. Phys.*, 13(42):18781–18788, 2011.

[60] J. Ladislas Wiza. Microchannel plate detectors. *Nuclear Instruments and Methods*, 162(1):587–601, 1979.

[61] Lambda Physics. *FL3001/2 Dye Laser Manual*. Lambda Physics GmbH, Hans-Böckler-Str. 12 37079 Göttingen Germany, 1988.

[62] E. Latimer, D. Spence, C. Feng, A. Boatwright, A. M. Ellis, and S. Yang. Preparation of ultrathin nanowires using superfluid helium droplets. *Nano Lett.*, 14(5):2902–2906, 2014.

[63] J. W. Leachman, R. T. Jacobsen, E. W. Lemmon, and S. G. Penoncello. *Thermodynamic Properties of Cryogenic Fluids*. Springer, 2017. Google-Books-ID: Vx8vDwAAQBAJ.

[64] S. Lecoultre, A. Rydlo, C. Félix, J. Buttet, S. Gilb, and W. Harbich. UV - visible absorption of small gold clusters in neon: Au_n (n = 1 - 5 and 7 - 9). *J. Chem. Phys.*, 134(7):074302, 2011.

[65] K. K. Lehmann and J. A. Northby. Potential of an ionic impurity in a large ^{4}He cluster. *Mol. Phys.*, 97(5):639–644, 1999.

[66] M. Lewerenz, B. Schilling, and J. P. Toennies. A new scattering deflection method for determining and selecting the sizes of large liquid clusters of ^{4}He. *Chem. Phys. Lett.*, 206(1):381–387, 1993.

[67] F. Lindebner, A. Kautsch, M. Koch, and W. E. Ernst. Laser ionization and spectroscopy of Cu in superfluid helium nanodroplets. *Int. J. Mass Spectrom.*, 365–366:255–259, 2014.

[68] E. Loginov and M. Drabbels. Excited state dynamics of Ag atoms in helium nanodroplets. *J. Phys. Chem. A*, 111(31):7504–7515, 2007.

[69] E. Loginov and M. Drabbels. Unusual Rydberg system consisting of a positively charged helium nanodroplet with an orbiting electron. *Phys. Rev. Lett.*, 106(8):083401, 2011.

[70] E. Loginov, L. F. Gomez, N. Chiang, A. Halder, N. Guggemos, V. V. Kresin, and A. F. Vilesov. Photoabsorption of Ag_n (n $\sim$ 6 - 6000) nanoclusters formed in helium droplets: Transition from compact to multicenter aggregation. *Phys. Rev. Lett.*, 106(23):233401, 2011.

[71] E. Loginov, L. F. Gomez, and A. F. Vilesov. Surface deposition and imaging of large Ag clusters formed in He droplets. *J. Phys. Chem. A*, 115(25):7199–7204, 2011.

[72] E. Loginov, D. Rossi, and M. Drabbels. Photoelectron spectroscopy of doped helium nanodroplets. *Phys. Rev. Lett.*, 95:163401, 2005.

[73] R. Markus and N. Schwentner. *Photoinduced Aggregation and Dissociation of Ag and Au Clusters in Rare Gas Matrices*. Springer, Boston, MA, 1987. DOI: 10.1007/978-1-4757-0357-3_85.

[74] D. Mateo, A. Hernando, M. Barranco, E. Loginov, M. Drabbels, and M. Pi. Translational dynamics of photoexcited atoms in ^{4}He nanodroplets: The case of silver. *Phys. Chem. Chem. Phys.*, 15(42):18388–18400, 2013.

[75] F. Merkt. Molecules in high Rydberg states. *Ann. Rev. Phys. Chem.*, 48(1):675–709, 1997.

[76] R. Messner, A. Schiffmann, J. V. Pototschnig, M. Lasserus, M. Schnedlitz, F. Lackner, and W. E. Ernst. Spectroscopy of gold atoms and gold oligomers in helium nanodroplets. *In preparation*, 2018.

[77] P. Moroshkin, A. Hofer, and A. Weis. Atomic and molecular defects in solid ^{4}He. *Phys. Rep.*, 469(1):1–57, 2008.

[78] P. Moroshkin, V. Lebedev, and A. Weis. Laser ablation and spectroscopy of copper in liquid and solid ^{4}He. *Phys. Rev. A*, 84(5):052519, 2011.

[79] P. Moroshkin, V. Lebedev, and A. Weis. Vibronic transitions of atomic bubbles in condensed ^{4}He. *Jo. Low Temp. Phys.*, 162(5):710–717, 2011.

[80] P. Moroshkin, V. Lebedev, and A. Weis. Spectroscopy of gold atoms isolated in liquid and solid ^{4}He matrices. *J. Chem. Phys.*, 139(10):104307, 2013.

[81] M. D. Morse. Clusters of transition-metal atoms. *Chem. Rev.*, 86(6):1049–1109, 1986.

[82] V. Mozhayskiy, M. N. Slipchenko, V. K. Adamchuk, and A. F. Vilesov. Use of helium nanodroplets for assembly, transport, and surface deposition of large molecular and atomic clusters. *J. Chem. Phys.*, 127(9):094701, 2007.

[83] J. Nagl, G. Auböck, A. W. Hauser, O. Allard, C. Callegari, and W. E. Ernst. Heteronuclear and homonuclear high-spin alkali trimers on helium nanodroplets. *Phys. Rev. Lett.*, 100(6):063001, 2008.

[84] H. Pauly. *Atom, Molecule, and Cluster Beams II: Cluster Beams, Fast and Slow Beams, Accessory Equipment and Applications*. Springer Science & Business Media, 4 2013. Google-Books-ID: qrHxCAAAQBAJ.

[85] D. S. Peterka, J. H. Kim, C. C. Wang, L. Poisson, and D. M. Neumark. Photoionization dynamics in pure helium droplets. *J. Phys. Chem. A*, 111(31):7449–7459, 2007.

[86] K. A. Peterson and C. Puzzarini. Systematically convergent basis sets for transition metals. II. Pseudopotential-based correlation consistent basis sets for the group 11 (Cu, Ag, Au) and 12 (Zn, Cd, Hg) elements. *Theor. Chem. Acc.*, 114(4-5):283–296, 2005.

[87] J. R. Platt and R. A. Sawyer. New classifications in the spectra of Au I and Au II. *Phys. Rev.*, 60(12):866–876, 1941.

[88] J. V. Pototschnig, F. Lackner, A. W. Hauser, and W. E. Ernst. Rydberg states of alkali atoms on superfluid helium nanodroplets: Inside or outside? *Phys. Chem. Chem. Phys.*, 19(22):14718–14728, 2017.

[89] A. Przystawik, S. Göde, T. Döppner, J. Tiggesbäumker, and K.-H. Meiwes-Broer. Light-induced collapse of metastable magnesium complexes formed in helium nanodroplets. *Phys. Rev. A*, 78:021202, 2008.

[90] A. Przystawik, P. Radcliffe, S. Göde, K. Meiwes-Broer, and J. Tiggesbäumker. Spectroscopy of silver dimers in triplet states. *J. Phys. B: At. Mol. Opt.*, 39(19):S1183, 2006.

[91] M. Ratschek, J. V. Pototschnig, A. W. Hauser, and W. E. Ernst. Solvation and spectral line shifts of chromium atoms in helium droplets based on a density functional theory approach. *J. Phys. Chem. A*, 118(33):6622–6631, 2014.

[92] M. Schnedlitz. A study of thermally induced surface diffusion processes of monometallic nanowires. Master's thesis, Graz University of Technology, 2017.

[93] M. Schnedlitz, M. Lasserus, D. Knez, A. W. Hauser, F. Hofer, and W. E. Ernst. Thermally induced breakup of metallic nanowires: Experiment and theory. *Phys. Chem. Chem. Phys.*, 19(14):9402–9408, 2017.

[94] J. A. Scholl, A. L. Koh, and J. A. Dionne. Quantum plasmon resonances of individual metallic nanoparticles. *Nature*, 483(7390):421–427, 2012.

[95] F. Stienkemeier and K. K. Lehmann. Spectroscopy and dynamics in helium nanodroplets. *J. Phys. B: At. Mol. Opt. Phys.*, 39(8):R127, 2006.

[96] B. Tabbert, M. Beau, H. Günther, W. Häußler, C. Hönninger, K. Meyer, B. Plagemann, and G. Z. Putlitz. Atoms and ions in superfluid helium. *Z. Phys. B Con. Mat.*, 97(3):425–432, 1995.

[97] Y. Takahashi, K. Sano, T. Kinoshita, and T. Yabuzaki. Spectroscopy of alkali atoms and molecules in superfluid helium. *Phys. Rev. Lett.*, 71(7):1035–1038, 1993.

[98] P. Thaler, A. Volk, D. Knez, F. Lackner, G. Haberfehlner, J. Steurer, M. Schnedlitz, and W. E. Ernst. Synthesis of nanoparticles in helium droplets - A characterization comparing mass-spectra and electron microscopy data. *J. Chem. Phys.*, 143(13):134201, 2015.

[99] P. Thaler, A. Volk, F. Lackner, J. Steurer, D. Knez, W. Grogger, F. Hofer, and W. E. Ernst. Formation of bimetallic core-shell nanowires along vortices in superfluid he nanodroplets. *Phys. Rev. B*, 90(15):155442, 2014.

[100] M. Theisen, F. Lackner, and W. E. Ernst. Forming Rb^+ snowballs in the center of He nanodroplets. *Phys. Chem. Chem. Phys.*, 12(45):14861–14863, 2010.

[101] M. Theisen, F. Lackner, and W. E. Ernst. Rb and Cs oligomers in different spin configurations on helium nanodroplets. *J. Phys. Chem. A*, 115(25):7005–7009, 2011.

[102] J. P. Toennies and a. A. F. Vilesov. Spectroscopy of atoms and molecules in liquid helium. *Annual Review of Physical Chemistry*, 49(1):1–41, 1998.

[103] J. P. Toennies and A. F. Vilesov. Superfluid helium droplets: A uniquely cold nanomatrix for molecules and molecular complexes. *Angew. Chem. Int. Ed.*, 43(20):2622–2648, 2004.

[104] P. Toennies, A. F. Vilesov, and K. Birgitta Whaley. Superfluid helium droplets: An ultracold nanolaboratory. *Phys. Today*, 54, 2001.

[105] L. Vegard. The light emitted from solidified gases and its relation to cosmic phenomena. *Nature*, 114:357–359, 1924.

[106] A. Volk, P. Thaler, D. Knez, A. W. Hauser, J. Steurer, W. Grogger, F. Hofer, and W. E. Ernst. The impact of doping rates on the morphologies of silver and gold nanowires grown in helium nanodroplets. *Phys. Chem. Chem. Phys.*, 18:1451–1459, 2016.

[107] J. Wang, G. Wang, and J. Zhao. Density-functional study of Au_n (n = 2 - 20) clusters: Lowest-energy structures and electronic properties. *Phys. Rev. B*, 66(3):035418, 2002.

[108] H.-J. Werner, P. J. Knowles, G. Knizia, F. R. Manby, M. Schütz, P. Celani, T. Korona, R. Lindh, A. Mitrushenkov, G. Rauhut, K. R. Shamasundar, T. B. Adler, R. D. Amos, A. Bernhardsson, A. Berning, D. L. Cooper, M. J. O. Deegan, A. J. Dobbyn, F. Eckert, E. Goll, C. Hampel, A. Hesselmann, G. Hetzer, T. Hrenar, G. Jansen, C. Köppl, Y. Liu, A. W. Lloyd, R. A. Mata, A. J. May, S. J. McNicholas, W. Meyer, M. E. Mura, A. Nicklass, D. P. O'Neill, P. Palmieri, D. Peng, K. Pflüger, R. Pitzer, M. Reiher, T. Shiozaki, H. Stoll, A. J. Stone, R. Tarroni, T. Thorsteinsson, and M. Wang. Molpro, version 2012.1, a package of ab initio programs, 2012. see http://www.molpro.net.

[109] E. Whittle, D. A. Dows, and G. C. Pimentel. Matrix isolation method for the experimental study of unstable species. *J. Chem. Phys.*, 22(11):1943–1943, 1954.

[110] E. Wigner. *Gruppentheorie und ihre Anwendung auf die Quantenmechanik der Atomspektren*. Vieweg+Teubner Verlag, 1931. DOI: 10.1007/978-3-663-02555-9.

[111] G. A. Williams and R. E. Packard. Photographs of quantized vortex lines in rotating He II. *Phys. Rev. Lett.*, 33(5):280–283, 1974.

[112] I. Wolfram Research. Mathematica, 2017. Champaign, Illinois Wolfram Research, Inc.

[113] D. E. Woon and T. H. Dunning. Gaussian-basis Sets For Use In Correlated Molecular Calculations .4. Calculation of Static Electrical Response Properties. *J. Chem. Phys.*, 100(4):2975–2988, 1994.

[114] Q. Wu, C. J. Ridge, S. Zhao, D. Zakharov, J. Cen, X. Tong, E. Connors, D. Su, E. A. Stach, C. M. Lindsay, et al. Development of a new generation of stable, tunable, and catalytically active nanoparticles produced by the helium nanodroplet deposition method. *J. Phys Chem. Lett.*, 7(15):2910–2914, 2016.

[115] Z. Xiaohang and M. Drabbels. Communication: Barium ions and helium nanodroplets: Solvation and desolvation. *J. Chem. Phys.*, 137(5), 2012.

[116] E. J. Yarmchuk, M. J. V. Gordon, and R. E. Packard. Observation of stationary vortex arrays in rotating superfluid helium. *Phys. Rev. Lett.*, 43(3):214–217, 1979.

[117] O. Zatsarinny, K. Bartschat, M. Maslov, M. J. Brunger, and P. J. O. Teubner. Electron-impact excitation of the $(5d^{10}6s)\ ^2S_{1/2} \rightarrow (5d^96s^2)\ ^2D_{5/2,3/2}$ transitions in gold atoms. *Phys. Rev. A*, 78(4):042713, 2008.

[118] Y. Zhang, J. R. G. Evans, and S. Yang. Corrected values for boiling points and enthalpies of vaporization of elements in handbooks. *J. Chem. Eng. Data*, 56(2):328–337, 2011.

Danksagung

Zu guter Letzt möchte ich mich bei all jenen bedanken, die mich bei dieser Arbeit unterstützt haben, sei es durch direktes Einwirken oder aber auch guten Einfluss.

Allen voran möchte ich mich bei meinem Betreuer Herrn Prof. Wolfgang E. Ernst dafür bedanken, dass er mir die Möglichkeit gegeben hat, während meiner Diplomarbeit an einem so spannenden und anspruchsvollen Thema, mit durchaus wissenschaftlicher Relevanz, zu arbeiten. Auch für den ersten Einblick in den wissenschaftlichen Forschungsbetrieb bin ich sehr dankbar, sogleich dieser doch in einem so behaglichen Arbeitsumfeld stattgefunden hat.
Auch meinem Ko-Betreuer Florian Lackner möchte ich bei dieser Gelegenheit meinen Dank aussprechen, welcher mich durchgehend tatkräftigt unterstützt hat und essentielle Teile zu meiner Arbeit in der Forschungsgruppe beigetragen hat. Sowohl bei theoretischen als auch experimentellen Belangen, hatte er immer ein offenes Ohr und guten Rat zur Hand.
Johann Pototschnig verdanke ich die aufwändigen und sehr aussagekräftigen Berechnungen, die ich in meiner Diplomarbeit präsentieren durfte. Ohne diese Befunde wäre die Interpretation meiner Ergebnisse erheblich erschwert worden, wenn sie nicht teilweise unmöglich gewesen wären.
Dank gebührt auch meinen Mitarbeitern aus dem Clusterlabor 3, Alexander Schiffmann, Florian Lackner, Martin Schnedlitz, Maximilian I. Lasserus und Philip Zettl, für das sehr familiäre Abeitsklima, viele konstruktive Diskussionen, oftmals helfende Hände bei experimentellen Schwierigkeiten aber auch spaßige Kaffeepausen. Besonders meinen Bürokollegen, Max und Martin, die mich während meiner Anfangszeit in das Labor und den theoretischen Hintergrund eingeführt haben, danke ich für die Geduld, Sorgfalt und Expertise welche sie mir entgegengebracht haben.

Bei den fleißigen Korrekturlesern Martin Schnedlitz und Florian Lackner möchte ich mich bedanken und gleichzeitig entschuldigen für jeden Tippfeler und, Beistrichfehler.

Auch all meinen Freunden und Studienkollegen, ohne die mein Studium nur halb so viel Spaß gemacht hätte, möchte ich an dieser Stelle danken. Besonders Andi, Jakob, Kathi, Kriszi, Lukas, Manu, Martin, Max, Mopsi, Pascal, Philip und Raffi seien hier als Beispiele für besonders hervorragende ZeitgenossInnen hervorgehoben, welche ich in meinem Leben nicht missen möchte.

Am Schluss möchte ich mich noch bei meinen Eltern bedanken, die mich immer unterstützt und mir mein Studium erst ermöglicht haben.